UNIVERSITÀ DEGLI STUDI DI UDINE
hic sunt futura

www.uniud.it

Doctorate course in:

"Energy and Environment Engineering Science"

XXXVII cycle

Thesis title

"New oxygen carriers for efficient syngas and H_2 production by chemical looping steam methane reforming"

PhD candidate

Andrea Strazzolini

Advisor

Prof. Marta Boaro

Co-advisor

Prof. Carla de Leitenburg

Year 2025

The following dissertation wars reviewed by:

Prof. Fausto Gallucci, Eindhoven University of Technology (NL)

Prof. Massimo G. L. Santarelli, Politecnico di Torino (IT)

Defense committee members:

Prof. Antonella Glisenti, Università di Padova (IT)

Prof. Fausto Gallucci, Eindhoven University of Technology (NL)

Prof. Sara Colussi, Università di Udine (IT)

Prof. Victor Hacker, University of Graz (AT)

Abstract

Concerns about the dramatic effects that the anthropogenic-induced climate change could have on human societies on a global scale provide a strong drive to the development of alternative technologies in nearly all fields of science, including industrial chemistry. Given the significant contribution of the energy and chemical sectors to greenhouse gas emissions, the rapid development of novel environmentally friendly energy generation and chemical production processes, as well as the efficiency improvement of existing ones, is of paramount importance to slow down and halt as soon as possible the causes of alterations in the global climate system, which threatens human activities, biodiversity and ultimately life on this planet. In the last two decades, Chemical Looping (CL) technologies has garnered scientific interest as energy-efficient and emission-free hydrocarbons conversion pathways, fostering a continuous effort to improve and upscale processes that has shown promising results from the laboratory to the pilot scale. In such systems, a redox reaction is split into multiple subreactions using a solid Oxygen Carrier (OC) as an intermediate, able to reversibly exchange lattice oxygen with the reaction atmosphere in a cyclic manner. Large part of this effort has been dedicated to the development of active and reliable OC systems, since they are crucial for the chemical, energetic and economic performance of such processes.

Chemical Looping Steam Methane Reforming (CL-SMR) enables the simultaneous production of separate streams of syngas and hydrogen, minimizing the need for upstream and downstream gas separation and product refinement compared to conventional processes. This approach offers the potential for improved efficiency and reduced capital costs. Fe-based materials offer several advantages as OC materials in several different CL applications, but they often exhibit limited reactivity with hydrocarbons, particularly methane, which can hinder the process efficiency.

Focus of this dissertation is the development of multi-functional OC systems for the CL-SMR process. The OC systems investigated include a Fe-containing main oxygen transfer phase and a Ni-based catalytic phase, aimed at improving the reactivity of Fe-based materials towards methane.

In Chapter 1, a general overview of the scientific background and of the state-of-the-art methane to chemicals conversion processes is provided. The main research findings on related chemical looping technologies are discussed, focusing on OC material development.

In Chapter 2, the experimental methods commonly adopted throughout the research work are briefly reported. The custom-built setup specifically developed at the University of Udine for running CL-SMR experiments is hereby described.

In Chapter 3, the behaviour and stability of a Fe-based OC material, $Ca_2Fe_2O_5$ (here referred to as C2F), in periodic reduction-oxidation cycles is investigated. The influence of various parameters, including temperature, pressure, and the molar fraction of reactants in the feed, was analysed within ranges relevant to practical industrial applications. The structural and morphological evolution of the material following deep reduction and complete reoxidation was examined, leading to a better understanding of the material's redox behaviour and the remarkable

stability it has shown. A comprehensive kinetic model of the solid's reduction reaction with H_2 was developed, providing additional insights on the OCs reactivity under pressurized conditions, a topic that has been relatively underexplored in the scientific literature.

In Chapter 4, composite OC materials were prepared by physically mixing C2F with $Ce_{0.8}Zr_{0.2}O_2$ (CZ) and tested for CL-SMR cycles. Different functionalization strategies of the composite OC with Ni were compared in terms of CL-SMR performance and redox stability. The highest reactivity improvement was found when Ni is selectively deposited onto the CZ, thus preventing chemical interactions between Ni and Fe. Further investigation into the loss of reactivity over cycles of the best-performing sample revealed that the morphological stability of CZ is the critical factor influencing the durability of such composite systems.

In Chapter 5, a stable composite OC material was realized by physically mixing C2F with Ni-loaded SiO_2-modified CeO_2. The behaviour of the composite was investigated via *in situ* and *ex situ* techniques to clarify the role of the CeO_2-supported Ni catalyst in the OC system. The findings reveal that the improved reactivity of the composite towards CH_4 is due to a gas-phase mediated cooperative mechanism, able to enhance the oxygen exchange rate without affecting the syngas selectivity during the reduction step.

In Chapter 6, an alternative strategy to produce catalyst-promoted Fe-based OCs for CL-SMR was preliminarily explored, making use of the phenomenon of redox exsolution. Starting with the Fe-containing double perovskite $Sr_2FeMo_{0.6}Ni_{0.4}O_6$ (SFMN), a redox-active material decorated with metallic Ni nanoparticles was obtained by exposition to a reductive atmosphere at high temperature. The structural transformation taking place upon the reductive treatment has been found to significantly promote the OC reactivity with CH_4. The so-realized OC showed no sign of deactivation in 50 CL-SMR cycles, highlighting redox exsolution as a promising method for creating highly active and stable OCs.

In Chapter 7, the findings from the previous chapters are briefly summarized, and potential areas for further research arising from this work are outlined.

In conclusion, different functionalization strategies were developed to improve the reactivity of Fe-based OCs with CH_4 in CL-SMR cycles. The work provides guidance for the rational design of catalyst-promoted OC materials, broadening the design space to create OC systems that meet industrial application criteria, including chemical performance, durability and production cost considerations.

Table of Contents

List of abbreviations

aCLR: Autothermal Chemical Looping Reforming

ATR: Autothermal Reforming

BET: Brunauer-Emmett-Teller

C2F: $Ca_2Fe_2O_5$

CL: Chemical Looping

CL-DRM: Chemical Looping Dry Reforming of Methane

CL-POM: Chemical Looping Partial Oxidation of Methane

CL-RWGS: Chemical Looping Reverse Water Gas Shift

CL-SMR: Chemical Looping Steam Methane Reforming

CLC: Chemical Looping Combustion

CLR: Chemical Looping Reforming

CZ: $Ce_{0.8}Zr_{0.2}O_2$

DFT: Density Functional Theory

DRM: Dry Reforming of Methane

EDS: Energy Dispersive Spectroscopy

FESEM: Field Emission Scanning Electron Microscopy

FBR: Fluidized Bed Reactor

GHG: Greenhouse Gases

GTL: Gas to Liquids

HAADF-STEM: High-Angle Annular Dark Field Scanning Transmission Electron Microscopy

HP-TGA: High-Pressure Thermogravimetric Analysis

HRTEM: High-Resolution Transmission Electron Microscopy

IEA: International Energy Agency

JMAEK: Johnson-Mehl-Avrami-Erofeev-Kolmogorov (kinetic model)

MIP: Mercury Intrusion Porosimetry

OC: Oxygen Carrier

OTC: Oxygen Transfer Capacity

POM: Partial Oxidation of Methane

PSA: Pressure Swing Adsorption

RP: Ruddlesden-Popper

SFM: $SrFe_{1.5}Mo_{0.5}O_6$

SFMN: $SrFe_{1.5}Mo_{0.6}Ni_{0.4}O_6$

SEM: Scanning Electron Microscopy

SMR: Steam Methane Reforming

SR-CLC: Steam Reforming - Chemical Looping Combustion

TEOS: Tetraethyl Orthosilicate

TGA: Thermogravimetric Analysis

TPR: Temperature-Programmed Reduction

WGS: Water Gas Shift

XPD: X-ray Powder Diffraction

XPS: X-ray Photoelectron Spectroscopy

XRD: X-ray Diffraction

1. Background and motivation

1.1. Overview

The climate-altering emissions generated by human activities have been unambiguously identified as responsible for the rise of the global mean surface temperature that took place since the industrial revolution [1]. The increase, quantified in 1.1 °C as of 2022 [2], poses significant threats to environmental security, air quality, biodiversity, water, food, and soil resources [3-5]. Research shows that 3.6 billion people already live in areas highly susceptible to climate change [6], placing significant pressure on the international community to promptly develop effective countermeasures. The use of fossil sources in the energy, industry, and transport sectors, together with land use change, caused an increase in the atmospheric concentration of the so-called Greenhouse Gases (GHGs), such as CO_2, CH_4 and N_2O, which are able to absorb infrared radiation emitted from Earth's surface and reradiating it back to the surface, significantly affecting the Earth system energy budget [7]. In the sole 2019, it was estimated that 59 $GtCO_2$-eq (net value) has been emitted by anthropic activities [2]. Among these, in the European Union as in the rest of the world the energy sector plays a dominant role (figure 1.1a). CO_2 accounts for by far the largest share of GHG emissions in the EU (figure 1.1b). The second-largest contribution comes from CH_4 emissions. In the context of the energy transition, CH_4 represents both an opportunity and a threat. In fact, as the main component of (fossil) natural gas it has long been considered a transitional fuel, bridging the phase-out of coal and oil to the development of large-scale renewable energy grids. This is due to its lower carbon content compared to coal and oil on a per-energy basis, as well as the reduced pollutant emissions (such as SO_2 and particulates) associated with its combustion. Natural gas is considered an abundant fossil resource, with proven reserves of $1.88*10^{14}$ m^3 (ISO 13443 reference conditions) [8], and its demand is likely to overtake other fossil fuels due to its availability, accessibility, versatility, and smaller environmental footprint [9]. Nevertheless, its role as bridging fuel has been deeply questioned by the scientific community [10-12]. While natural gas is indeed less emission-intensive than other fossil fuels like oil and coal, greenhouse gas emissions from its production and transportation are often underestimated due to limited data on fugitive CH_4 emissions in the sector. Additionally, investments in existing natural gas infrastructure may hinder a direct transition to renewable energy sources. Nevertheless, the abundance of natural gas presents an opportunity in the pursuit of decarbonization and has spurred significant interest in utilizing CH_4 as a hydrocarbon feedstock for the chemical industry [13-18].

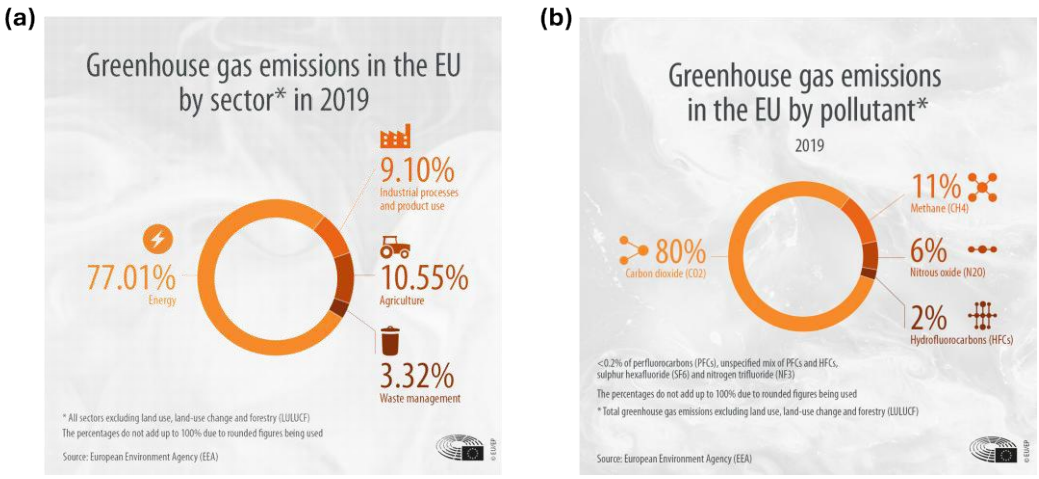

Fig.1.1. Greenhouse gas emissions in the European Union in 2019 (a) by sector and (b) by pollutant. [19].

Low-emission methane-to-chemicals processes could become a cost-effective technology platform for the production of commodity chemicals and intermediates in the foreseeable future. As an example, it is forecasted that in 2060 the average levelized cost of hydrogen produced from natural gas implementing carbon capture and storage technologies will be still lower than that produced by renewables-powered electrolysis (figure 1.2). In addition to that, the production of CH_4 from renewable (biological) sources has grown over the last decade and an even steeper increase is expected, promoting the development of a hybrid fossil-renewable gas infrastructure. In this regard, the International Energy Agency (IEA) estimated a potential yearly biomethane supply higher than $1*10^{12}$ m^3 in 2040 [20], roughly equal to 25% of the total natural gas demand in 2018 [21]. In the short term, alternative CH_4 transformation routes could provide an economically viable solution to convert the natural gas that is currently flared in the proximity of oil production facilities due to the insufficient local infrastructure and/or to high costs of transmission to the market, a practice that have generated 357 $MtCO_2$-eq of emissions in 2022 [22]. In this framework, low-emitting and energy efficient conversion paths of methane to hydrogen and valuable products, such as chemicals and energy carriers, will become of greater importance due to the sustainability value of decarbonizing existing industrial assets.

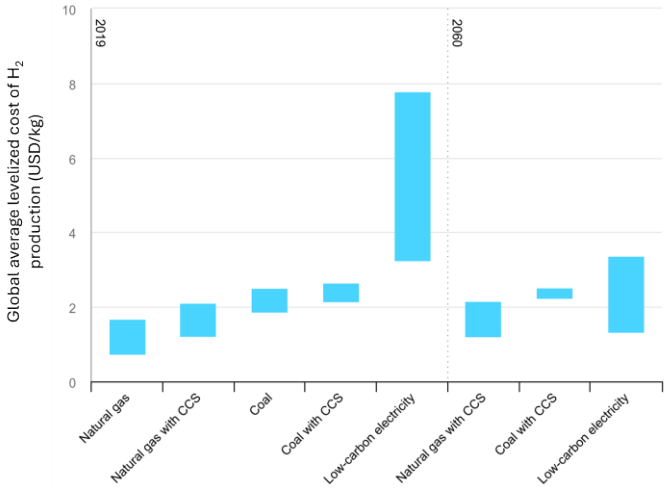

Fig. 1.2. Global average levelized cost of hydrogen production by energy source and technology, 2019 and 2060 [23].

1.2. Syngas and H_2 production from CH_4

Currently, all the methane-to-chemicals processes deployed at commercial scale are of the "indirect" type, meaning that methane is converted into the so-called synthesis gas or syngas, a mixture of gases composed mainly by H_2 and CO, by the addition of reforming agents (H_2O, CO_2, O_2). Syngas is a very flexible intermediate, that can be further processed and employed for the production of a plethora of commodity chemicals such as H_2, NH_3 methanol, higher hydrocarbons (figures 1.3 and 1.4). The main natural gas to syngas conversion processes adopted are Steam Methane Reforming (SMR), Autothermal Reforming (ATR) and Methane Partial Oxidation (POM), which will be discussed later in this section. All the aforementioned processes are remarkably capital intensive (largely due to the heat exchange elements inside and outside the reactor), making syngas production the most expensive step in the CH_4 indirect conversion [18, 24]. This is especially true when syngas is converted to H_2. In the case of ammonia production, the train of process units needed for the generation and purification of hydrogen from natural gas can account for more than 50% of the overall capital costs of the plant [25]. Consequently, syngas production is characterized by a strong reliance on economies of scale, restricting its application to stranded natural gas or geographically distributed biomethane resources.

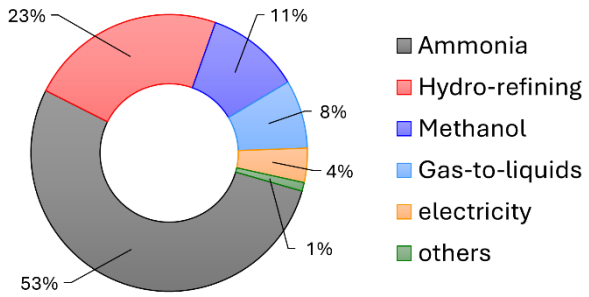

Fig. 1.3. syngas uses in 2004 [26].

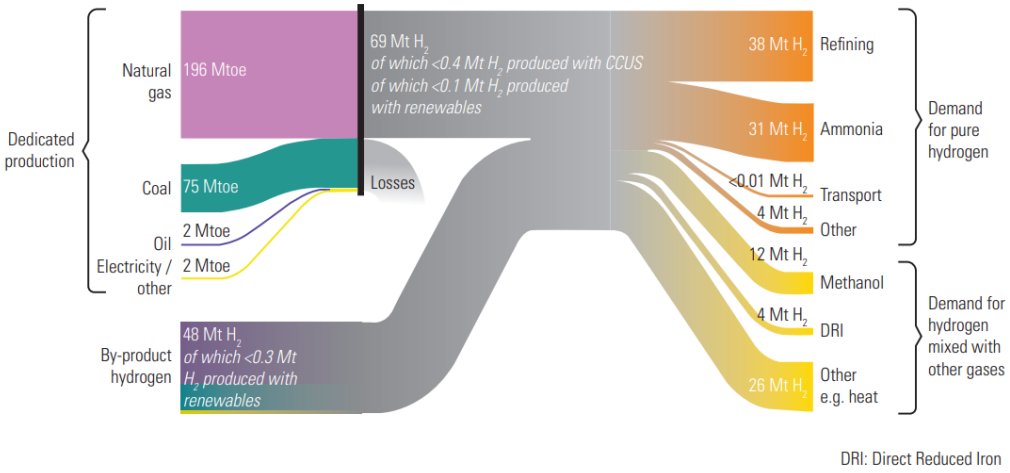

Fig. 1.4. H_2 (and syngas) global value chain in 2015 [27].

1.2.1. Steam methane reforming

In the SMR process, syngas is produced according to the reaction (1.1).

$$\boldsymbol{CH_4 + H_2O \rightleftharpoons CO + 3\,H_2} \qquad \boldsymbol{\Delta H^{\ominus}_{298K} = 206\ kJ/mol} \tag{1.1}$$

Stoichiometrically, the produced syngas has a H_2 to CO ratio of 3. Nevertheless, the actual value is affected by the concurrent water gas shift reaction (equation 1.2). At the operative conditions typically adopted for SMR (temperatures up to 950 °C, pressure between 20 and 30 bar, presence of a catalyst [24]), both reactions approach the equilibrium value. Moreover, to prevent catalyst deactivation by solid carbonaceous species that can be formed from CH_4 pyrolysis (eq. 1.3), the steam to CH_4 ratio in the inlet stream is kept high (typically between 2 and 5) [24], further raising the H_2/CO ratio. The equilibrium composition of a typical feed gas with a steam-to-methane ratio of 2.5 is shown in figure 1.5. To lower the H_2/CO ratio of the product gas, part of the steam can be substituted by CO_2, which generates additional CO via the Dry Methane Reforming (DRM) reaction (eq. 1.4). In the latter case, the process is referred as methane bi-reforming [28].

$$\boldsymbol{CO + H_2O \rightleftharpoons CO + H_2} \qquad \boldsymbol{\Delta H^{\ominus}_{298K} = -41\ kJ/mol} \tag{1.2}$$

$$\boldsymbol{CH_4 \rightleftharpoons C + 2\,H_2} \qquad \Delta H^{\ominus}_{298K} = 75\ kJ/mol \tag{1.3}$$

$$\boldsymbol{CH_4 + CO_2 \rightleftharpoons 2\,CO + 2\,H_2} \qquad \Delta H^{\ominus}_{298K} = 247\ kJ/mol \tag{1.4}$$

The steam reforming reaction involves two very stable molecules (CH_4 and H_2O) and is highly endothermal. For this reason, part of the natural gas input (approximately one third) is combusted to provide the necessary heat. Moreover, the need for an over-stoichiometric steam input increases the total thermal load of the system, lowering the energy efficiency.

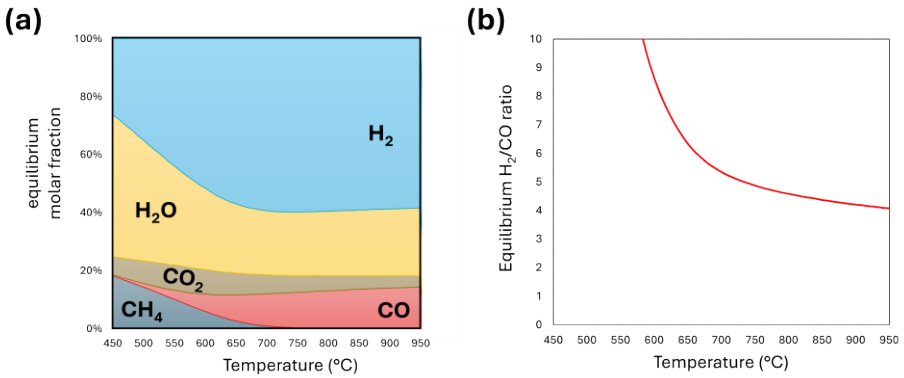

Fig. 1.5. (a) Equilibrium composition and (b) equilibrium H_2/CO ratio of a typical feed (steam to methane ratio of 2.5) as calculated from the HSC chemistry 5 software package.

1.2.2. Methane partial oxidation

The POM process produces syngas from direct partial oxidation (equation 1.4). The process can be carried out both with and without a catalyst. The exothermicity of the reaction eliminate the need for external heating. Nevertheless, the need for a capital and energy-intensive air separation unit to produce pure O_2 feed affects the

economics of the process, again favouring large-scale facilities. Moreover, safety concerns can arise related to the control of the heat balance and the presence in the process streams of CH_4-O_2 mixtures. Typically, the non-catalytic process results in a product gas with a H_2 to CO ratio of 1.7-1.8 [24].

$$\boldsymbol{CH_4 + 1/2\ O_2 \rightleftharpoons CO + 2\ H_2} \qquad \boldsymbol{\Delta H^{\ominus}_{298K} = -36\ kJ/mol} \tag{1.5}$$

1.2.3. Autothermal reforming

Autothermal reforming represents the integration of the two processes presented above. In this case, CH_4 is co-fed with O_2 and H_2O. The heat required for reforming reactions is supplied by the exothermic reactions between CH_4 and O_2. A catalytic bed is included to drive the products distribution close to the thermodynamic equilibrium. Also in this case, the air separation unit affects the economy of the process, resulting in approximately 40% of the total plant cost [29].

1.2.4. H_2 production

Currently, roughly half of the total dedicated H_2 production (70 Mt in 2020) originates from natural gas reforming (figure 1.6). Pure H_2 is used mainly for hydrotreating processes in refineries (52% in 2015), ammonia synthesis (42%), being the rest hydrogenation reactions in the food and fine chemicals industries, semiconductors production and as transportation fuel [27]. Excluding the production via electrochemistry, pure H_2 is obtained from syngas using multiple unit operations, which generally involve one or two (high and low temperature) Water Gas Shift (WGS, equation 1.2) reactors and a Pressure Swing Absorption (PSA) unit to reach the desired purity (figure 1.7).

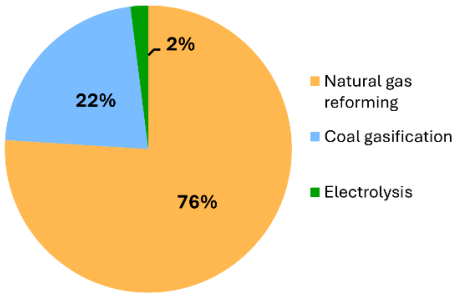

Fig. 1.6. Global dedicated H_2 production by source in 2020 [27].

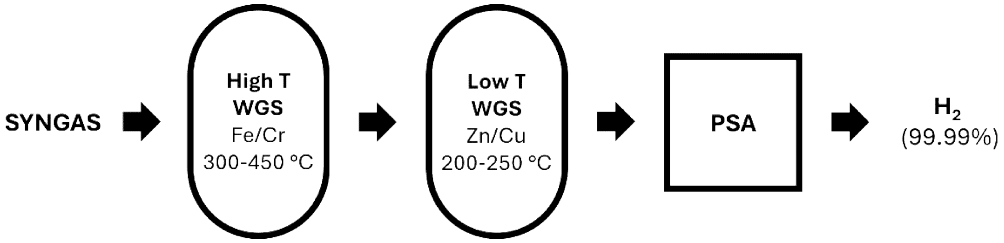

Fig. 1.7. Typical unit operations involved in the production of pure H_2 from syngas [30, 31].

1.3. The chemical looping technology

Chemical looping is a reaction scheme that make use of a redox mediator to decompose a given reaction into multiple sub-reactions, in which the redox mediator acts as a chemical intermediate being reacted and regenerated within the sub-reactions. Ideally, the sub-reactions are configured to minimize the exergy losses of the process. [32]. This principle can provide several advantages in respect of conventional process schemes, such as an intrinsic separation of products streams coming from the sub-reactions, thus reducing the energetic and capital cost of products separation and/or purification and allowing to overcome equilibrium limitations [33]. Historically, the term "chemical looping" was first introduced by Ishida et al. [34] to describe a process scheme for the combustion of carbonaceous fuels. They proposed the use of a reducible metal oxide to oxidize the fuel to H_2O and CO_2 using its lattice oxygen. The oxygen-depleted solid was then regenerated in air, generating thermal energy to drive a gas turbine, thanks to the large exothermicity of the oxidation reaction. The concept was originally introduced to improve the exergy efficiency of the combustion process, by leveraging the fact that the oxidation of the solid takes place at temperatures lower than those of direct combustion of the fuel with molecular oxygen. Revised with a modern twist, this approach allows for the production of a concentrated stream of CO_2 (and steam, which can be easily separated by condensation), ready for compression and storage. In respect of the oxy-combustion process, the need for a cost and energy-intensive cryogenic Air Separation Unit (ASU) is removed, since the oxygen separation is performed by the metal oxide itself [35]. For this reason, a rise in the scientific interest towards Chemical Looping Combustion (CLC) took place in the early 2000s (figure 1.8). Aside from energy generation with integrated carbon capture, the chemical looping approach can be leveraged to raise the efficiency of several chemical processes such as biomass and coal gasification [36], hydrocarbons reforming [37] oxidative dehydrogenations [38], and even ammonia synthesis [39].

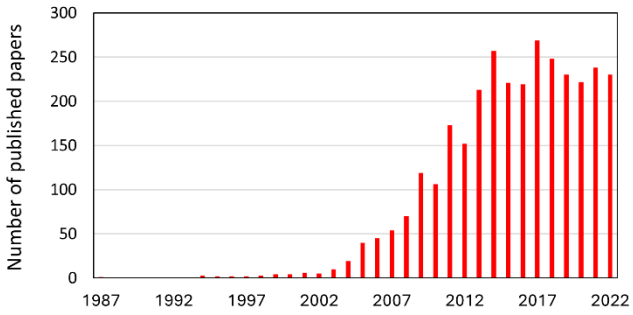

Fig. 1.8. Literature search results using the keywords "Chemical Looping Combustion" on Scopus published between 1987 and 2022 (searched 22/10/2024).

1.3.1. Hydrocarbons reforming with chemical looping

The use of a metal oxide, also termed oxygen carrier (OC), to transport oxygen from two or more different reaction environments give rise to some potential benefits for what concerns the conversion of carbonaceous fuels to syngas. First of all, by selecting OC materials with appropriate thermodynamic properties, the feed can be selectively oxidized to H_2 and CO by the solid's lattice oxygen. A useful tool to perform such screening is represented by Ellingham diagrams (figure 1.9), in which the Gibbs free energy of reactions is plotted against

temperature. Redox couples suitable for partial oxidation applications have a Gibbs free energy of reaction (oxidation) higher than that of the partial oxidation of methane and solid carbon with molecular oxygen and lower than that of hydrogen oxidation to water (blue area in figure 1.9). This means that redox couples that fall in this area of the diagram are thermodynamically able to perform partial oxidation and gasification reactions using their lattice oxygen, while further oxidation of H_2 and CO to total combustion products is unfavoured. Furthermore, the thermodynamic properties of the chosen OC determine which oxidizing agent(s) can be used to regenerate the carrier material. Regarding syngas production, the oxidants considered include air, enabling a mildly exothermic cycle equivalent to the partial oxidation reaction (Eq. 1.5); steam, enabling the overall endothermic SMR reaction (Eq. 1.1); or CO_2, enabling the endothermic DRM reaction (Eq. 1.4). While the Chemical Looping Partial Oxidation of Methane (CL-POM) offers the possibility to produce syngas with a H_2/CO ratio of about two while exporting process heat, Chemical Looping Steam and Dry Methane Reforming (CL-SMR and CL-DMR respectively) offer the interesting advantage of producing together with syngas a separate H_2 or CO-containing product stream at the expense of requiring a significant net heat input. This is particularly relevant in the case of CL-SMR, where pure hydrogen can be obtained by simple condensation of the unconverted steam fed to the oxidizer reactor.

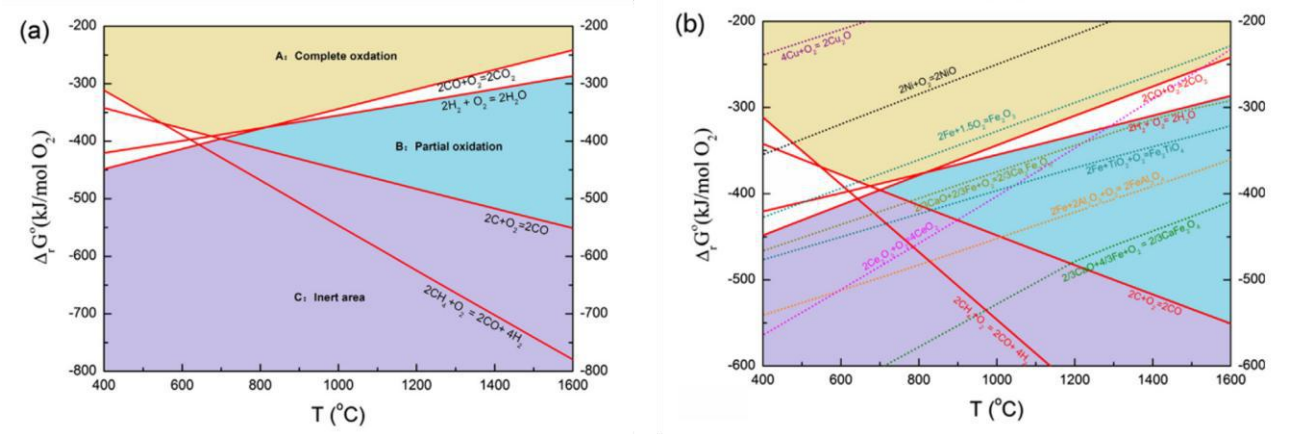

Fig. 1.9. Ellingham diagram showing the variation of oxidation Gibbs free energy with temperature for oxygen carriers: (a) reaction zone division for chemical looping complete oxidation, partial oxidation and inert area and (b) standard Gibbs free energy changes of related oxidation reactions of some oxygen carrier materials [40].

Given these premises, several different process technologies were developed to implement chemical looping methane reforming (figure 1.10) [42]. Among these, the closest to conventional SMR is represented by the integration of CLC to conventional steam reforming (SR-CLC, figure 1.10a). In this case, CLC is used as a way to generate the heat needed for driving the steam reformer, which is directly placed inside the oxidiser reactor. While relying on conventional reforming technology and unit operations, this approach allows for the facile separation of CO_2 from the CLC's reducer reactor. Since the combustion and the reforming processes are decoupled, this configuration offers the highest flexibility on the type of fuel used. Alternatively, the two processes can be combined to maximise the syngas production while operating in in an autothermal regime. The process, named Autothermal Chemical Looping Reforming (aCLR, figure 1.10b), make use of a NiO-based oxygen carrier which acts both as an oxygen vector and as a reforming catalyst. In the reducer reactor, CH_4 is co-fed together with H_2O.

The carbon in the feed is converted to CO partially by the lattice oxygen of NiO and partially by the Ni-catalysed reaction with steam. The steam also inhibits the carbon deposition by CH_4 pyrolysis on the catalytically active sites. The heat needed to drive the endothermal reactions is provided by the oxidation of Ni to NiO, taking place in the oxidiser reactor, and transported by the OC itself. The air-to-fuel ratio is nevertheless kept low to prevent the full oxidation of the fuel. In a similar way, CL-POM (figure 1.10c) can make use of oxygen carriers different than NiO, such as Fe-based perovskites [43]. A careful selection of the OC material, together with a restricted air-to-fuel ratio, drives the selectivity towards syngas without co-feeding steam. The overall process is slightly exothermic, allowing for a net heat export. Alternatively, the OC reoxidation can be fully or partly carried on with steam, thus realizing two or three reactors CL-SMR (figure 1.10d, e). The air oxidation step in the three reactors configuration can be implemented to allow the complete regeneration of the carrier and/or to provide part of the thermal energy required to sustain the heat requirement of the reducer reactor. CL-SMR can achieve higher fuel conversion, syngas yield and thermal and exergy efficiency compared to conventional ATR, thus rendering the process economically attractive [44].

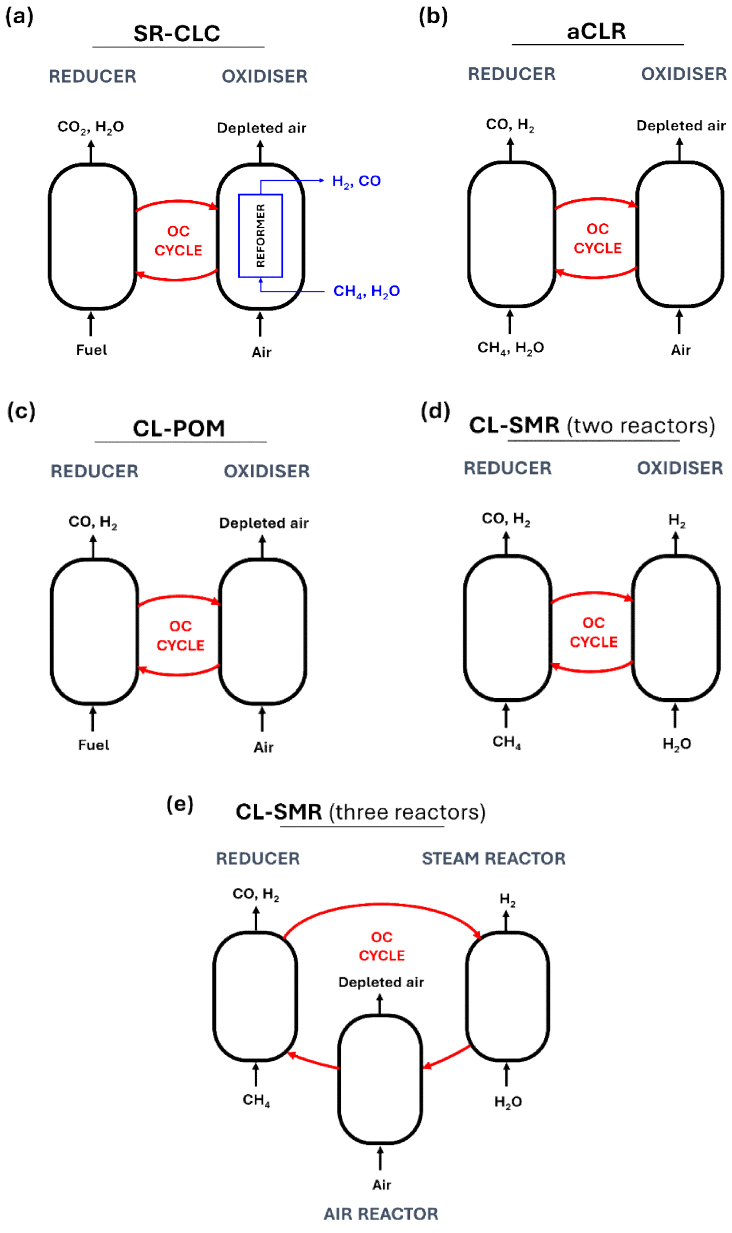

Fig.1.10. Basic schemes of chemical looping reforming.

1.3.2. Reactor technology

Multiple reactor types can be implemented in CLR processes. The first laboratory-scale CLR reactors were developed from CLC systems, thus they were constituted by two interconnected fluidized bed implementing the CL-POM or aCLR reaction scheme with supported NiO as OC material [45]. By the control of the air-to-fuel ratio, the product selectivity was effectively shifted from steam and CO_2 to syngas. However, the use of fluidized bed imposed some restraints to the syngas purity because the solid conversion had to be kept below 0.4 to avoid carbon deposition, leading to overoxidation [32]. To improve the selectivity and to allow for the use of OCs like iron and copper oxides, that can thermodynamically oxidize the fuel to CO_2 and H_2O and therefore could further reduce the syngas selectivity, the use of cocurrent moving beds reducers was proposed [46]. In this type of reactor, oxidized OC particles are fed on the top of the reducer and travel downward along with the gas stream, exiting at the bottom. This configuration establishes a gradient in the oxidation state of the OC particles throughout the reactor's length, with the most reduced particles located near the outlet. Doing so, the thermodynamic drive towards total oxidation products in the last section of the reactor is minimized, improving the selectivity towards syngas. A typical CL-POM system configuration, with a co-current moving bed reducer and a fast fluidized bed air riser, is depicted in figure 1.13. In the case of CL-SMR, the reaction with steam can be carried out in a moving bed operating in countercurrent. In this configuration, the reduced OC particles coming from the reducer are fed near the gas outlet, maximizing the steam conversion to H_2. Alternatively, CLR processes could be operated in fixed bed reactors by cyclically switching between reducing and oxidizing feeds [32, 47]. A schematic depiction of the process is reported in figure 1.14. In this configuration, the semireactions are not conducted in separate reactors, but they take place at different times. This configuration allows for the easy implementation of pressurized CLR processes and poses less mechanical stress on the OC particles. On the other side, it requires operating gas-switching valves at high temperature and some precautions to avoid gas mixing between the reduction and the oxidation step.

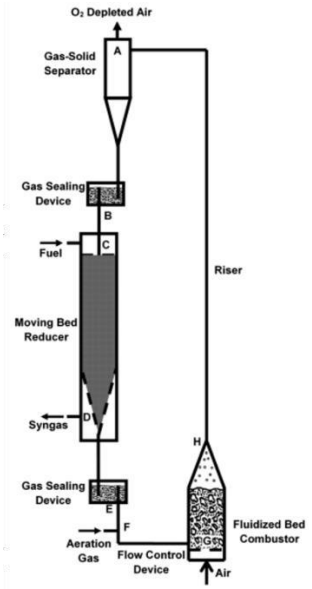

Fig. 1.13. Typical CL-POM system configuration, with a cocurrent moving bed reducer and a fast fluidized bed oxidizer [32].

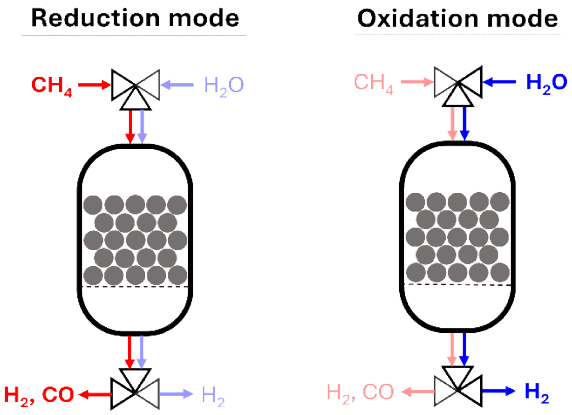

Fig. 1.14. CL-SMR reactor configuration with dynamically operated fixed bed reactors.

1.3.3. Oxygen carriers

Oxygen carriers are at the heart of every chemical looping scheme. Their physical, thermodynamic, and kinetic properties largely determine the product quality, the process efficiency and ultimately the economics of the process [48]. Given the harsh conditions to which OCs are exposed, such as high temperatures, high oxygen potential gradients and extreme redox potential variations of the reaction environment, great part of the research efforts have been focusing on the development of suitable OC materials [49]. In detail, the requirements for an appropriate OC are a high oxygen carrying capacity on a mass basis, high selectivity towards the desired products, high oxygen mobility inside the crystalline lattice, fast kinetics, good heat carrying capacity, high attrition resistance, low toxicity, suitable long-term stability and low production costs [50]. Several different metal oxides have been investigated for CLR, such as NiO [51-53], CeO_2 [54, 55], Fe_2O_3 [35, 56, 57], spinel-type mixed oxides [58, 59] and perovskite-type oxides [60-63]. Figure 1.11 summarizes the properties of the most investigated metal oxides for CLR. Iron-based oxygen carriers are particularly attractive for CLR, given their lower cost in respect of other transition metals such as Ni and Co, and their environmentally friendly nature [64], although they generally suffer from a lower reactivity towards hydrocarbons [65]. Many iron-containing oxides, from pure FeO_x [66] to spinels [67], perovskites [68], brownmillerites [69], and garnets [70] display a suitable equilibrium oxygen partial pressure, allowing for the selective oxidation of hydrocarbons to syngas in the reducer and the steam conversion to H_2 in the oxidizer. Moreover, various (raw and modified) natural minerals such as iron ore [71] and ilmenite [72], and industrial wastes such as red mud [73] and steel slag [74] were succesfully tested for this reaction. This large materials design space allows for the optimization of OCs to different process requirements, operating conditions and economical and environimental costraints. As a recent development in OC technology, multicomponent and multi-functional materials has been proposed and tested for CL applications to increase the system performance in a cost-effective manner while offering a high degree of flexibility [75-79]. The present work follow from these findings, focusing on the development of Ni-promoted Fe-based OC materials.

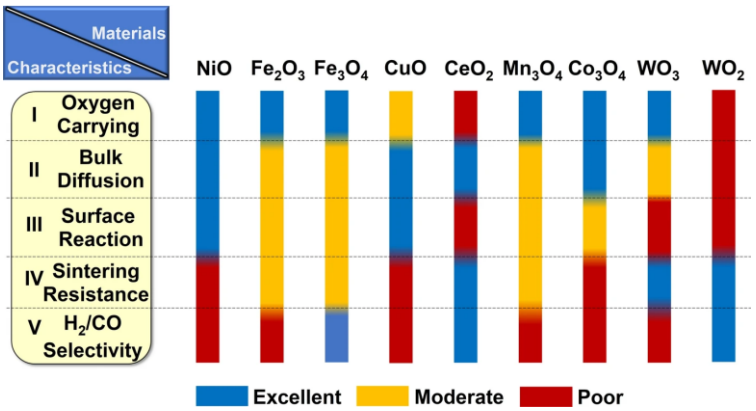

Fig. 1.11. Oxygen carrying capacity, bulk diffusion, surface reaction, sintering resistance, and H_2/CO selectivity characteristics of Ni, Fe, Cu, Ce, Mn, Co and W-based oxygen carriers [80].

1.3.4. Reaction principles

The gas-solid reactions taking place in all CL systems involve a complicated network of phenomena, rendering the accurate description of the OC materials in reaction conditions extremely challenging. Each subreaction of the CL cycle involves the generation (or consumption) of lattice oxygen vacancies, which may (or may not) be associated to a phase change of the solid. Since the reactions take place on the OC surface, large oxygen potential gradients can build up at the particle-scale, providing the driving force for oxygen anion diffusion inside the lattice. Consequently, the oxygen solid-state diffusion influences the reactivity by altering the availability of the solid reactants on the surface. Chemical potential gradients in turn determines the migration of the metallic cations and the formation of new phases. Lastly, the state of the surface, dynamically changing across the reaction step, determines the absorption and activation of the reactants and thus the catalytic properties. As an example, figure 1.12 provides a simplified schematization of the phenomena involved in the reduction of OC materials by carbonaceous fuels. Despite the complexity of the framework presented above, it is possible to effectively tune the behaviour of OCs making use of established design principles [80]. The ionic diffusion rate of crystalline phases such as perovskites can be tuned by altering the composition, thus modifying the selectivity towards total oxidation, partial oxidation, and pyrolysis of the fuel by adjusting the bulk-to-surface O^{2-} flux [81] and the superficial coordination environment of metallic cations [82, 83]. The metal to oxygen bond length in transition metals oxides can be altered by lattice doping, modifying both the oxygen release and transport properties, and improving OC reactivity [84]. The surface reaction rate can be improved by specifically introducing a catalytically active phase [85] or by producing it *in situ* alongside with the reduction of the OC, for example inducing the formation of a metallic phase from an oxide or making use of the redox exsolution phenomenon [86]. A careful design and optimization of OC materials should take in consideration these principles as much as possible to maximize the process performances.

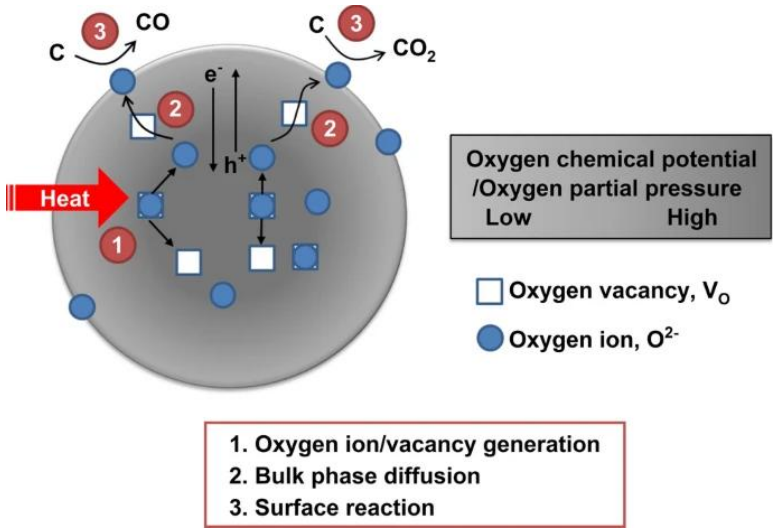

Fig. 1.12. Reaction principle of oxygen carriers under reducing environment [37].

1.4. References

[1] Jones, M. W., Peters, G. P., Gasser, T., Andrew, R. M., Schwingshackl, C., Gütschow, J., Houghton, R. A., Friedlingstein, P., Pongratz, J., & Quéré, C. L. (2023). National contributions to climate change due to historical emissions of carbon dioxide, methane, and nitrous oxide since 1850. Scientific Data, 10(1). https://doi.org/10.1038/s41597-023-02041-1.

[2] IPCC, 2023: Climate Change 2023: Synthesis Report. Contribution of Working Groups I, II and III to the Sixth Assessment Report of the Intergovernmental Panel on Climate Change [Core Writing Team, H. Lee and J. Romero (eds.)]. IPCC, Geneva, Switzerland, pp. 35-115, doi: 10.59327/IPCC/AR6-9789291691647.

[3] Magnan, A. K., Pörtner, H., Duvat, V. K. E., Garschagen, M., Guinder, V. A., Zommers, Z., Hoegh-Guldberg, O., & Gattuso, J. (2021). Estimating the global risk of anthropogenic climate change. *Nature Climate Change*, *11*(10), 879–885. https://doi.org/10.1038/s41558-021-01156-w

[4] Chiang, F., Mazdiyasni, O., & AghaKouchak, A. (2021). Evidence of anthropogenic impacts on global drought frequency, duration, and intensity. *Nature Communications*, *12*(1). https://doi.org/10.1038/s41467-021-22314-w

[5] IPCC, 2022: Climate Change 2022: Impacts, Adaptation and Vulnerability. Contribution of Working Group II to the Sixth Assessment Report of the Intergovernmental Panel on Climate Change [H.-O. örtner, D.C. Roberts, M. Tignor, E.S. Poloczanska, K. Mintenbeck, A. Alegría, M. Craig, S. Langsdorf, S. Löschke, V. Möller, A. Okem, B. Rama (eds.)]. Cambridge University Press. Cambridge University Press, Cambridge, UK and New York, NY, USA, 3056 pp., doi:10.1017/9781009325844.

[6] World Health Organization: WHO. (2023, October 12). *Climate change*. https://www.who.int/news-room/fact-sheets/detail/climate-change-and-health

[7] Mann, M. E. (2024, November 21). *Global warming | Definition, Causes, Effects, Solutions, & Facts*. Encyclopedia Britannica. https://www.britannica.com/science/global-warming

[8] Energy Institute. (2024). Home. Statistical Review of World Energy 2024. https://www.energyinst.org/statistical-review

[9] Wood, D. A., Nwaoha, C., & Towler, B. F. (2012). Gas-to-liquids (GTL): A review of an industry offering several routes for monetizing natural gas. *Journal of Natural Gas Science and Engineering, 9,* 196–208. https://doi.org/10.1016/j.jngse.2012.07.001

[10] Kemfert, C., Präger, F., Braunger, I., Hoffart, F. M., & Brauers, H. (2022). The expansion of natural gas infrastructure puts energy transitions at risk. *Nature Energy*, *7*(7), 582–587. https://doi.org/10.1038/s41560-022-01060-3

[11] Gürsan, C., & De Gooyert, V. (2020). The systemic impact of a transition fuel: Does natural gas help or hinder the energy transition? *Renewable and Sustainable Energy Reviews*, *138*, 110552. https://doi.org/10.1016/j.rser.2020.110552

[12] Brauers, H. (2022). Natural gas as a barrier to sustainability transitions? A systematic mapping of the risks and challenges. *Energy Research & Social Science*, *89*, 102538. https://doi.org/10.1016/j.erss.2022.102538

[13] McFarland, E. (2012). Unconventional chemistry for unconventional natural gas. *Science*, *338*(6105), 340–342. https://doi.org/10.1126/science.1226840

[14] Nesterenko, N., Medeiros-Costa, I., Clatworthy, E., Cruchade, H., Konnov, S., Dath, J., Gilson, J., & Mintova, S. (2023). Methane-to-chemicals: a pathway to decarbonization. *National Science Review*, *10*(9). https://doi.org/10.1093/nsr/nwad116

[15] Kapsalyamova, Z., & Paltsev, S. (2020). Use of natural gas and oil as a source of feedstocks. *Energy Economics*, *92*, 104984. https://doi.org/10.1016/j.eneco.2020.104984

[16] Liu, J., Yang, Y., Goetjen, T. A., & Hupp, J. T. (2022). Carbon-efficient conversion of natural gas and natural-gas condensates to chemical products and intermediate feedstocks via catalytic metal–organic framework (MOF) chemistry. *Energy & Environmental Science*, *15*(7), 2819–2842. https://doi.org/10.1039/d2ee01010k

[17] Franz, R., Uslamin, E. A., & Pidko, E. A. (2021). Challenges for the utilization of methane as a chemical feedstock. *Mendeleev Communications*, *31*(5), 584–592. https://doi.org/10.1016/j.mencom.2021.09.002

[18] Galvita, V., Bos, R., & Buelens, L. (2023). Methane conversion routes. In *Royal Society of Chemistry eBooks*. https://doi.org/10.1039/9781839160257

[19] *Greenhouse gas emissions by country and sector (infographic) | Topics | European Parliament*. (2018, July 3). Topics | European Parliament. https://www.europarl.europa.eu/topics/en/article/20180301STO98928/greenhouse-gas-emissions-by-country-and-sector-infographic.

[20] *The outlook for biogas and biomethane to 2040 – Outlook for biogas and biomethane: Prospects for organic growth – Analysis - IEA*. (2021). IEA. https://www.iea.org/reports/outlook-for-biogas-and-biomethane-prospects-for-organic-growth/the-outlook-for-biogas-and-biomethane-to-2040.

[21] IEA (2019), World Energy Outlook 2019, IEA, Paris. https://www.iea.org/reports/world-energy-outlook-2019

[22] World Bank Group. (2023). Global Gas Flaring Tracker Report. In *World Bank*. https://www.worldbank.org/en/topic/extractiveindustries/publication/2023-global-gas-flaring-tracker-report

[23] *Global average levelised cost of hydrogen production by energy source and technology, 2019 and 2050 – Charts – Data & Statistics - IEA*. (2020). IEA. https://www.iea.org/data-and-statistics/charts/global-average-levelised-cost-of-hydrogen-production-by-energy-source-and-technology-2019-and-2050

[24] Rostrup-Nielsen, J. R., Sehested, J., & Nørskov, J. K. (2002). Hydrogen and synthesis gas by steam- and CO_2 reforming. In *Advances in catalysis* (pp. 65–139). https://doi.org/10.1016/s0360-0564(02)47006-x

[25] Amhamed, A. I., Qarnain, S. S., Hewlett, S., Sodiq, A., Abdellatif, Y., Isaifan, R. J., & Alrebei, O. F. (2022). Ammonia Production Plants—A Review. *Fuels*, *3*(3), 408–435. https://doi.org/10.3390/fuels3030026

[26] Boerrigter, H., & Rauch, R. (2006). Review of applications of gases from biomass gasification. ECN Biomassa, Kolen en Milieuonderzoek, 20, 211-230.

[27] Hydrogen strategy (2020), U.S. Department of Energy, Washington, DC. https://www.energy.gov/sites/prod/files/2020/07/f76/USDOE_FE_Hydrogen_Strategy_July2020.pdf

[28] He, D., Zhang, Y., Wang, Z., Mei, Y., & Jiang, Y. (2020). Bi-reforming of Methane with Carbon Dioxide and Steam on Nickel-Supported Binary Mg–Al Metal Oxide Catalysts. *Energy & Fuels*, *34*(4), 4822–4827. https://doi.org/10.1021/acs.energyfuels.9b03312

[29] Rostrup-Nielsen, J. R. (2000b). New aspects of syngas production and use. *Catalysis Today*, *63*(2–4), 159–164. https://doi.org/10.1016/s0920-5861(00)00455-7

[30] Saeidi, S., Fazlollahi, F., Najari, S., Iranshahi, D., Klemeš, J. J., & Baxter, L. L. (2016). Hydrogen production: Perspectives, separation with special emphasis on kinetics of WGS reaction: A state-of-the-art review. *Journal of Industrial and Engineering Chemistry*, *49*, 1–25. https://doi.org/10.1016/j.jiec.2016.12.003

[31] Sircar, S., & Golden, T. C. (2000). Purification of hydrogen by pressure swing adsorption. *Separation Science and Technology*, *35*(5), 667–687. https://doi.org/10.1081/ss-100100183

[32] Fan, L. (2017). *Chemical looping partial oxidation: Gasification, Reforming, and Chemical Syntheses*. Cambridge University Press.

[33] Metcalfe, I. S., Ray, B., Dejoie, C., Hu, W., De Leeuwe, C., Dueso, C., García-García, F. R., Mak, C., Papaioannou, E. I., Thompson, C. R., & Evans, J. S. O. (2019). Overcoming chemical equilibrium limitations using a thermodynamically reversible chemical reactor. *Nature Chemistry*, *11*(7), 638–643. https://doi.org/10.1038/s41557-019-0273-2

[34] Ishida, M., Zheng, D., & Akehata, T. (1987). Evaluation of a chemical-looping-combustion power-generation system by graphic exergy analysis. *Energy*, *12*(2), 147–154. https://doi.org/10.1016/0360-5442(87)90119-8

[35] Bhavsar, S., & Veser, G. (2014). Chemical looping beyond combustion: production of synthesis gas via chemical looping partial oxidation of methane. *RSC Advances*, *4*(88), 47254–47267. https://doi.org/10.1039/c4ra06437b

[36] Guan, Y., Liu, Y., Lin, X., Wang, B., & Lyu, Q. (2022). Research Progress and Perspectives of Solid Fuels Chemical Looping Reaction with Fe-Based Oxygen Carriers. *Energy & Fuels*, *36*(23), 13956–13984. https://doi.org/10.1021/acs.energyfuels.2c02802

[37] Zheng, H., Jiang, X., Gao, Y., Tong, A., & Zeng, L. (2022). Chemical looping reforming: process fundamentals and oxygen carriers. *Discover Chemical Engineering*, *2*(1). https://doi.org/10.1007/s43938-022-00012-3

[38] Luongo, G., Donat, F., Bork, A. H., Willinger, E., Landuyt, A., & Müller, C. R. (2022). Highly Selective Oxidative Dehydrogenation of Ethane to Ethylene via Chemical Looping with Oxygen Uncoupling through Structural Engineering of the Oxygen Carrier. *Advanced Energy Materials*, *12*(23). https://doi.org/10.1002/aenm.202200405

[39] Brown, S., & Hu, J. (2023). Review of chemical looping ammonia synthesis materials. *Chemical Engineering Science*, *280*, 119063. https://doi.org/10.1016/j.ces.2023.119063

[40] Zhang, J., He, T., Wang, Z., Zhu, M., Zhang, K., Li, B., & Wu, J. (2017). The search of proper oxygen carriers for chemical looping partial oxidation of carbon. *Applied Energy*, *190*, 1119–1125. https://doi.org/10.1016/j.apenergy.2017.01.024

[41] Luo, M., Yi, Y., Wang, S., Wang, Z., Du, M., Pan, J., & Wang, Q. (2017). Review of hydrogen production using chemical-looping technology. *Renewable and Sustainable Energy Reviews*, *81*, 3186–3214. https://doi.org/10.1016/j.rser.2017.07.007

[42] Luo, M., Yi, Y., Wang, S., Wang, Z., Du, M., Pan, J., & Wang, Q. (2017). Review of hydrogen production using chemical-looping technology. *Renewable and Sustainable Energy Reviews*, *81*, 3186–3214. https://doi.org/10.1016/j.rser.2017.07.007

[43] Mihai, O., Chen, D., & Holmen, A. (2012). Chemical looping methane partial oxidation: The effect of the crystal size and O content of $LaFeO_3$. *Journal of Catalysis*, *293*, 175–185. https://doi.org/10.1016/j.jcat.2012.06.022

[44] Shah, V., Mohapatra, P., & Fan, L. (2020). Thermodynamic and process analyses of Syngas production using chemical looping reforming assisted by flexible dicalcium Ferrite-Based oxygen carrier regeneration. *Energy & Fuels*, *34*(5), 6490–6500. https://doi.org/10.1021/acs.energyfuels.0c00479

[45] Rydén, M., Lyngfelt, A., & Mattisson, T. (2008). Chemical-Looping combustion and Chemical-Looping reforming in a circulating Fluidized-Bed reactor using Ni-Based oxygen carriers. *Energy & Fuels*, *22*(4), 2585–2597. https://doi.org/10.1021/ef800065m

[46] Zhou, Q., Zeng, L., & Fan, L. (2013). Syngas chemical looping process: Dynamic modelling of a moving-bed reducer. *AIChE Journal*, *59*(9), 3432–3443. https://doi.org/10.1002/aic.14181

[47] Spallina, V., Marinello, B., Gallucci, F., Romano, M., & Van Sint Annaland, M. (2016). Chemical looping reforming in packed-bed reactors: Modelling, experimental validation and large-scale reactor design. *Fuel Processing Technology*, *156*, 156–170. https://doi.org/10.1016/j.fuproc.2016.10.014

[48] Luo, S., Zeng, L., & Fan, L. (2015). Chemical looping Technology: oxygen carrier characteristics. *Annual Review of Chemical and Biomolecular Engineering*, *6*(1), 53–75. https://doi.org/10.1146/annurev-chembioeng-060713-040334

[49] Tian, M., Wang, C., Han, Y., & Wang, X. (2020). Recent advances of oxygen carriers for chemical looping reforming of methane. *ChemCatChem*, *13*(7), 1615–1637. https://doi.org/10.1002/cctc.202001481

[50] De Vos, Y., Jacobs, M., Van Der Voort, P., Van Driessche, I., Snijkers, F., & Verberckmoes, A. (2020). Development of Stable Oxygen Carrier Materials for Chemical Looping Processes—A Review. *Catalysts*, *10*(8), 926. https://doi.org/10.3390/catal10080926

[51] Rydén, M., Lyngfelt, A., & Mattisson, T. (2006). Synthesis gas generation by chemical-looping reforming in a continuously operating laboratory reactor. *Fuel*, *85*(12–13), 1631–1641. https://doi.org/10.1016/j.fuel.2006.02.004

[52] Ortiz, M., De Diego, L. F., Abad, A., García-Labiano, F., Gayán, P., & Adánez, J. (2009). Hydrogen production by auto-thermal chemical-looping reforming in a pressurized fluidized bed reactor using Ni-based oxygen carriers. *International Journal of Hydrogen Energy*, *35*(1), 151–160. https://doi.org/10.1016/j.ijhydene.2009.10.068

[53] Feng, Y., Wang, N., & Guo, X. (2018). Influence mechanism of supports on the reactivity of Ni-based oxygen carriers for chemical looping reforming: A DFT study. *Fuel*, *229*, 88–94. https://doi.org/10.1016/j.fuel.2018.04.160

[54] Gao, X., Vidal, A., Bayon, A., Bader, R., Hinkley, J., Lipiński, W., & Tricoli, A. (2016). Efficient ceria nanostructures for enhanced solar fuel production via high-temperature thermochemical redox cycles. *Journal of Materials Chemistry A*, *4*(24), 9614–9624. https://doi.org/10.1039/c6ta02187e

[55] Nair, M. M., & Abanades, S. (2016). Tailoring hybrid nonstoichiometric Ceria Redox cycle for combined solar methane reforming and thermochemical conversion of H_2O/CO_2. *Energy & Fuels*, *30*(7), 6050–6058. https://doi.org/10.1021/acs.energyfuels.6b01063

[56] Galvita, V. V., Poelman, H., Bliznuk, V., Detavernier, C., & Marin, G. B. (2013). CeO_2-Modified Fe_2O_3 for CO_2 utilization via chemical looping. *Industrial & Engineering Chemistry Research*, *52*(25), 8416–8426. https://doi.org/10.1021/ie4003574

[57] Lu, C., Li, K., Wang, H., Zhu, X., Wei, Y., Zheng, M., & Zeng, C. (2017). Chemical looping reforming of methane using magnetite as oxygen carrier: Structure evolution and reduction kinetics. *Applied Energy*, *211*, 1–14. https://doi.org/10.1016/j.apenergy.2017.11.049

[58] Imtiaz, Q., Yüzbasi, N. S., Abdala, P. M., Kierzkowska, A. M., Van Beek, W., Broda, M., & Müller, C. R. (2015). Development of $MgAl_2O_4$-stabilized, Cu-doped, Fe_2O_3-based oxygen carriers for thermochemical water-splitting. *Journal of Materials Chemistry A*, *4*(1), 113–123. https://doi.org/10.1039/c5ta06753g

[59] Huang, J., Liu, W., Yang, Y., & Liu, B. (2018). High-Performance Ni–Fe redox catalysts for selective CH_4 to syngas conversion via chemical looping. *ACS Catalysis*, *8*(3), 1748–1756. https://doi.org/10.1021/acscatal.7b03964

[60] Zhang, X., Pei, C., Chang, X., Chen, S., Liu, R., Zhao, Z., Mu, R., & Gong, J. (2020). FeO_6 Octahedral Distortion Activates Lattice Oxygen in Perovskite Ferrite for Methane Partial Oxidation Coupled with CO_2 Splitting. *Journal of the American Chemical Society*, *142*(26), 11540–11549. https://doi.org/10.1021/jacs.0c04643

[61] Chang, H., Bjørgum, E., Mihai, O., Yang, J., Lein, H. L., Grande, T., Raaen, S., Zhu, Y., Holmen, A., & Chen, D. (2020). Effects of oxygen mobility in La–Fe-Based perovskites on the catalytic activity and selectivity of methane oxidation. *ACS Catalysis*, *10*(6), 3707–3719. https://doi.org/10.1021/acscatal.9b05154

[62] Li, M., Zhao, K., Zhao, Z., Li, H., He, F., & Lv, P. (2019). Enhanced hydrogen-rich syngas generation in chemical looping methane reforming using an interstitial doped $La_{1.6}Sr_{0.4}FeCoO_6$. *International Journal of Hydrogen Energy*, *44*(21), 10250–10264. https://doi.org/10.1016/j.ijhydene.2019.03.012

[63] Neal, L., Shafiefarhood, A., & Li, F. (2015). Effect of core and shell compositions on $MeO@La_xSr_{1-x}FeO_3$ core–shell redox catalysts for chemical looping reforming of methane. *Applied Energy*, *157*, 391–398. https://doi.org/10.1016/j.apenergy.2015.06.028

[64] Yu, Z., Yang, Y., Yang, S., Zhang, Q., Zhao, J., Fang, Y., Hao, X., & Guan, G. (2018). Iron-based oxygen carriers in chemical looping conversions: A review. *Carbon Resources Conversion*, *2*(1), 23–34. https://doi.org/10.1016/j.crcon.2018.11.004

[65] Bhavsar, S., & Veser, G. (2013). Bimetallic Fe–Ni oxygen carriers for chemical looping combustion. *Industrial & Engineering Chemistry Research*, *52*(44), 15342–15352. https://doi.org/10.1021/ie400612g

[66] García-García, & Metcalfe, I. (2021). Chemical looping dry reforming of methane using mixed oxides of iron and cerium: Operation window. *Catalysis Communications*, *160*, 106356. https://doi.org/10.1016/j.catcom.2021.106356

[67] Vozniuk, O., Tanchoux, N., Millet, J., Albonetti, S., Di Renzo, F., & Cavani, F. (2019). Spinel Mixed Oxides for Chemical-Loop Reforming: From Solid State to Potential Application. In *Studies in surface science and catalysis* (pp. 281–302). https://doi.org/10.1016/b978-0-444-64127-4.00014-8

[68] Dawa, T., & Sajjadi, B. (2023). Exploring the potential of perovskite structures for chemical looping technology: A state-of-the-art review. *Fuel Processing Technology*, *253*, 108022. https://doi.org/10.1016/j.fuproc.2023.108022

[69] Sukma, M. S., Zheng, Y., Hodgson, P., & Scott, S. A. (2022). Understanding the Behavior of Dicalcium Ferrite ($Ca_2Fe_2O_5$) in Chemical Looping Syngas Production from CH_4. *Energy & Fuels*, *36*(17), 9410–9422. https://doi.org/10.1021/acs.energyfuels.2c01065

[70] Kang, Y., Han, Y., Tian, M., Huang, C., Wang, C., Lin, J., Hou, B., Su, Y., Li, L., Wang, J., & Wang, X. (2020). Promoted methane conversion to syngas over Fe-based garnets via chemical looping. *Applied Catalysis B Environment and Energy*, *278*, 119305. https://doi.org/10.1016/j.apcatb.2020.119305

[71] Gu, H., Cui, X., Wang, J., Li, W., Wu, X., Wang, L., Zhao, S., Qiao, Z., & Niu, M. (2021). Natural Iron Ore as Oxygen Carrier Modified with Rare Earth Metal for Chemical Looping Hydrogen Production. *Energy & Fuels*, *35*(18), 15234–15242. https://doi.org/10.1021/acs.energyfuels.1c02105

[72] Sun, Z., Rasi, N. M., Lu, D. Y., Symonds, R. T., Mahinpey, N., Wu, B., & Duan, L. (2023). Chemical looping reforming for syngas production with co-conversion of CH_4 and CO_2 by using ilmenite ore as both oxygen carrier and catalyst. *Chemical Engineering Science*, *280*, 119050. https://doi.org/10.1016/j.ces.2023.119050

[73] Ma, S., Cheng, F., Meng, J., Ge, H., Lu, P., & Song, T. (2022). Ni-enhanced red mud oxygen carrier for chemical looping steam methane reforming. *Fuel Processing Technology*, *230*, 107204. https://doi.org/10.1016/j.fuproc.2022.107204

[74] Hildor, F., Leion, H., Linderholm, C. J., & Mattisson, T. (2020). Steel converter slag as an oxygen carrier for chemical-looping gasification. *Fuel Processing Technology*, *210*, 106576. https://doi.org/10.1016/j.fuproc.2020.106576

[75] Shafiefarhood, A., Hamill, J. C., Neal, L. M., & Li, F. (2015). Methane partial oxidation using $FeO_x@La_{0.8}Sr_{0.2}FeO_{3-\delta}$ core–shell catalyst – transient pulse studies. *Physical Chemistry Chemical Physics*, *17*(46), 31297–31307. https://doi.org/10.1039/c5cp05583k

[76] Hu, J., Galvita, V., Poelman, H., & Marin, G. (2018). Advanced Chemical looping Materials for CO_2 utilization: A review. *Materials*, *11*(7), 1187. https://doi.org/10.3390/ma11071187

[77] Hu, J., Galvita, V. V., Poelman, H., Detavernier, C., & Marin, G. B. (2019). Pressure-induced deactivation of core-shell nanomaterials for catalyst-assisted chemical looping. *Applied Catalysis B Environment and Energy*, *247*, 86–99. https://doi.org/10.1016/j.apcatb.2019.01.084

[78] Zeng, D., Qiu, Y., Li, M., Ma, L., Cui, D., Zhang, S., & Xiao, R. (2020). Spatially controlled oxygen storage materials improved the syngas selectivity on chemical looping methane conversion. *Applied Catalysis B Environment and Energy*, *281*, 119472. https://doi.org/10.1016/j.apcatb.2020.119472

[79] More, A., & Veser, G. (2016). Physical mixtures as simple and efficient alternative to alloy carriers in chemical looping processes. *AIChE Journal*, *63*(1), 51–59. https://doi.org/10.1002/aic.15380

[80] Zheng, H., Jiang, X., Gao, Y., Tong, A., & Zeng, L. (2022b). Chemical looping reforming: process fundamentals and oxygen carriers. *Discover Chemical Engineering*, *2*(1). https://doi.org/10.1007/s43938-022-00012-3

[81] Neal, L. M., Shafiefarhood, A., & Li, F. (2014). Dynamic methane partial oxidation using a Fe_2O_3@$La_{0.8}Sr_{0.2}FeO_{3-\Delta}$ Core–Shell Redox catalyst in the absence of gaseous oxygen. *ACS Catalysis*, *4*(10), 3560–3569. https://doi.org/10.1021/cs5008415

[82] Yang, J., Bjørgum, E., Chang, H., Zhu, K., Sui, Z., Zhou, X., Holmen, A., Zhu, Y., & Chen, D. (2021). On the ensemble requirement of fully selective chemical looping methane partial oxidation over La-Fe-based perovskites. *Applied Catalysis B Environment and Energy*, *301*, 120788. https://doi.org/10.1016/j.apcatb.2021.120788

[83] Liu, Y., Qin, L., Cheng, Z., Goetze, J. W., Kong, F., Fan, J. A., & Fan, L. (2019). Near 100% CO selectivity in nanoscaled iron-based oxygen carriers for chemical looping methane partial oxidation. *Nature Communications*, *10*(1). https://doi.org/10.1038/s41467-019-13560-0

[84] Qin, L., Cheng, Z., Guo, M., Xu, M., Fan, J. A., & Fan, L. (2016). Impact of 1% Lanthanum Dopant on Carbonaceous Fuel Redox Reactions with an Iron-Based Oxygen Carrier in Chemical Looping Processes. *ACS Energy Letters*, *2*(1), 70–74. https://doi.org/10.1021/acsenergylett.6b00511

[85] Zheng, Y., Sukma, M. S., & Scott, S. A. (2023). The exploration of $NiO/Ca_2Fe_2O_5/CaO$ in chemical looping methane conversion for syngas and H_2 production. *Chemical Engineering Journal*, *465*, 142779. https://doi.org/10.1016/j.cej.2023.142779

[86] Hosseini, D., Donat, F., Abdala, P. M., Kim, S. M., Kierzkowska, A. M., & Müller, C. R. (2019). Reversible exsolution of dopant improves the performance of $Ca_2Fe_2O_5$ for chemical looping hydrogen production. *ACS Applied Materials & Interfaces*, *11*(20), 18276–18284. https://doi.org/10.1021/acsami.8b16732

2. Experimental methods

Purpose of this chapter is to provide an overview of the synthesis, characterization and testing methods adopted throughout the PhD research work. Hereby will be described the experimental procedures adopted in multiple chapters of the text, while specific techniques used in particular instances are discussed separately in their respective chapters. While most of the synthesis and characterization methods are standard techniques widely employed in the materials science, catalysis and chemical engineering fields, the experimental setup used for CL-SMR testing was developed, built, and optimized on-purpose. A brief description of the setup is provided in the last section of the chapter.

2.1. Materials synthesis

Commercial ZrO_2 (MEL chemicals) and CeO_2 (Umicore) were used throughout chapters 2 and 3 as reference supports. Other oxides investigated within this study were prepared as described below:

$Ca_2Fe_2O_5$ (C2F) was synthesized by the coprecipitation method, following the procedure reported in [1]. 1M solutions of $Fe(NO_3)_3 \cdot 9H_2O$ (Treibacher Industrie A.G.) and $Ca(NO_3)_2 \cdot 4H_2O$ (Sigma Aldrich) were prepared and mixed in ratio 1:1. Then, the solution was stirred at ambient temperature for 20 min. Thereafter, a 0.5M NaOH (Sigma Aldrich) and 0.5M $NaCO_3$ (Carlo Erba) solution was added dropwise under vigorous stirring until reaching a pH of 12.5. The slurry was then aged under constant stirring for 6h at ambient temperature and then filtered and washed four times with distilled water. The cake was dried at 100 °C for 12 h and calcined at 1150 °C (ramp 10 °C/min) in a dry air flow for 6h.

$Ca_2Fe_{1.95}Ni_{0.05}O_5$ was synthesized via a modified Pechini method, following the procedure reported in [2]. 1M solutions of $Fe(NO_3)_3 \cdot 9H_2O$ (Treibacher Industrie A.G.), $Ca(NO_3)_2 \cdot 4H_2O$ (Sigma Aldrich) and $Ni(NO_3)_2 \cdot 6H_2O$ (VWR chemicals) were prepared and mixed according to the desired stoichiometry. The solution was stirred at ambient temperature for 20 min. Then citric acid (Sigma Aldrich) and ethylene glycol (VWR Chemicals) were added to obtain citric acid:metal ion and ethylene glycol:citric acid molar ratios of 1. The obtained solution was kept at 60 °C for 2 h under constant stirring. The obtained gel was then dried for 12 h at 220 °C, and successively calcined at 950 °C for 3 h, using a ramp rate of 5°C/min.

$Ce_{0.8}Zr_{0.2}O_2$ (CZ) was synthesized by coprecipitation in presence of H_2O_2 following a procedure previously developed in our group [3]. $Ce(NO_3)_3 \cdot 6H_2O$ (Treibacher Industrie A.G.) and $ZrO(NO_3)_2$ solution (Treibacher Industrie A.G.) were separately dissolved/diluted to obtain 0.2M solutions. The solutions were then mixed according to the desired stoichiometry and stirred for 15 min. H_2O_2 (Sigma Aldrich, 35%) was then added to obtain a H_2O_2:metal cations molar ratio of 3. The obtained solution was stirred for additional 45 minutes. To induce precipitation, NH_3 solution (Sigma Aldrich, 30%) was then added dropwise until the pH reached a value of 10.5. The slurry was aged under constant stirring for 4h at ambient temperature and then filtered and washed four times with deionized water. The cake was dried at 100 °C for 12 h and calcined at 500 °C (ramp 10 °C/min) in a dry air

flow for 3 h. A further calcination step at 850 °C (ramp 10 °C/min) in a dry air flow for 3h was then performed to stabilize the morphological features of the obtained powder.

CeO_2-Al_2O_3 was synthesized following a procedure analogous to that of CZ. $Ce(NO_3)_3 \cdot 6H_2O$ (Treibacher Industrie A.G.) and $Al(NO_3)_3 \cdot 9H_2O$ (Sigma Aldrich) were separately dissolved to obtain a 0.2 M and 0.4 M solution respectively. The solutions were then mixed according to the desired stoichiometry and stirred for 15 min. H_2O_2 (Sigma Aldrich, 35%) was then added to obtain a H_2O_2:metal cations molar ratio of 3. The obtained solution was stirred for additional 45 min. To induce precipitation, NH_4OH solution (Sigma Aldrich, 30%) was then added dropwise until the pH reached a value of 10.5. The slurry was then aged under constant stirring for 4 h at ambient temperature and then filtered and washed four times with distilled water. The cake was dried at 100 °C for 12 h and calcined at 500 °C (ramp 10 °C/min) in a dry air flow for 3 h. The powder was then grinded with agate mortar and pestle and subjected to an additional calcination step at 850 °C (ramp 10 °C/min) in a dry air flow for 3 h was performed.

CeO_2-SiO_2 was synthesized via coprecipitation/hydrolysis in ethanol. $Ce(NO_3)_3 \cdot 6H_2O$ (Treibacher Industrie A.G.) was dissolved in absolute ethanol (Sigma Aldrich). Tetraethyl orthosilicate (TEOS, Fluka) was then added to the solution in stoichiometric amount. The obtained solution was continuously stirred for 2 h. Then, an excess amount of NH_3 solution (Sigma Aldrich, 30%) was rapidly added to the solution to induce the precipitation of Ce and the hydrolysis of the TEOS. The slurry was then stirred at 60 °C for 1 h and then dried in an oven for 12 h at 100 °C. The calcination was carried on heating the powders to 220 °C (ramp 2 °C/min) and held for 30 min to decompose NH_4NO_3, and then heating up to 500 °C (ramp 5 °C/min) for 3 h. The powder was then grinded with agate mortar and pestle and subjected to an additional calcination step at 850 °C (ramp 10 °C/min) in a dry air flow for 3 h afterwards.

Ni-loaded materials were prepared by conventional incipient wetness impregnation. An aqueous solution was prepared dissolving $Ni(NO_3)_2 \cdot 6H_2O$ (VWR chemicals) in an appropriate amount of deionized water. The amount of liquid needed to fully wet the powders was determined prior to the impregnation. The solution was poured drop by drop over the powders, frequently homogenizing the obtained paste with the aid of a pestle. The paste was then dried for 6 h at 100 °C and calcined at 500°C for 1 h (ramp 10 °C/min) to decompose the Ni precursor.

$Sr_2FeMo_{0.6}Ni_{0.4}O_6$ (SFMN) powders were prepared using a citrate auto-combustion route. $Sr(NO_3)_2$ (Sigma Aldrich), $Fe(NO_3)_3$ (Treibacher Industrie A.G.), $(NH_4)_6Mo_7O_{24} \cdot 6H_2O$ (Carlo Erba), and $Ni(NO_3)_2 \cdot 6H_2O$ (VWR chemicals) were separately dissolved in deionized water. To avoid possible inhomogeneous precipitation the nitrate solutions of Sr, Fe and Ni were mixed and stirred for 15 minutes before adding Mo solution. Citric acid (Sigma Aldrich) was employed as the complexing agent, with a citric acid-to-cations molar ratio of 2:1. After adding the Citric Acid, the pH was adjusted to 8 using an ammonium hydroxide solution (30% wt.). The solution was then stirred and dried at 80 °C for 24 h. The temperature of resulting gel was set to 350 °C to allow auto-ignition, and the powders were then collected and finely ground in an agate mortar and calcinated at 1100 °C for 10 h (ramp 10 °C/min).

2.2. Materials characterization

The materials, both in their prepared state and after testing, have been characterized in terms of their physicochemical and functional properties. The standard operating conditions for conventional characterization are outlined below. Additional experimental details will be provided in subsequent chapters, as needed, to justify the methodological approach employed to achieve the desired objectives.

2.2.1. Characterisation of chemical and physical properties

Morphological, structural, nanostructural and surface properties of oxides were investigated by porosimetry, adsorption techniques, X ray diffractometry, electron microscopy and X-ray photoelectron spectroscopy.

The superficial area and pore volume of pristine $Ca_2Fe_2O_5$ were determined by Mercury Intrusion Porosimetry (MIP) in a Micromeritics AutoPore IV 9500 porosimeter.

The superficial area and pore volume of Zr and Ce-containing materials was determined using a Micromeritics Tristar porosimeter by analysing N_2 adsorption isotherm at 77 K using the Brunauer-Emmet-Teller (BET) method. Samples were degassed by maintaining them at 0.15 mbar and 150 °C for 1.5 h prior to the analysis.

Powders X-ray Diffraction (XRD) patterns discussed in chapter 3 were acquired at the Technical University of Eindhoven, Eindhoven (NL) on a Rigaku Miniflex diffractometer operating at 40 kV, 15 mA with a mobile Cu anode, equipped with a graphite monochromator. Diffraction patterns of samples used in chapters 4, 5 and 6 were acquired in a Philips X'Pert diffractometer equipped with an X'Celerator detector using Ni-filtered Cu Kα radiation (λ=1.542Å). Data were recorded in the 10-90 ° 2θ range with a step size of 0.02 ° and a counting time per step of 40 s. The average crystallite size was estimated using the Sherrer equation [4] (eq. 2.1, where D_p is the average crystallite size, K is the shape factor, set equal to 0.9, B_{obs} is the line broadening at half the maximum intensity and B_{strum} is the instrumental peak widening) and corrected for the instrumental peak widening using a silica standard.

$$D_p(\text{Å}) = \frac{K\,\lambda}{\sqrt{B_{obs}^2 - B_{strum}^2}\cos\theta} \qquad (2.1)$$

Scanning Electron Microscopy (SEM) images of C2F samples reported in chapter 3 were obtained at the Technical University of Eindhoven, Eindhoven (NL) using a Thermo Fisher Phenom proX G6 microscope, equipped with a built-in Energy Dispersive X-ray Spectroscopy (EDS) analyser for elemental mapping. SEM images of composite OC materials were acquired with a JEOL JSM7610F Plus Field Emission-Scanning Electron Microscope (FESEM), equipped with an EDS analyser. Prior to the analysis, the powders were ultrasonically dispersed in ethanol and poured on a gold sample holder.

Microstructural characterization by High-Angle Annular Dark Field Scanning Transmission Electron Microscopy (HAADF-STEM), High-Resolution Transmission Electron Microscopy (HRTEM) images and Energy Dispersive X-ray Spectroscopy (EDS) patterns were acquired at the Universitat Politècnica de Catalunya, Barcelona (ES), on a FEI Tecnai G2 F20 instrument equipped with a field emission gun operating at an accelerating voltage of 200 kV. Elemental mapping was performed with an EDS analyser. Prior to the analysis, samples were ultrasonically dispersed in ethanol and deposited onto a lacey carbon copper grid.

X-ray Photoelectron Spectroscopy (XPS) was performed with a SPECS system at the Universitat Politècnica de Catalunya, Barcelona (ES), using a Mg X-ray source and a 9-channel Phoibos detector at a pressure below 10^{-6} Pa. Quantification was carried out using CasaXPS software package, adopting spline Shirley baselines and Gaussian-Lorentzian lineshapes.

2.2.2. Characterization of redox properties

The evaluation of the reducibility of materials used throughout chapters 4 and 5 was investigated performing Temperature-Programmed Reductions (TPR) in 5% H_2 (balance N_2) atmosphere in a TA instruments Q500 Thermogravimetric Analyser (TGA). Approximately 15 mg of powdered sample were loaded into a platinum pan. Prior to the analysis, samples were held at 500 °C in pure N_2, to removed physisorbed species. Reductions were performed with a constant gas flow of 60 ml/min, heating the sample from 100 to 850 °C with a heating rate of 10 °C/min and holding the sample at the maximum temperature for 30 min.

CH_4-TPRs, isothermal CH_4 reduction and CL-SMR tests were performed in a custom-built laboratory setup. A schematic representation of the setup is provided in figure 2.1. The apparatus is equipped with a gas feeding system composed by 5 mass flow controllers (Brooks instruments). Steam was fed by flowing He in a jacketed saturator operating at a constant temperature of 50 °C. Gas lines to and from the reactor were heated to avoid steam condensation. Powdered samples were loaded into a quartz reactor with an internal diameter of 8 mm and placed inside the isothermal zone of an electrically heated furnace. Sample temperature was continuously monitored with a K-type thermocouple placed ~5mm above the sample. The reactor was connected to a calibrated mass spectrometer (Hiden Analytical HPR20). CH_4, H_2, CO, CO_2 and O_2 calibration factors were periodically corrected using standard mixtures. H_2O calibration factor was inferred from the H_2 consumption of the reduction of a known amount of CuO. The accuracy was monitored performing carbon balances, closed to within 10%. The mass spectrometer operative conditions were carefully fine-tuned to minimize the acquisition time, obtaining a scanning rate of 5 datapoints per minute for each mass signal acquired. The automated gas-switching valve system implemented in the setup, as shown in figure 2.1, was designed to allow for a fast interchange between different reactive mixtures. Valves were controlled by a microcontroller (Arduino Uno, Arduino) to ensure consistent steps duration and simultaneous valves operation. The pressure drop across the reactor bypass line was kept equal to the reactor pressure drop by manually operating the needle valved fitted on the former. Doing so, fast pressure oscillations due to valves opening and closing are avoided, providing a stable pressure value at the mass spectrometer inlet.

For CH_4-TPR experiments, 50 mg of sample were loaded into the reactor and heated up to 500 °C (ramp 10 °C/min) in pure He for 30 minutes to removed physisorbed species. Samples were then heated from 100 to 880 °C (ramp 10 °C/min) in 10% CH_4 in He and held for 15 minutes under the same feed at the maximum temperature. The samples were then oxidized by flowing ~10% steam for 11 minutes and successively 5% O_2 for 3 minutes and brought back to ambient temperature in pure He. The total flowrate was kept constant at 50 ml/min.

Isothermal CH_4 reduction experiments were conducted by loading 200 mg of sample in the reactor. Samples were heated to 800 °C (ramp 30 °C/min) in 5% O_2 and then exposed to 10% CH_4 in He. The total flowrate was kept constant at 50 ml/min.

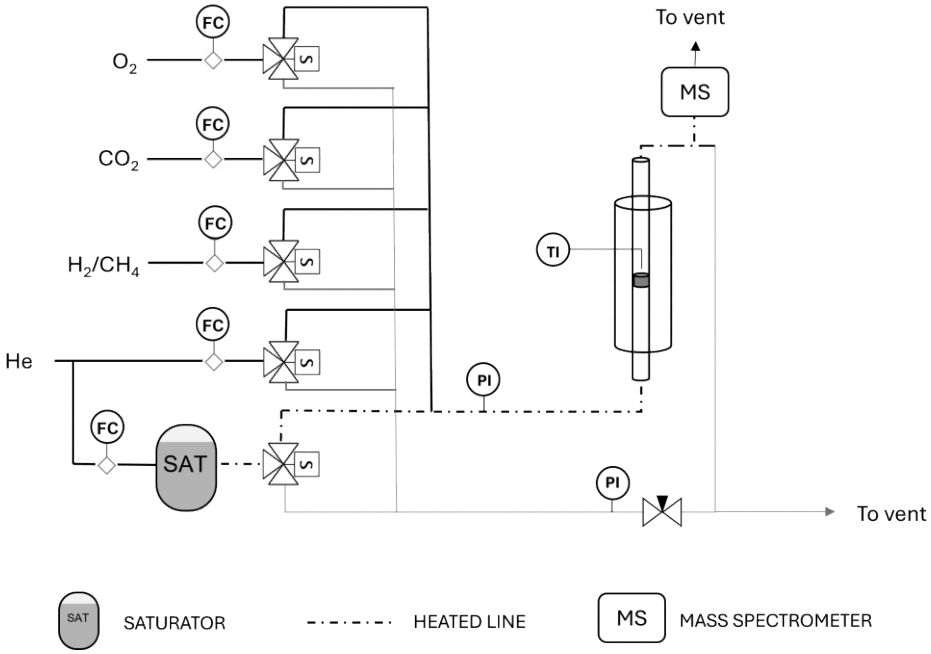

Fig. 2.1. Schematic representation of the experimental setup used throughout this thesis.

2.3. Chemical looping tests

Chemical Looping tests were performed in the same experimental setup depicted in figure 2.1. CL-SMR cycles were performed loading 200 mg of sample into the reactor and heating up to 800 °C (ramp 30 °C/min) in 5% O_2 in He. If not explicitly stated otherwise, CL-SMR cycles of chapters 4 and 5 were performed following the procedure reported in figure 2.2. With the chosen step times, the CH_4 to $Ca_2Fe_2O_5$ molar ratio is approximately equal to 3 (stoichiometrically, one mole of C2F can exchange 3 moles of atomic O). H_2O was fed in excess to ensure the full reoxidation of the OC material, since the steam conversion is equilibrium limited. The oxygen oxidation step was included to ensure the total reoxidation of the oxygen carrier material and the complete combustion of solid carbonaceous species that may have been formed by CH_4 pyrolysis. The total flowrate was kept constant at 50 ml/min, obtaining a spatial velocity of approximately 20'000 h^{-1}. At the end of the test, samples were brought to ambient temperature in a pure He flow.

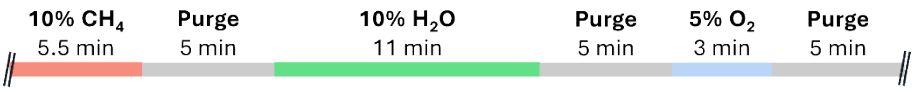

Fig. 2.2. Procedure adopted for performing standard CL-SMR cycles. He was used both as the carrier gas and the purge gas.

2.4. References

[1] Ismail, M., Liu, W., Chan, M. S. C., Dunstan, M. T., & Scott, S. A. (2016). Synthesis, application, and carbonation behavior of $Ca_2Fe_2O_5$ for chemical looping H2 production. Energy & Fuels, 30(8), 6220–6232. https://doi.org/10.1021/acs.energyfuels.6b00631

[2] Hosseini, D., Donat, F., Abdala, P. M., Kim, S. M., Kierzkowska, A. M., & Müller, C. R. (2019b). Reversible exsolution of dopant improves the performance of $Ca_2Fe_2O_5$ for chemical looping hydrogen production. *ACS Applied Materials & Interfaces*, *11*(20), 18276–18284. https://doi.org/10.1021/acsami.8b16732

[3] Moser, M., Vilé, G., Colussi, S., Krumeich, F., Teschner, D., Szentmiklósi, L., Trovarelli, A., & Pérez-Ramírez, J. (2015). Structure and reactivity of ceria–zirconia catalysts for bromine and chlorine production via the oxidation of hydrogen halides. *Journal of Catalysis*, *331*, 128–137. https://doi.org/10.1016/j.jcat.2015.08.024

[4] Scherrer, P. (1918). Bestimmung der Grosse und inneren Struktur von Kolloidteilchen mittels Rontgenstrahlen. Nach Ges Wiss Gottingen, 2, 8-100.

3. Reactivity of $Ca_2Fe_2O_5$ for chemical looping steam reforming under pressurized conditions

Abstract

$Ca_2Fe_2O_5$ (C2F) showed a great potential in chemical looping applications, due to its remarkable redox stability and its ability to be fully regenerated by H_2O, producing a pure H_2 stream. Many chemical looping (CL) processes, such as Water Splitting (CLWS) and Steam Methane Reforming (CL-SMR), can benefit significantly from operating at high pressure, as it reduces or eliminates the need for downstream products compression steps. Nevertheless, only a limited number of experimental investigations focused on high-pressure operation of CL systems. Here, the effect of pressure on the stability of C2F was explored, finding that the total pressure doesn't affect the cyclic performances of the OC material. A comprehensive kinetic model was developed for the reduction of C2F with H_2, taking into account the effect of temperature, pressure, and reactant molar fraction in the feed. The total pressure was found to have a minimal effect on the reduction kinetics, while the H_2 molar fraction determined the reduction kinetics at a given temperature.

3.1. Introduction

The urgency of climate change calls for the development of more sustainable and efficient pathways from hydrocarbon fuels to hydrogen (H_2) and chemicals. Chemical Looping Reforming (CLR) represents an energy conversion technology that offers relevant opportunities for process intensification, energy efficiency and reduction of capital costs [1-3]. CLR is a family of processes whose aim is the production of syngas from carbonaceous fuels. Generally, it consists in two or three interconnected reactors between which a reducible metal oxide, called the Oxygen Carrier (OC), circulates cyclically releasing and acquiring lattice oxygen. In the fuel reactor, the hydrocarbon feedstock is oxidized to syngas according to the reaction (3.1), which is generally endothermic.

$$C_xH_y + M_mO_n \rightleftharpoons xCO + y/2\,H_2 + MeO_{n-x} \qquad (3.1)$$

Given the large availability and low cost of natural gas resources [4], a significant part of the research efforts on CLR focuses on methane as fuel. In the latter case, the syngas produced from the fuel reactor has an H_2/CO ratio of about 2, and it is thus optimal for Gas-To-Liquid (GTL) applications, such as methanol production or Fischer-Tropsch synthesis [1]. Using steam as oxidant allows to produce a pure hydrogen stream from the oxidizer reactor by simple condensation of the unconverted steam. In this case, the process is generally referred as Chemical Looping Steam Methane Reforming (CL-SMR) [1]. A general depiction of the process is provided in figure 3.1.

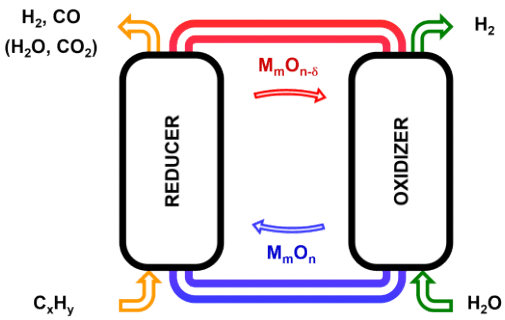

Fig. 3.1. Process scheme for fuel assisted CL-SMR with a generic metal oxide (M_mO_n) as OC and a generic hydrocarbon fuel (C_xH_y).

The development of suitable oxygen carriers is crucial for the deployment of CL-SMR processes at commercial scale, since the choice of the OC determines the fuel conversion (and the selectivity) of the reduction step, and the steam conversion at the oxidizer. Moreover, it determines the operative temperature and pressure ranges, and it largely affects the economics of the process. In this regard, iron oxides had been widely explored as OCs for their environmental friendliness, low cost, large OTC and suitable thermodynamics [5, 6]. When pure iron oxides are used, only Fe_3O_4-FeO and FeO-Fe transitions are suitable for CL-SMR [7], and the addition of a support is frequently necessary to overcome sintering and agglomeration of the active phase, particularly if large amounts of FeO and Fe are produced upon reduction [8-10]. The support plays a key role in providing high surface area for the active phase and a stable porous structure to facilitate intraparticle gas diffusion pathways. Moreover, the use of O^{2-} conductive supports can enhance the oxygen exchange kinetics of the active phase [9], leading to higher H_2 production from the water splitting step [11]. An alternative strategy to improve Fe-based OCs consists in confining the iron in stable and redox-active crystalline structures, such as perovskites, that can simultaneously increase the cyclic stability and the oxygen exchange rate [12, 13]. Among FeO_x promoters evaluated for stability improvement, CaO was found to effectively stabilize cyclic reduction/oxidation performance, and the formation of Ca ferrites, such as $Ca_2Fe_2O_5$ (C2F) in oxidizing conditions was observed [14]. The first application of C2F to CL-SMR is dated back to 2016 [15-17]. The interest in this material relied initially on its low equilibrium pO_2, which allows steam to completely oxidize Fe^0 to Fe^{3+}, and on the brownmillerite-type lattice structure, which facilitates fast oxygen ion transport [18, 19]. It was experimentally observed that all Ca-ferrite containing samples had better cyclic stability than pure FeO_x [4], with slight or no deactivation over cycles in a laboratory Fluidized Bed Reactor (FBR). Experimental studies confirmed that C2F reduction and oxidation follow a one-step pathway, as expected from thermodynamics [20]. H_2 reduction at ambient pressure was reported to be described by an Avrami-Erofeev random nucleation and growth model, with the Avrami exponent varying with the extent of OC conversion [21].

Taking in consideration that operating CL-SMR systems at high pressure is advantageous for both the oxidation and the reduction step, several papers have stressed the need for high pressure experimental evaluation of OCs reactivity [22-26]. Specifically, hydrogen production at pressurized conditions would raise the energy efficiency of the CL-SMR process due to the avoidance of its energy intensive compression [27], while GTL processes are operated at pressure higher than 10 bars (10-35 bar for Fischer-Tropsch synthesis, 40-100 bar for methanol production [24]), and direct pressurized syngas production can facilitate process couplings. Nevertheless, due to

the challenges related to operating laboratory setups with pressurized steam, few papers investigated OC behaviour at non-ambient pressure for CL-SMR systems [28-30].

Contradictory results were reported for the effect of total pressure on the reactivity of OCs. Various supported metal oxides were tested up to 30 bars, and a negative effect of the total pressure on reaction kinetics was reported for all the tested OCs and all the fuels used (H_2 and CO) [31, 32]. Similar results were obtained with CH_4 as the reducing agent [33]. Experiments carried on with TiO_2-Fe_2O_3 mixed oxides shown on the contrary a quasi-linear increase in reduction rates with total pressure for both H_2 and CH_4 reduction [34]. Steam oxidation experiments of supported iron oxides suggested that the total pressure doesn't affect significantly the water splitting kinetics [35]. The total pressure was found to also affect the stability of engineered catalyst-assisted OCs when employing methane as fuel, due to the pressure-induced enhancement of the CH_4 pyrolysis reaction [36]. These findings reflect the need for experimental investigations of OC behaviour at the actual forecasted operating conditions of CL processes, given the non-trivial effect of pressure on OC reactivity and stability.

The present work focuses on the effect of absolute pressure up to 20 bars on H_2-reduction (typically used as reducing agent in place of CH_4 to explore the material redox activity while by-passing cracking and carbon deposition phenomena [37]) and H_2O-oxidation of C2F. Aim of the study is the assessment of $Ca_2Fe_2O_5$-based OCs behaviour in terms of performance and stability at operating conditions relevant to practical industrial applications, providing information that can help guiding the design of larger scale pressurized CL-SMR systems. The experimental investigation was carried on in a high-pressure thermogravimetric analyser (HP-TGA) at the Technical University of Eindhoven, Eindhoven (NL).

3.2. Experimental

The details on samples preparation and characterization methods are reported in chapter 2. For the determination of the reduction kinetics, the C2F powders were pelletized applying a 5 tons static load. Pellets were then crushed and sieved between 0.2-0.4 mm.

Thermogravimetric analysis

The reactivity experiments have been carried in a custom-built high-pressure thermogravimetric analyser (HP-TGA) able to operate at pressures up to 30 bar and total flowrate up to 10 Nl/min. N_2 was used as carrier gas. All temperature variations, including sample heating from ambient to reaction temperature, were carried on under a N_2 atmosphere with 15 °C/min ramps. N_2 was sent between each reduction and oxidation step to avoid mixing of the reactants inside the TGA tube. Gas flow rates were controlled by mass flow controllers (Bronkhorst). H_2O was supplied as a liquid by a mass flow controller (Bronkhorst) and fed to a steam generator (CEM W-102A-NN0-K, Bronkhorst). A Schematic representation of the HP-TGA setup is shown in figure 3.2. A detailed description can be found in [38]. For each test, 24 ±1 mg of C2F were loaded in an alumina sample holder connected to a CI Precision microbalance with a platinum wire. The sample temperature and weight, as well as the reactor pressure, were continuously monitored. Inlet and outlet lines were kept at 250 °C to avoid water condensation. Blank measurements were performed with the empty sample holder (no oxygen carrier loaded) for each condition to

correct the weight signal for buoyancy effects caused by changes in the feed composition and reactor temperature and pressure.

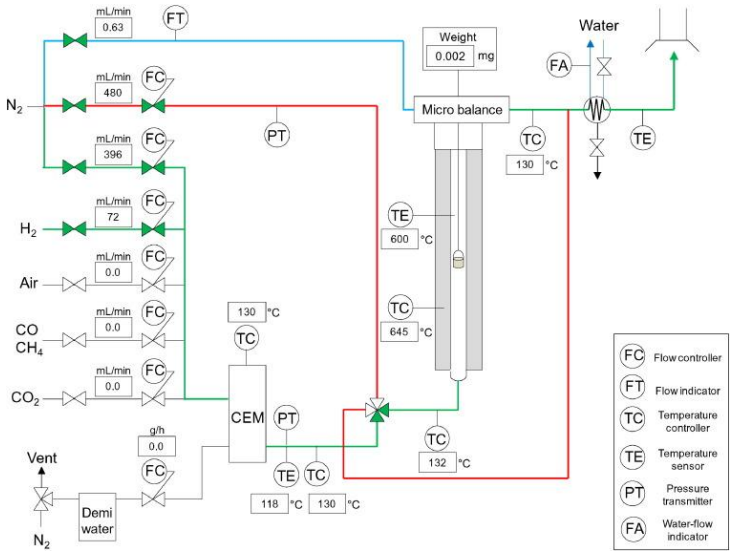

Fig. 3.2. Schematic representation of the HP-TGA setup (from [38]).

Stability tests

Reduction-oxidation experiments up to 50 cycles were performed at a fixed temperature of 800 °C and different pressures to assess the OC stability in different operating conditions. Each cycle consisted in a 12 min reduction in 20% mol. H_2 and a complete reoxidation in 10% mol. H_2O. Oxidation time was varied to take in account mass transfer limitations at higher pressure. The total flowrate was kept at 2 Nl/min at ambient pressure and 4 Nl/min at 10 bar.

Reactivity tests

To perform the kinetic analysis, a dedicate set of experiments was performed for both reduction and oxidation modelling. A different sample was used for each temperature and pressure combination. All the experiments were preceded by three reduction-oxidation cycles (20% mol. H_2-air) at 900 °C to obtain a cyclic steady state. Due to setup limitations, it was not possible to perform high pressure experiments at the same spatial velocity as the ambient pressure case. Nevertheless, the total flowrate was chosen to be high enough to ensure independence of the reaction rates in respect of it (shown in fig. 3.3a for the 20 bar case). The total flowrate used in the reduction kinetic measurements was 2 Nl/min at ambient pressure, 4 Nl/min at 5 and 10 bar, and 6 Nl/min at 20 bar. For each step, reactants were fed until the sample weight reached a steady state. Isothermal reduction experiments were conducted varying temperature, reducing gas (H_2) volume fraction and total pressure, ranging between 750 and 900°C, 0.2 and 0.6, and 1 and 20 bar respectively. For reduction experiments, the oxygen carrier conversion (α) was calculated according to eq. (3.2).

$$\alpha = \frac{m_{ox} - m(t)}{m_{ox} - m_{red}} \qquad (3.2)$$

Oxidation experiments were conducted in the 1-20 bar and 750-900 °C pressure and temperature range. An additional set of experiments was conducted at ambient pressure reducing the sample at 750 °C and 20% H_2 and successively oxidizing it at 650, 675 or 700 °C. In all cases, the steam fraction in the feed was kept constant at 10%

mol. In N_2 to avoid steam condensation at high pressure. The total flowrate used in the measures was 2 Nl/min at ambient pressure, 4 Nl/min at 5 and 10 bar and 6 Nl/min at 20 bar to avoid external mass transfer limitations (figure 3.3b). The oxygen carrier conversion was calculated as shown in eq. (3.3).

$$\alpha_{ox} = \frac{m(t) - m_{red}}{m_{ox} - m_{red}} \tag{3.3}$$

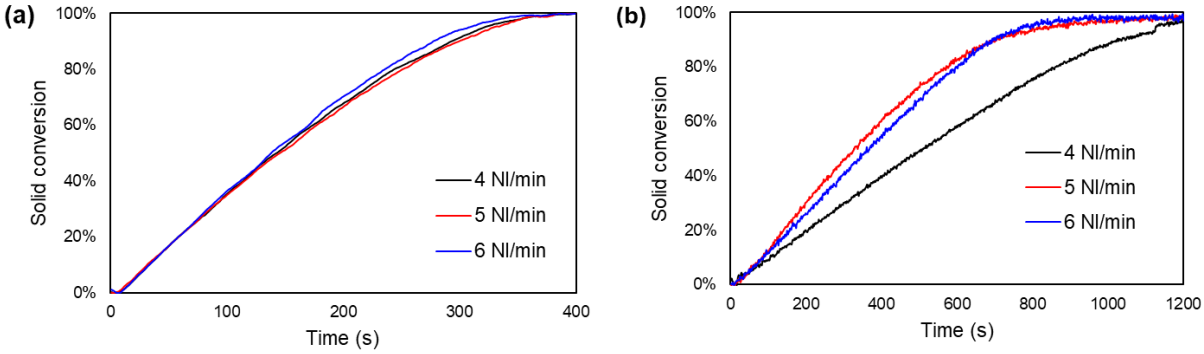

Fig. 3.3. (a) $Ca_2Fe_2O_5$ reduction at 900 °C, 20 bar and 20% vol. H_2 at various total flowrates. Oxidation was performed in air. (b) $Ca_2Fe_2O_5$ oxidation at 900 °C, 20 bar and 10% vol. H_2O at various total flowrates.

Kinetic analysis

The reduction reaction of $Ca_2Fe_2O_5$ with H_2 is described by eq. (3.4).

$$Ca_2Fe_2O_5 + 3H_2 \rightleftharpoons 2CaO + 2Fe + 3H_2O \tag{3.4}$$

Assuming an Arrhenius-type temperature dependency of the rate equation, the latter can be written as:

$$r\left(T, \alpha, p_{H_2}\right) = \frac{d\alpha}{dt} = Ae^{\left(-E_a/RT\right)} f(\alpha)\, p_{H_2}^n \tag{3.5}$$

In which r is the reaction rate, A is the apparent Arrhenius pre-exponential factor, E_a is the apparent activation energy, T is the absolute temperature, R is the universal gas constant, f(α) is the model function and n is the apparent reaction order [39]. To allow for a better description of the effect of total pressure on the reaction rate, an empirical correction factor (q) was introduced according to [40]:

$$r_{0,p} = r_0 \left(\frac{p}{p_0}\right)^q \tag{3.6}$$

Introducing the corrective factor, eq. (3.5) becomes:

$$r = Ae^{\left(-E_a/RT\right)} f(\alpha)\; p_{H_2}^n \left(\frac{p}{p_0}\right)^q \tag{3.7}$$

Eq. (3.7) was used to fit the isothermal reduction curves, simultaneously extracting the parameters A, E_a, n, and q. Isoconversional analysis was performed to check whether the process could be reasonably approximated with a one-step model. The isoconversional Friedman method was used to sequentially estimate the apparent activation energy over a small α interval (equal to 0.05) in the range α=0.1-0.9, as recommended in [41]. Briefly, the method is based on equation (3.8).

$$ln\left(\frac{d\alpha}{dx}\right)_{\alpha,i} = ln(f(\alpha)A_{\alpha}) - \frac{E_{a,\alpha}}{RT_{\alpha,i}} \quad (3.8)$$

In which the subscript α indicates the solid conversion (interval) upon which the analysis is performed, while the subscript i indicates the i-th test temperature. The value of apparent activation energy is obtained by linear fitting of $ln\left(\frac{d\alpha}{dx}\right)_{\alpha,i}$ *vs.* $\frac{1}{T_{\alpha,i}}$ data. According to [42], a process could be adequately described with a single step model if the difference between the minimum and maximum value of E_a is less than 30% of the average value. The same method was applied to the whole α=0.1-0.9 range to provide the initial guess for E_a.

The selection of the appropriate model functions to be evaluated, *i.e.* f(α), was carried out through visual inspection of normalized plots (so-called masterplots) of the normalized reaction rate *vs.* solid conversion [41] and morphological observations made over the reacted samples.

3.3. Results and discussion

3.3.1. Structural evolution of the OC

To better elucidate the structural changes that take place upon redox cycling, the OC material was characterized through XRD and SEM-EDS at various stages of a reduction-oxidation cycle performed at ambient pressure and 800 °C, as depicted in figure 3.4a. Each curve point was taken starting from as-synthesized C2F powders. From XRD patterns (figure 3.4b) it is observed that upon exposure to H_2 $Ca_2Fe_2O_5$ is reduced to CaO and metallic Fe. Upon oxidation, $Ca_2Fe_2O_5$ crystalline structure is fully restored. From XRD, no evidence of the formation of solid phases different from $Ca_2Fe_2O_5$, CaO and Fe is provided. Both reduction and oxidation reactions are known to proceed without stable intermediates [20, 43, 44]. SEM micrographs show the progressive formation of spherical particles on the surface of the grains, and the simultaneous formation of pores and cracks on the grains surface. At high reduction degrees (points R3 and R4 in figure 3.4), the surface of the grains appears composed by a large number of particles embedded in a rough matrix. Upon oxidation, the particles are no longer visible, while pores formed during the reduction are retained. EDS maps of the same samples has been acquired to confirm the nature of the observed particles (figure 3.5). Figure 3.5b shows that upon reduction some inhomogeneities in the Fe distribution arise, corresponding to the bright spots observed from SEM. As shown in figure 3.5c, on the fully reduced sample metallic iron is distributed in sphere-like domains with diameter in the range of 100-400 nm.

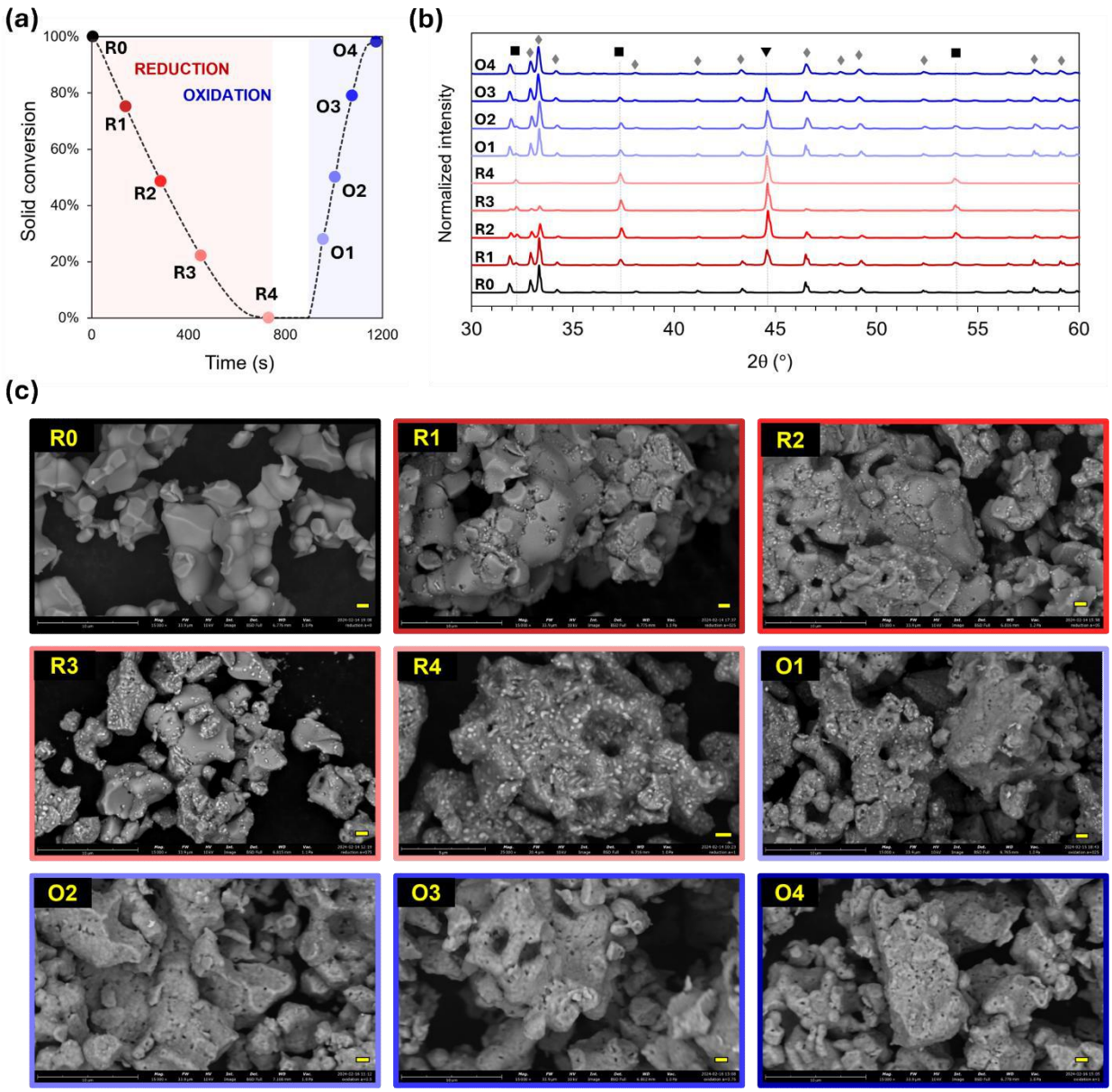

Fig. 3.4. (a) Point position on TG curve. The solid conversion was calculated according to eq. (3.2). (b) XRD profiles of the OC at different reaction stages. The marked peaks were attributed to: Fe (▼) [45], CaO (■) [46] and $Ca_2Fe_2O_5$ (♦) [15]. (c) SEM micrographs. Yellow bars represent 1 μm scale.

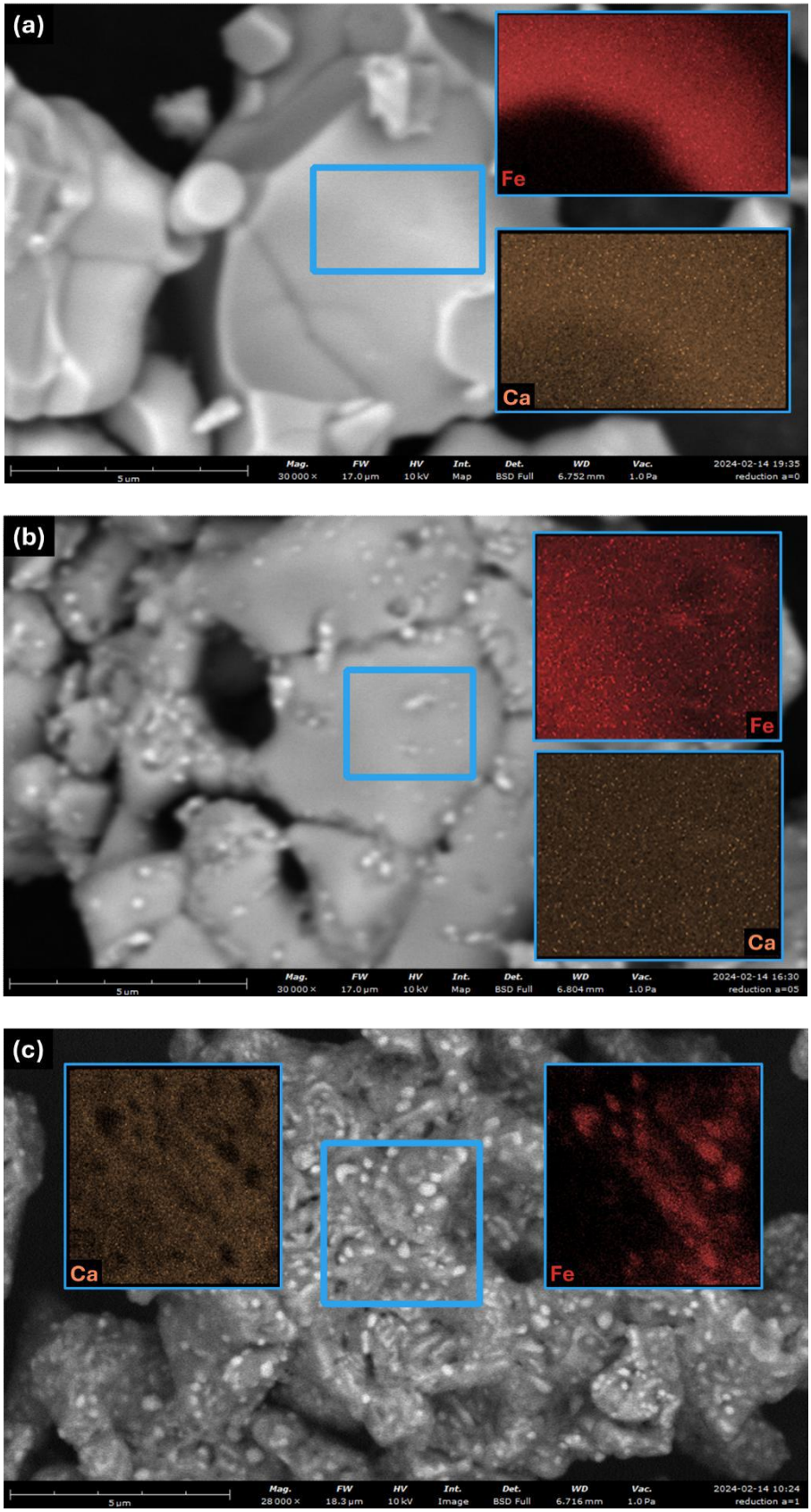

Fig. 3.5. SEM-EDS maps of $Ca_2Fe_2O_5$ samples upon reduction at (a) 0%, (b) 50%, (c) 100% conversion (800 °C, 1 bar, 20% H_2).

3.3.2. OC stability

The evaluation of the cyclic stability of C2F was investigated performing 50 cycles at a fixed temperature of 800 °C and two different pressures, 1 and 10 bar. Figure 3.6 reports the samples weight variation during the reduction step in selected cycles. At 1 bar, the sample reduced faster in the second cycle in respect of the first one, while all the following cycles showed almost superimposable weight loss profiles. The increase in the reduction speed between the first and second cycle could be due to the porous structure formed upon the first redox cycle, as discussed in the previous section. At 10 bar, this phenomenon is no longer visible, and the sample shows a highly stable behaviour over all the 50 cycles performed.

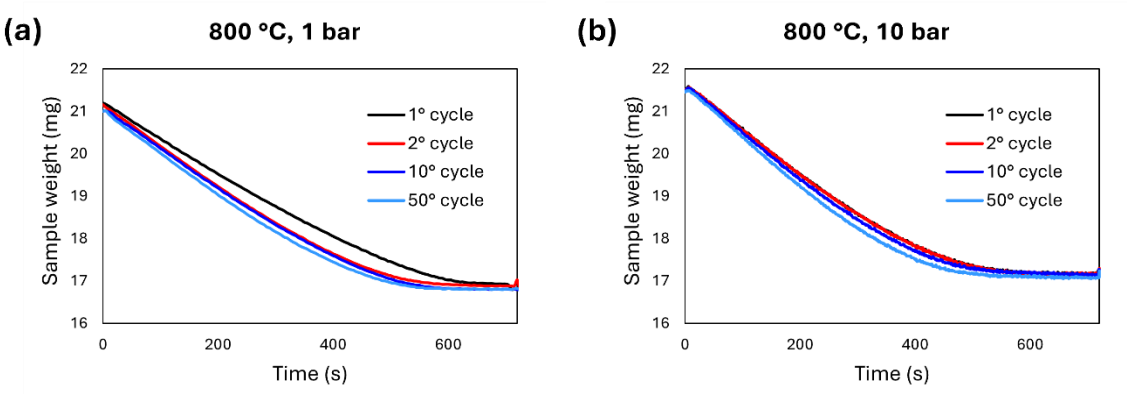

Fig. 3.6. Cyclic performance of C2F upon 50 H_2-H_2O reduction-oxidation cycles at 800 °C.

X-ray diffraction patterns of the samples after the test (figure 3.7) do not show major modifications in the crystalline structure of the samples. The lower intensity of the diffraction peaks observed on the tested samples is due to the low amount of sample that it was possible to retrieve from the HP-TGA. Small amounts of segregated impurity phases (CaO and Fe_3O_4) are observed in both the tested samples. As discussed in the previous section, exposing C2F to repeated reduction-oxidation cycles lead to the development of a porous network inside the original grain matrix. Evidence of this phenomenon can be seen also on the samples cycled 50 times (figure 3.8). The tested material (figure 3.7b, c) displays a more porous and complex morphology compared to the pristine C2F. Notably, the sample tested at 10 bar exhibits slightly coarser features than the one tested at 1 bar.

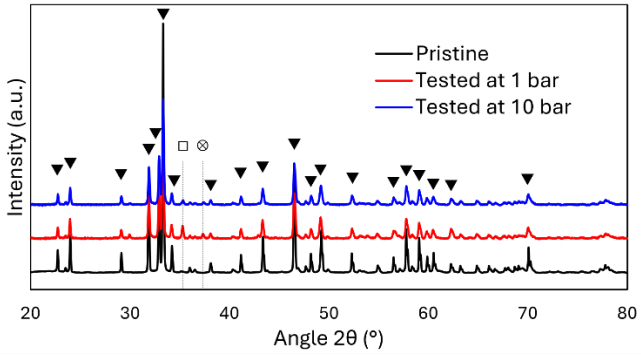

Fig. 3.7. Diffraction patters of pristine C2F and C2F tested for 50 redox cycles at 1 and 10 bar. (▼) C2F. (⊗) CaO, PDF card 01-075-0264. (□) Fe_3O_4, PDF card 00-019-0629.

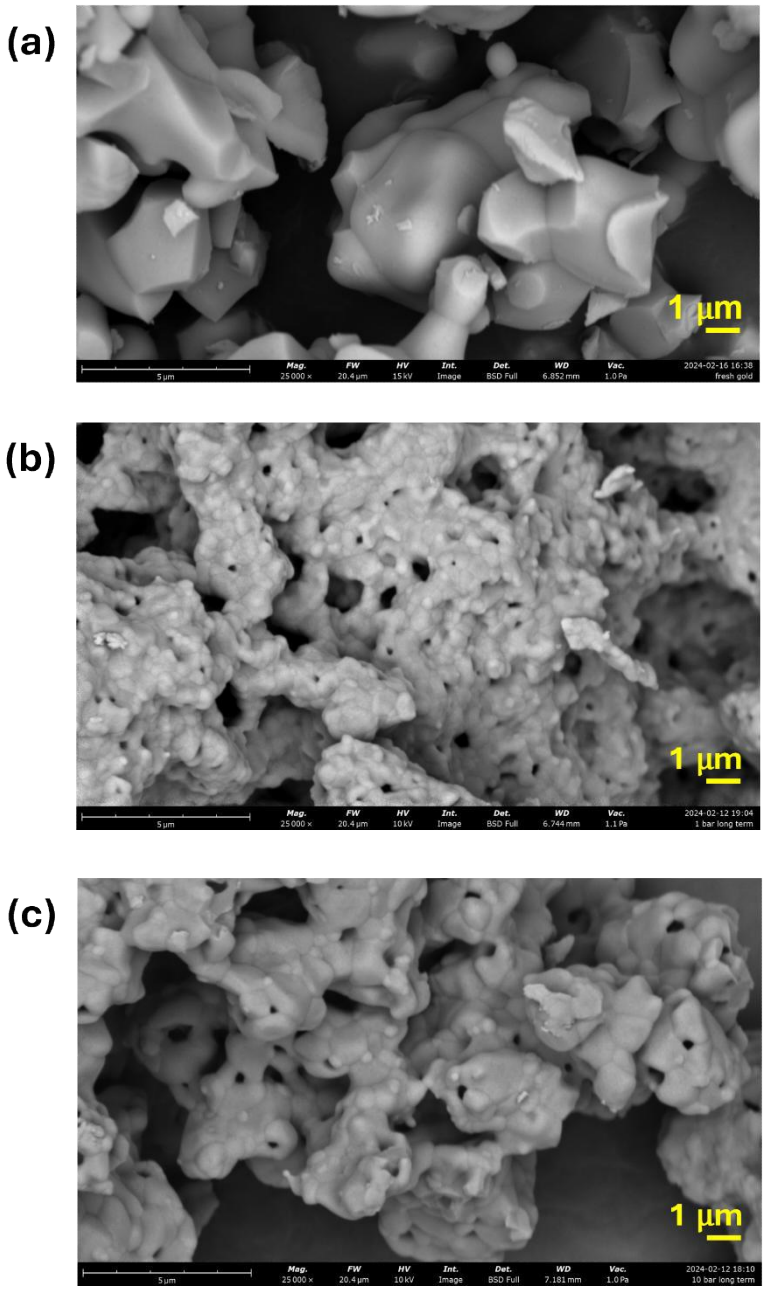

Fig. 3.8. SEM images of (a) pristine C2F, (b) C2F tested for 50 redox cycles at 1 bar and (c) C2F tested for 50 redox cycles at 10 bar.

3.3.3. Kinetic modelling of the reduction step

The kinetic parameters for the reduction have been determined performing experiments at various pressures, temperatures and H_2 volume fractions, respectively in the range 1-20 bar, 750-900 °C and 20-60 %. As an example, figure 3.9 shows conversion versus time curves obtained by fixing respectively (a) total pressure and H_2 volume fraction, (b) total pressure and temperature and (c) temperature and H_2 volume fraction.

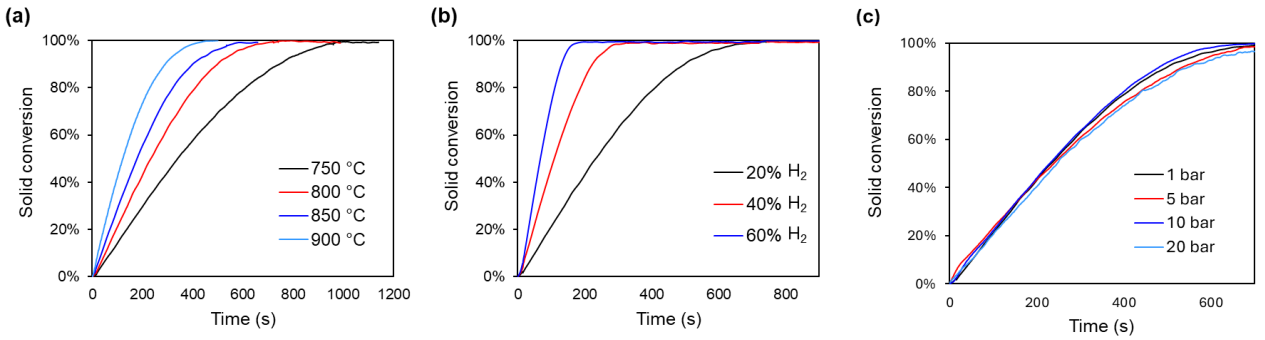

Fig. 3.9. $Ca_2Fe_2O_5$ reduction *vs.* time curves at (a) 1 bar, 20% vol. H_2, (b) 1 bar, 800 °C and (c) 800 °C, 20% vol. H_2.

A model fitting approach was adopted to describe the reduction kinetics. A single experiment was carried on for each temperature and pressure combination, while H_2 volume fraction was varied within the same test. As recommended in [41], the suitability of a single-step model for the description of the reduction process was investigated evaluating the apparent activation energy at different conversions varying from 0.1 to 0.9 through Friedman's isoconversional method applied to small conversion intervals (corresponding to a conversion range of 0.05). Significant variations of the E_a value (conventionally when the difference between the maximum and minimum values of E_a is more than 20–30% of the average) with conversion are considered indicative of a multi-step process. As shown in figure 3.10, the low variability of the E_a value over the conversion range supports the choice of a single-step model. At 20 bar, the activation energy calculated by the Friedman's method was found to differ significantly from the lower pressure cases, and those data were fitted separately keeping the apparent reaction order and the pressure correction term constant. In heterogeneous solid-gas reactions, a decrease in the apparent activation energy is typically correlated to the concomitant effect of mass (and heat) transfer phenomena, together with the intrinsic reaction rate, to the determination of the overall reaction kinetics. In fact, because of the inverse dependency of the gas diffusion coefficient with pressure [47], at elevated pressures the gas diffusion coefficient decreases, slowing reactant/product transport to/from the solid surface. This shifts the rate-determining step from the temperature-sensitive chemical reaction to diffusion-controlled processes, which exhibit weaker temperature dependence (lower apparent Ea). Consequently, under high-pressure conditions, the overall kinetics reflect the transport limitations rather than the inherent reaction barrier, as supported by literature [47-49].

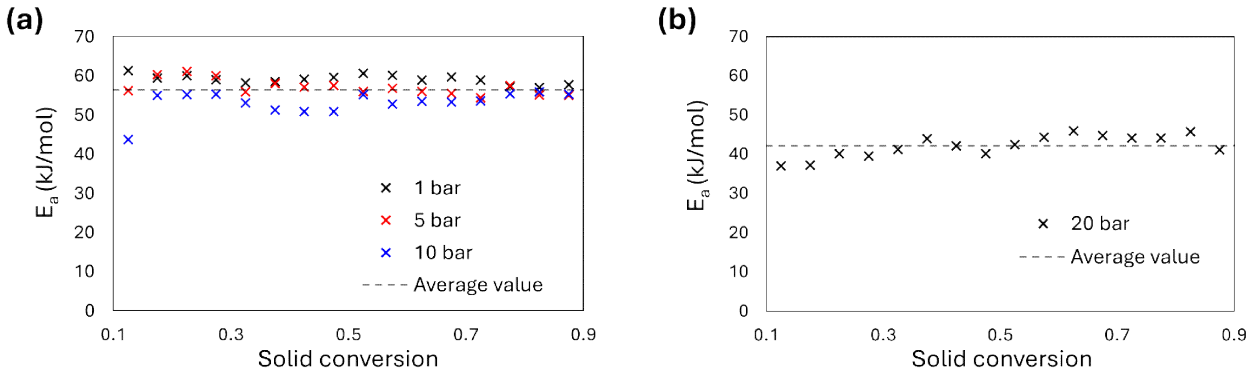

Fig. 3.10. Fitted Ea value *vs.* solid conversion over small conversion intervals for H_2 reduction at (a) 1,5,10 and (b) 20 bar (T between 750 and 900°C).

The choice of the single-step model was made based on graphical procedures and on phenomenological considerations on the microstructural evolution of the OC upon reaction, as discussed in the previous section. Reaction rate *vs.* solid conversion masterplots are shown in figure 3.11. A Johnson-Mehl-Avrami-Erofeev-Kolmogorov (JMAEK) model [50] with an Avrami exponent (n_{Av}) of 1.5 was used to fit the experimental data. The mathematical form of the model is shown in eq. (3.10).

$$f(\alpha) = 1.5 \cdot (1-\alpha) \cdot (-\ln(1-\alpha))^{1/2} \qquad (3.10)$$

The model assumes that the formation and subsequent growth of crystalline product nuclei is the kinetically controlling step, that the nuclei are randomly distributed across the reactant volume and that the rates of nucleation and growth are constant in the whole solid conversion range. The Avrami exponent arises from the combination of the rates expression for nucleation and growth. Its value cannot be attributed unequivocally to a distinct kinetically controlling step, since it accounts for both phenomena [51]. Fitted values for n_{Av} evaluated in the 0.1-0.9 α range with 0.1 increments are reported in figure 3.12.

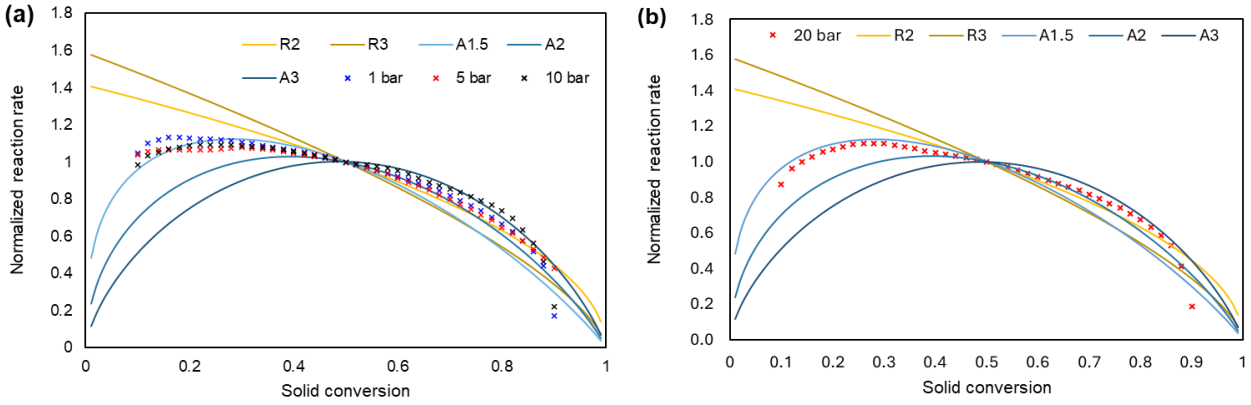

Fig. 3.11. Normalized reaction rate $\left(d\alpha/dt\right)/\left(d\alpha/dt\right)|_{0.5}$ *vs.* solid conversion experimental and selected theoretical masterplots at (a) 1,5,10 and (b) 20 bar.

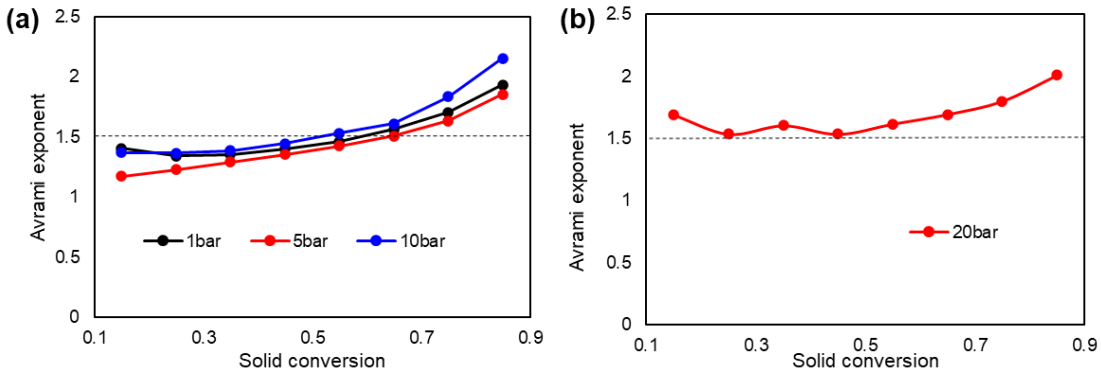

Fig. 3.12. Avrami exponent value evaluated by linear fitting of $\ln(-\ln(1-\alpha))$ against $\ln(t)$ curves over small conversion intervals at (a) 1,5,10 and (b) 20 bar.

The microstructural analysis made on the reduction process provided evidence of the formation of quasi-spherically shaped product (metallic Fe) particles, suggesting an isotropic growth process, as already observed in [21]. For this reason, the n_{Av} value found in the present study was attributed to fast formation of nuclei and diffusion-controlled three-dimensional growth. A non-linear fitting method was applied to the entire dataset to

obtain numerical values of the apparent pre-exponential factor, the apparent activation energy, the apparent reaction order, and the pressure correction term exponent (as shown in eq. (3.7)). Figure 3.13 reports the model predictions against the experimental data for the reduction with 20% H_2 at various temperatures and pressures. The fitted values are reported in tab. 3.1. The closeness of the value of n and -q reflects the low dependence of the reaction rate from the total pressure, as eq. (3.7) can be rewritten as:

$$r = Ae^{\left(-E_a/RT\right)} f(\alpha)\ x_{H_2}^{n} \left(\frac{p^{(n-q)}}{{p_0}^{q}}\right) \qquad (3.11)$$

Reaction rate is thus largely determined by the reactant molar fraction in the feed, while the total pressure has a limited effect, as already observed on different OC materials by other authors [32, 40]. The accuracy of the fitting was checked by evaluating the apparent activation energy by Friedman's isoconversional method over the 0.1-0.9 solid conversion range at each pressure level [52]. The obtained values, reported in tab. 3.2, are consistent with those calculated by the model fitting approach. Similar values were obtained by other authors for C2F reduction with hydrogen at ambient pressure [21].

Tab. 3.1. Fitted kinetic parameters for $Ca_2Fe_2O_5$ reduction with H_2.

	E_a (kJ · mol^{-1})	A (s^{-1} · Pa^{-n})	n	q	R^2 fitting
1-10 bar	54.93	$2.12 \cdot 10^{-5}$	1.13	-1.16	0.9735
20 bar	42.36	$6.69 \cdot 10^{-6}$	1.13	-1.16	0.9806

Tab. 3.2 Apparent activation energy for $Ca_2Fe_2O_5$ reduction with H_2 calculated by Friedman method at various total pressures.

	1 bar	5 bar	10 bar	20 bar
E_a (kJ · mol^{-1}) calculated by Friedman's method	54.80	54.30	53.09	42.41

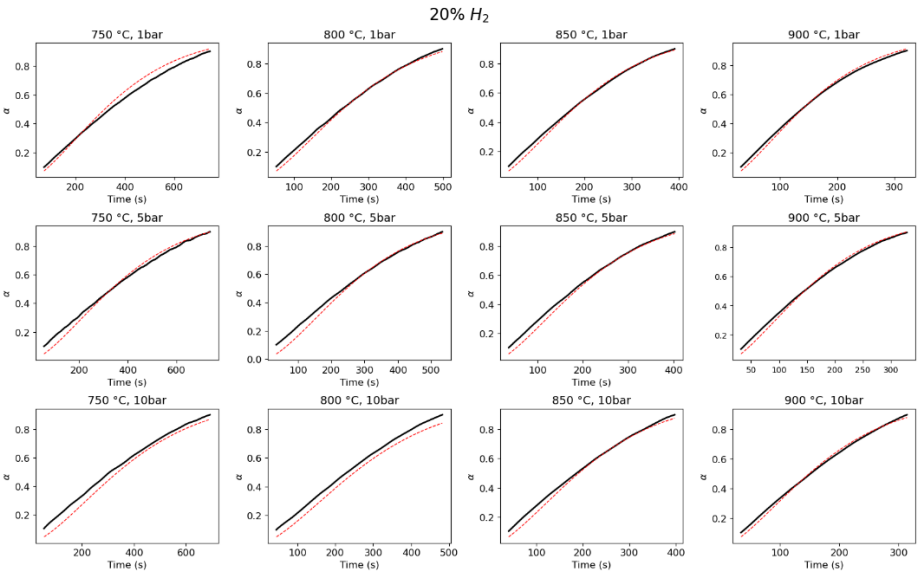

Fig. 3.13. Model predictions (dashed red) *vs.* experimental conversion data (solid black) of $Ca_2Fe_2O_5$, reduction with 20% H_2 at various temperatures and pressures.

3.3.4. Oxidation with steam

In the temperature range investigated for the evaluation of the reduction kinetics, the chemical reaction between steam and metallic iron supported by CaO to give $Ca_2Fe_2O_5$ is believed to be significantly faster than the inverse process. In fact, no temperature dependency was observed at temperatures above 750 °C, indicating that the rate-determining step was not the chemical reaction. Above 750 °C, almost superimposable solid conversion *versus* time curves were obtained for each pressure level, as shown in figure 3.14. Similar results were obtained varying total flowrates (up to 6 Nl/min), sample mass (24 and 40 mg) and particle size (unpelletized and 200-400 µm pelletized sample). Moreover, reaction rate was found to be comparable between 1 and 5 bar, and to decrease with increasing pressure at pressures higher than 5 bar. It is hypothesized that this observation results from the combination of Knudsen diffusion (independent on pressure, diffusion rate-controlling at low total pressures) and bulk diffusion (inversely proportional to the pressure, diffusion rate-controlling at high total pressures) inside the OC particles. At ambient pressure, a decrease in the oxidation rate with decreasing temperature was observed below 700 °C. Nevertheless, the decrease in the oxidation rate was accompanied by the incomplete formation of $Ca_2Fe_2O_5$ and the appearance of significant amounts of segregated phases such as Fe_3O_4, CaO and $CaFe_2O_4$ (figure 3.15), likely due to the effect of temperature on the diffusion rate of metallic cations [17]. Because of the uncertainties regarding the kinetics of formation of the different crystalline phases observed, which in turn affects their relative amount in the fully oxidised sample, the oxidation reaction kinetics were not modelled in the present work.

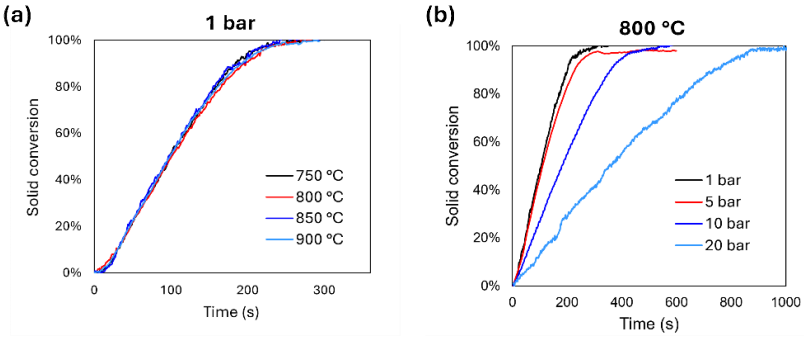

Fig.3.14. $Ca_2Fe_2O_5$ oxidation *vs.* time curves at (a) 1 bar and 10% vol. H_2O and (b) 800 °C and 10% H_2O.

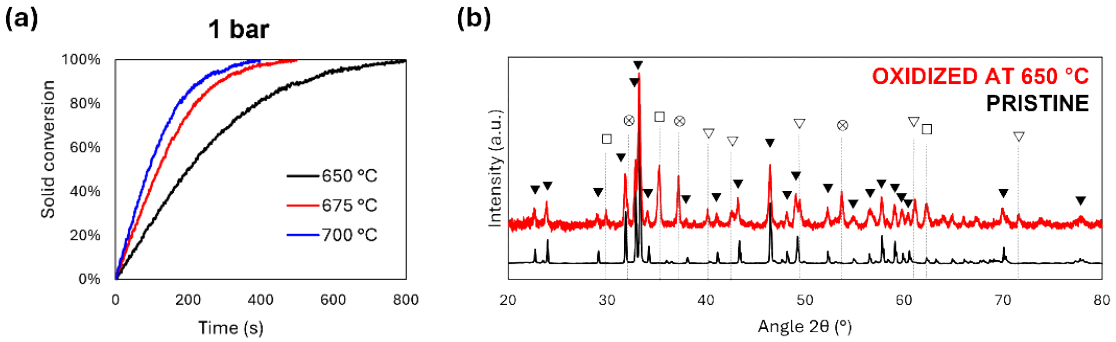

Fig. 3.15. (a) $Ca_2Fe_2O_5$ oxidation *vs.* time curves at 1 bar and 10% vol. H_2O. (b) X-ray diffraction patterns of pristine C2F (black) and C2F after reduction (750 °C, 1 bar, 20% H_2) and oxidation at 650 °C (1 bar, 10% H_2O). (▼) C2F. (⊗) CaO, PDF card 01-075-0264. (□) Fe_3O_4, PDF card 00-019-0629. (▽) $CaFe_2O_4$, PDF card 01-072-1199.

3.4. Conclusions

$Ca_2Fe_2O_5$ (C2F) has shown an exceptional stability when subjected to reduction-oxidation cycles, both at ambient pressure and in pressurized conditions. The ability of an oxygen carrier material to withstand extensive redox cycling at high pressure without performance deterioration is particularly relevant for the large-scale implementation of CL processes, which benefit significantly from high-pressure operation. The reduction of C2F to CaO and metallic Fe takes place along with the formation of sphere-like Fe particles 100-400 nm in diameter, dispersed on a CaO matrix. Upon reoxidation, the Fe domains are gradually reincorporated into the matrix, leading to the development of a porous structure. The parametric study of the reduction step revealed that total pressure has a minimal impact on reduction kinetics, whereas temperature and the reactant mole fraction in the gas feed play a dominant role in influencing the reaction rate. A comprehensive kinetic model was developed taking in account both the structural evolution of the C2F upon reduction and oxidation and the results obtained from the parametric study. A good fit was obtained using a nucleation and growth model (JMAEK) with an Avrami exponent of 1.5. Between 1 and 10 bar, a constant apparent activation energy of 54.93 kJ/mol was obtained from the numerical fitting, while at 20 bar a lower value was found, corresponding to 42.36 kJ/mol. The lower E_a found at 20 bar was attributed to increased diffusion limitations caused by the higher pressure, which slows down gas-phase diffusion.

3.5. References

[1] Zheng, H., Jiang, X., Gao, Y., Tong, A., & Zeng, L. (2022d). Chemical looping reforming: process fundamentals and oxygen carriers. Discover Chemical Engineering, 2(1). https://doi.org/10.1007/s43938-022-00012-3

[2] Zhu, X., Imtiaz, Q., Donat, F., Müller, C. R., & Li, F. (2020). Chemical looping beyond combustion – a perspective. *Energy & Environmental Science*, *13*(3), 772–804. https://doi.org/10.1039/c9ee03793d

[3] Spallina, V., Motamedi, G., Gallucci, F., & Van Sint Annaland, M. (2019). Techno-economic assessment of an integrated high-pressure chemical-looping process with packed-bed reactors in large scale hydrogen and methanol production. *International Journal of Greenhouse Gas Control*, *88*, 71–84. https://doi.org/10.1016/j.ijggc.2019.05.026

[4] Ediger, V. Ş., & Berk, I. (2023). Future availability of natural gas: Can it support sustainable energy transition? *Resources Policy*, *85*, 103824. https://doi.org/10.1016/j.resourpol.2023.103824

[5] Ishida, M., Jin, H., & Okamoto, T. (1996). A fundamental study of a new kind of medium material for Chemical-Looping combustion. *Energy & Fuels*, *10*(4), 958–963. https://doi.org/10.1021/ef950173n

[6] Svoboda, K., Slowinski, G., Rogut, J., & Baxter, D. (2007). Thermodynamic possibilities and constraints for pure hydrogen production by iron based chemical looping process at lower temperatures. *Energy Conversion and Management*, *48*(12), 3063–3073. https://doi.org/10.1016/j.enconman.2007.05.019

[7] Jerndal, E., Mattisson, T., & Lyngfelt, A. (2006). Thermal Analysis of Chemical-Looping combustion. *Process Safety and Environmental Protection*, *84*(9), 795–806. https://doi.org/10.1205/cherd05020

[8] Tang, M., Xu, L., & Fan, M. (2015). Progress in oxygen carrier development of methane-based chemical-looping reforming: A review. *Applied Energy*, *151*, 143–156. https://doi.org/10.1016/j.apenergy.2015.04.017

[9] Galinsky, N. L., Shafiefarhood, A., Chen, Y., Neal, L., & Li, F. (2014). Effect of support on redox stability of iron oxide for chemical looping conversion of methane. *Applied Catalysis B Environment and Energy*, *164*, 371–379. https://doi.org/10.1016/j.apcatb.2014.09.023

[10] Zhao, L., Dou, B., Zhang, H., & Wang, Z. (2021). Oxygen carriers for chemical-looping water splitting to hydrogen production: A critical review. *Carbon Capture Science & Technology*, *1*, 100006. https://doi.org/10.1016/j.ccst.2021.100006

[11] Dueso, C., Thompson, C., & Metcalfe, I. (2015). High-stability, high-capacity oxygen carriers: Iron oxide-perovskite composite materials for hydrogen production by chemical looping. *Applied Energy*, *157*, 382–390. https://doi.org/10.1016/j.apenergy.2015.05.062

[12] Das, S., Biswas, A., Tiwary, C., & Paliwal, M. (2022). Hydrogen production using chemical looping technology: A review with emphasis on H_2 yield of various oxygen carriers. *International Journal of Hydrogen Energy*, *47*(66), 28322–28352. https://doi.org/10.1016/j.ijhydene.2022.06.170

[13] Murugan, A., Thursfield, A., & Metcalfe, I. S. (2011). A chemical looping process for hydrogen production using iron-containing perovskites. *Energy & Environmental Science*, *4*(11), 4639. https://doi.org/10.1039/c1ee02142g

[14] Ismail, M., Liu, W., & Scott, S. A. (2014). The performance of Fe_2O_3-CaO Oxygen Carriers and the Interaction of Iron Oxides with CaO during Chemical Looping Combustion and H2 production. *Energy Procedia*, *63*, 87–97. https://doi.org/10.1016/j.egypro.2014.11.010

[15] Ismail, M., Liu, W., Dunstan, M. T., & Scott, S. A. (2016). Development and performance of iron-based oxygen carriers containing calcium ferrites for chemical looping combustion and production of hydrogen. *International Journal of Hydrogen Energy*, *41*(7), 4073–4084. https://doi.org/10.1016/j.ijhydene.2015.11.066

[16] Chan, M. S., Liu, W., Ismail, M., Yang, Y., Scott, S. A., & Dennis, J. S. (2016). Improving hydrogen yields, and hydrogen:steam ratio in the chemical looping production of hydrogen using $Ca_2Fe_2O_5$. *Chemical Engineering Journal*, *296*, 406–411. https://doi.org/10.1016/j.cej.2016.03.132

[17] Ismail, M., Liu, W., Chan, M. S. C., Dunstan, M. T., & Scott, S. A. (2016b). Synthesis, application, and carbonation behavior of $Ca_2Fe_2O_5$ for chemical looping H_2 production. *Energy & Fuels*, *30*(8), 6220–6232. https://doi.org/10.1021/acs.energyfuels.6b00631

[18] Shaula, A., Pivak, Y., Waerenborgh, J., Gaczyñski, P., Yaremchenko, A., & Kharton, V. (2006). Ionic conductivity of brownmillerite-type calcium ferrite under oxidizing conditions. *Solid State Ionics*, *177*(33–34), 2923–2930. https://doi.org/10.1016/j.ssi.2006.08.030

[19] Shukla, A., Gaur, N., & Ghosh, P. (2020). First principles investigations of structure, stability and electronic properties of polar $Ca_2Fe_2O_5$ (010) surfaces. *Applied Surface Science*, *527*, 146703. https://doi.org/10.1016/j.apsusc.2020.146703

[20] Miller, D. D., Riley, J., & Siriwardane, R. (2019). Interaction of Methane with Calcium Ferrite in the Chemical Looping Partial Oxidation Application: Experimental and DFT Study. *Energy & Fuels*, *34*(2), 2193–2204. https://doi.org/10.1021/acs.energyfuels.9b03623

[21] Cai, Y., Wang, C., Zhong, M., Zhang, Z., Xiao, B., Xu, T., & Wang, X. (2023). Evaluation of redox activity of brownmillerite-structured Ca2Fe2O5 oxygen carrier for chemical looping applications. *International Journal of Hydrogen Energy*, *48*(70), 27112–27126. https://doi.org/10.1016/j.ijhydene.2023.03.395

[22] Ramezani, R., Di Felice, L., & Gallucci, F. (2023). A review of chemical looping reforming technologies for hydrogen production: recent advances and future challenges. *Journal of Physics Energy*, *5*(2), 024010. https://doi.org/10.1088/2515-7655/acc4e8

[23] Kim, Y., Lim, H. S., Kim, H. S., Lee, M., Lee, J. W., & Kang, D. (2022). Carbon dioxide splitting and hydrogen production using a chemical looping concept: A review. *Journal of CO2 Utilization*, *63*, 102139. https://doi.org/10.1016/j.jcou.2022.102139

[24] Sandvik, P., Kathe, M., Wang, W., Kong, F., & Fan, L. (2018). High-Pressure Chemical Looping Reforming Processes: System Analysis for Syngas Generation from Natural Gas and Reducing Tail Gases. *Energy & Fuels*, *32*(10), 10408–10420. https://doi.org/10.1021/acs.energyfuels.8b01834

[25] Spallina, V., Marinello, B., Gallucci, F., Romano, M., & Van Sint Annaland, M. (2016b). Chemical looping reforming in packed-bed reactors: Modelling, experimental validation and large-scale reactor design. *Fuel Processing Technology*, *156*, 156–170. https://doi.org/10.1016/j.fuproc.2016.10.014

[26] Adanez, J., Abad, A., Garcia-Labiano, F., Gayan, P., & De Diego, L. F. (2011). Progress in Chemical-Looping Combustion and Reforming technologies. *Progress in Energy and Combustion Science*, *38*(2), 215–282. https://doi.org/10.1016/j.pecs.2011.09.001

[27] Ugwu, A., Donat, F., Zaabout, A., Müller, C., Albertsen, K., Cloete, S., Van Diest, G., & Amini, S. (2020). Hydrogen production by water splitting using gas switching technology. *Powder Technology*, *370*, 48–63. https://doi.org/10.1016/j.powtec.2020.05.039

[28] Nestl, S., Voitic, G., Lammer, M., Marius, B., Wagner, J., & Hacker, V. (2015). The production of pure pressurised hydrogen by the reformer-steam iron process in a fixed bed reactor system. *Journal of Power Sources*, *280*, 57–65. https://doi.org/10.1016/j.jpowsour.2015.01.052

[29] Voitic, G., Nestl, S., Malli, K., Wagner, J., Bitschnau, B., Mautner, F., & Hacker, V. (2016). High purity pressurised hydrogen production from syngas by the steam-iron process. *RSC Advances*, *6*(58), 53533–53541. https://doi.org/10.1039/c6ra06134f

[30] Zacharias, R., Visentin, S., Bock, S., & Hacker, V. (2019). High-pressure hydrogen production with inherent sequestration of a pure carbon dioxide stream via fixed bed chemical looping. *International Journal of Hydrogen Energy*, *44*(16), 7943–7957. https://doi.org/10.1016/j.ijhydene.2019.01.257

[31] Osman, M., Khan, M. N., Zaabout, A., Cloete, S., & Amini, S. (2021). Review of pressurized chemical looping processes for power generation and chemical production with integrated CO_2 capture. *Fuel Processing Technology*, *214*, 106684. https://doi.org/10.1016/j.fuproc.2020.106684

[32] Hamers, H. P., Gallucci, F., Williams, G., Cobden, P. D., & Van Sint Annaland, M. (2015). Reactivity of Oxygen Carriers for Chemical-Looping Combustion in Packed Bed Reactors under Pressurized Conditions. *Energy & Fuels*, *29*(4), 2656–2663. https://doi.org/10.1021/ef5027899

[33] Nordness, O., Han, L., Zhou, Z., & Bollas, G. M. (2015). High-Pressure Chemical-Looping of Methane and Synthesis Gas with Ni and Cu Oxygen Carriers. *Energy & Fuels*, *30*(1), 504–514. https://doi.org/10.1021/acs.energyfuels.5b01986

[34] Deshpande, N., Majumder, A., Qin, L., & Fan, L. (2015). High-Pressure Redox Behavior of Iron-Oxide-Based Oxygen Carriers for Syngas Generation from Methane. *Energy & Fuels*, *29*(3), 1469–1478. https://doi.org/10.1021/ef5025998

[35] Voitic, G., Nestl, S., Lammer, M., Wagner, J., & Hacker, V. (2015). Pressurized hydrogen production by fixed-bed chemical looping. *Applied Energy*, *157*, 399–407. https://doi.org/10.1016/j.apenergy.2015.03.095

[36] Hu, J., Galvita, V. V., Poelman, H., Detavernier, C., & Marin, G. B. (2019b). Pressure-induced deactivation of core-shell nanomaterials for catalyst-assisted chemical looping. *Applied Catalysis B Environment and Energy*, *247*, 86–99. https://doi.org/10.1016/j.apcatb.2019.01.084

[37] Zhao, Z., Uddi, M., Tsvetkov, N., Yildiz, B., & Ghoniem, A. F. (2016). Redox Kinetics Study of Fuel Reduced Ceria for Chemical-Looping Water Splitting. *The Journal of Physical Chemistry C*, *120*(30), 16271–16289. https://doi.org/10.1021/acs.jpcc.6b01847

[38] Pio, M. S., Roghair, I., Gallucci, F., & Van Sint Annaland, M. (2016). Investigation on the decrease in the reduction rate of oxygen carriers for chemical looping combustion. *Powder Technology*, *301*, 429–439. https://doi.org/10.1016/j.powtec.2016.06.031

[39] Pijolat, M., & Favergeon, L. (2018b). Kinetics and mechanisms of Solid-Gas reactions. In *Handbook of thermal analysis and calorimetry* (pp. 173–212). https://doi.org/10.1016/b978-0-444-64062-8.00011-5

[40] García-Labiano, F., Adánez, J., De Diego, L. F., Gayán, P., & Abad, A. (2005). Effect of pressure on the behavior of copper-, iron-, and Nickel-Based oxygen carriers for Chemical-Looping combustion. *Energy & Fuels*, *20*(1), 26–33. https://doi.org/10.1021/ef050238e

[41] Vyazovkin, S., Burnham, A. K., Criado, J. M., Pérez-Maqueda, L. A., Popescu, C., & Sbirrazzuoli, N. (2011). ICTAC Kinetics Committee recommendations for performing kinetic computations on thermal analysis data. *Thermochimica Acta*, *520*(1–2), 1–19. https://doi.org/10.1016/j.tca.2011.03.034

[42] Vyazovkin, S., Burnham, A. K., Favergeon, L., Koga, N., Moukhina, E., Pérez-Maqueda, L. A., & Sbirrazzuoli, N. (2020). ICTAC Kinetics Committee recommendations for analysis of multi-step kinetics. *Thermochimica Acta*, *689*, 178597. https://doi.org/10.1016/j.tca.2020.178597

[43] Sun, Z., Chen, S., Hu, J., Chen, A., Rony, A. H., Russell, C. K., Xiang, W., Fan, M., Dyar, M. D., & Dklute, E. C. (2017). $Ca_2Fe_2O_5$: A promising oxygen carrier for CO/CH_4 conversion and almost-pure H_2 production with inherent CO_2 capture over a two-step chemical looping hydrogen generation process. *Applied Energy*, *211*, 431–442. https://doi.org/10.1016/j.apenergy.2017.11.005

[44] Feng, Y., Wang, N., & Guo, X. (2021). Reaction mechanism of methane conversion over $Ca_2Fe_2O_5$ oxygen carrier in chemical looping hydrogen production. *Fuel*, *290*, 120094. https://doi.org/10.1016/j.fuel.2020.120094

[45] Zieliński, J., Zglinicka, I., Znak, L., & Kaszkur, Z. (2010). Reduction of Fe_2O_3 with hydrogen. *Applied Catalysis a General*, *381*(1–2), 191–196. https://doi.org/10.1016/j.apcata.2010.04.003

[46] Molinder, R., Comyn, T. P., Hondow, N., Parker, J. E., & Dupont, V. (2012). In situ X-ray diffraction of CaO based CO_2 sorbents. *Energy & Environmental Science*, *5*(10), 8958. https://doi.org/10.1039/c2ee21779a

[47] Atsumi, R., Noda, R., Takagi, H., Vecchione, L., Di Carlo, A., Del Prete, Z., & Kuramoto, K. (2014). Ammonia decomposition activity over Ni/SiO_2 catalysts with different pore diameters. *International Journal of Hydrogen Energy*, *39*(26), 13954–13961. https://doi.org/10.1016/j.ijhydene.2014.07.003

[48] Schneider, P.; Mitschka, P. (1969). Intraparticle Diffusion and the Apparent Activation Energy. *Chemical Engineering Science*, 24 (11), 1725–1731. https://doi.org/10.1016/0009-2509(69)87037-5

[49] Vyazovkin, S. (2000). On the phenomenon of variable activation energy for condensed phase reactions. *New Journal of Chemistry*, *24*(11), 913–917. https://doi.org/10.1039/b004279j

[50] Barmak, K. (2010). A commentary on: "Reaction Kinetics in Processes of Nucleation and Growth". *Metallurgical and Materials Transactions B*, *49*(6), 3616–3680. https://doi.org/10.1007/s11663-010-9421-1

[51] Galwey, A. K., Brown, M. E. Kinetic models for solid state reactions. *Thermal Decomposition of Ionic Solids*, Elsevier, 1999; pp. 75–115. https://doi.org/10.1016/s0167-6881(99)80004-4

[52] Dilmaç, N. (2021). Isothermal and non-isothermal reduction kinetics of iron ore oxygen carrier by CO: Modelistic and model-free approaches. *Fuel*, *296*, 120707. https://doi.org/10.1016/j.fuel.2021.120707

4. Chemical looping steam methane reforming using Ni-promoted composite $Ca_2Fe_2O_5$-$Ce_{0.8}Zr_{0.2}O_2$ oxygen carriers

Abstract

$Ca_2Fe_2O_5$ (C2F) shows several favourable properties and a remarkable redox stability when employed as Oxygen Carrier (OC) in Chemical Looping Steam Methane Reforming (CL-SMR) process. Nevertheless, it suffers from a very low reactivity towards CH_4. Here, composite C2F-$Ce_{0.8}Zr_{0.2}O_2$ (CZ) oxygen carriers were prepared by simple physical mixing and characterized. A comparative assessment of different functionalization strategies with Ni as reforming catalyst was performed by testing the samples for multiple CL-SMR cycles. The selective deposition of Ni onto the CZ gave by far the best results in terms of fuel conversion, syngas selectivity and H_2 yield during CL-SMR tests performed on composite samples, despite showing a significant activity loss following the first 10 redox cycles. N_2-physisorption, SEM-EDS and XPS suggest that the deactivation of the composite oxygen carrier is bound to the strong sintering of the CZ induced by the redox cycling and the co-presence of C2F in the same reactive bed.

4.1. Introduction

Fossil fuels are currently the dominant world's source of energy, with projections indicating that their share will remain above 60% in 2050 [1]. Considering the forecasted increase in the total energy demand, there is a growing need for efficient conversion technologies, particularly when it comes to non-renewable resources. Presently, natural gas reforming represents the major source of H_2 and syngas [2], which in turn are key intermediates in industrial chemical synthesis. Chemical Looping Steam Methane Reforming (CL-SMR) has been recently considered as an alternative to conventional Steam Methane Reforming (SMR) since it can provide a viable process intensification approach with inherent gas-gas separation [3]. Chemical Looping (CL) is a process strategy in which a given reaction is decomposed into multiple subreactions separated in time (in a dynamically operated reactor) or space (in multiple interconnected reactors). The subreactions are connected by a chemical intermediate, typically a solid, that cyclically alternates between the reacted and regenerated states. This concept can be applied to SMR by the use of a circulating metal oxide-based oxygen carrier, able to selectively oxidise CH_4 to CO and H_2 through the release of its lattice oxygen (reduction step), and to recover the original state by oxidation with steam, thus producing a stream of pure H_2 (oxidation step). The availability of suitable Oxygen Carriers is essential for the commercial-scale deployment of CL-SMR processes. The selection of the oxygen carrier influences fuel conversion and selectivity during the reduction step, as well as steam conversion in the oxidizer. Additionally, it determines the operative conditions and significantly impacts the overall economics of the process. The scientific community has dedicated large effort to the development of OCs able to fulfil the stringent requirements of the process, such as high Oxygen Transfer Capacity (OTC), good mechanical and chemical stability, good recyclability, low cost, and

low environmental footprint [4]. In this framework, Fe-based oxygen carriers are particularly attractive thanks to their environmental friendliness, low cost, large OTC and suitable thermodynamics [5]. The major issues related to the use of iron oxides as OC are their comparably low reactivity with CH_4 in respect of other transition metals oxides (e.g. Ni, Cu), their tendency to agglomerate at high reduction degrees and their non-optimal selectivity to partial oxidation products [6]. Multiple strategies have been proposed to address these challenges, such as the introduction of structural and chemical promoters and the confinement of Iron into complex oxides such as perovskites and garnets. $Ca_2Fe_2O_5$ (C2F) is a brownmillerite-type oxide that has recently been considered as OC for CL-SMR, thanks to its superior stability in redox cycles, its low equilibrium pO_2 and its fast oxygen ion transport [7, 8]. Despite the favourable features, it suffers from slow reduction kinetics, thus affecting negatively the CH_4 conversion. Studies reported that the introduction of a support material is beneficial to the reduction kinetics with CH_4 because it increases the dispersion of the active phase [9]. The introduction of transition metal dopants able to activate CH_4 (Ni, Cu) drastically increases the fuel conversion, even if it raises some concerns over the cyclical stability of the OC [10]. This finding suggests that the close contact between iron and the active metal phase could lead to undesired deactivation phenomena, such as the formation of alloys and the segregation of mixed oxide phases [11]. To overcome this, a spatial structuring approach of the redox material could be carried out [12, 13]. Providing a physical separation can avoid the formation of undesired phases [14], while keeping the beneficial effect of having a bifunctional material. Moreover, it has been proven that controlling the OCM lattice oxygen supply to the catalytically active phase through the interposition of an oxygen conducting material could enhance the product selectivity toward partial oxidation products [15]. As an example, it has been shown that the spatial proximity between Ni-based catalytic phase and Fe-based oxygen carrier phase in a ZrO_2-supported OCM has a significant impact on the CO selectivity during the reduction with CH_4, with the best results obtained by selectively deposit Ni particles on the zirconia support by sequential coprecipitation [12]. It has been observed that blending C2F with a Ce-based material leads to a composite OC with a higher reactivity in respect of the linear combination of the reactivities of the single components, indicating the existence of a certain degree of synergy between the two materials [16]. Furthermore, it was reported that a simple physical mixture of a Fe-based OC and a Ni-based catalyst can significantly enhance fuel conversion in chemical looping combustion and reforming applications [17, 18]. According to the authors, the promotion of the reactivity is likely due to a gas-phase collaborative mechanism between OC and catalyst, in which reducing gases (H_2, CO) produced on Ni accelerate the reduction of FeO_x, while the oxidizing gases produced by the reduction of FeO_x (H_2O, CO_2) inhibits Ni deactivation by solid carbon formation.

In this work, a physical mixture of $Ca_2Fe_2O_5$ and $Ce_{0.8}Zr_{0.2}O_2$ is investigated as OC in CL-SMR cycles and took as benchmark for the investigation of different methods to introduce catalytic amounts of Ni as a reactivity promoter. The prepared OC materials are compared in terms of reactant conversion, specific yields, and stability.

4.2. Experimental

The details on samples preparation and characterization methods are reported in chapter 2. Composite samples were prepared by mixing the desired amount of powdered components in an empty vial and shaking for 5 minutes. H_2-TPRs were performed in a Micromeritics Autochem II apparatus. Approximately 50 mg of powdered sample

were loaded I to a U-shaped reactor. Prior to the analysis, samples were held for 30 min at 500 °C in pure N_2, to removed physisorbed species. Reductions were performed with a constant gas flow of 35 ml/min, heating the sample from 200 to 800 °C with a heating rate of 10 °C/min and holding the sample at the maximum temperature for 30 min. The reduction kinetics of composite samples with CH_4 was investigated in a Netzsch STA 2500 Regulus apparatus at Politecnico di Torino, Torino (IT). Approximately 15 mg of powdered sample was loaded in an alumina pan and heated to 800 °C (ramp 10 °C/min) in pure N_2, and then exposed to 5% CH_4 in N_2 for 20 minutes. CL-SMR testing procedure is reported in chapter 2.

4.3. Results and discussion

4.3.1. Preliminary investigation of composite OC

Figure 4.1a shows the X-ray diffraction pattern of the pristine C2F. No crystalline phases except $Ca_2Fe_2O_5$ are observed above the detection limit of the instrument. Figure 4.1b shows an HRTEM-EDS image of a C2F particle. The particle appears as a large agglomerate with micrometric size. A high degree of sintering of C2F is expected given the high calcination temperature (1150 °C). Thereby, the pristine material has a very low surface area, corresponding to 0.57 m^2/g as calculated by Hg porosimetry. The EDS line scan confirms the homogeneity of the particle, as deduced from the almost constant Ca/Fe ratio along the line.

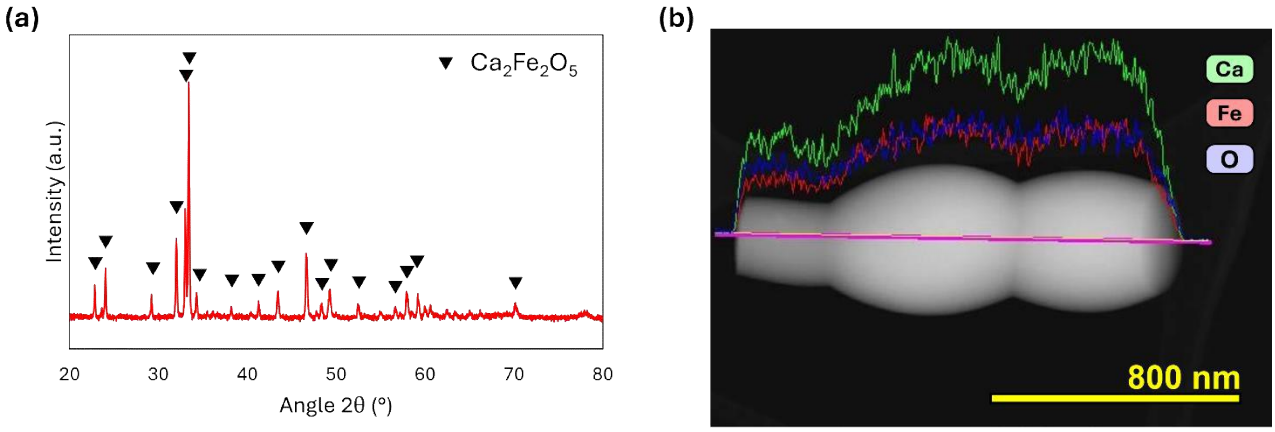

Fig. 4.1. (a) XRD pattern of the synthesized $Ca_2Fe_2O_5$ powder (PDF card: 00-047-1744). (b) HRTEM-EDS analysis of a single $Ca_2Fe_2O_5$ particle.

The redox behaviour of C2F was investigated by temperature-programmed reduction in a TGA. Fig 4.2 shows the weight change of the sample when heated at 10 °C/min up to 900 °C under a 5% H_2 in N_2 atmosphere. A first weak weight loss is observed between 520 and 570 °C, attributed to the presence of small amounts of reducible impurity phases [19]. The major weight loss starts at approximately 620 °C and proceeds at a steady pace after reaching 770 °C. 10 minutes after reaching the maximum temperature the weight stabilized to a value corresponding to the stoichiometric C2F to Fe and CaO reaction (82.3% of the initial weight), indicating the complete conversion of the solid. Once reduced, the large agglomerates observed in the pristine material assume a less compact and more porous morphology, with spheroidal metallic Fe particles of 100-200 nm embedded in a CaO matrix (figure 4.3). As observed in the previous chapter, the successive reductions and oxidations induces the development of a porous network that promotes the reactivity.

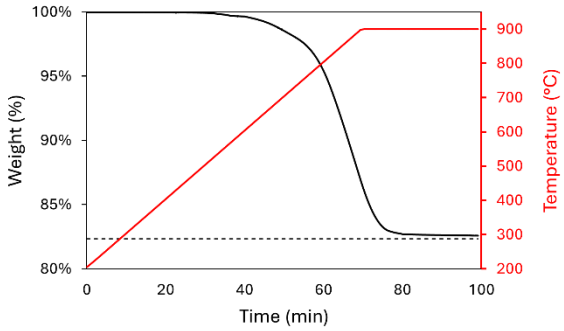

Fig.5.2. Temperature-programmed reduction of C2F in a TGA under a 5% H_2 in N_2 atmosphere. The temperature was varied with a 10 °C/min rate up to 900 °C and held for 30 minutes.

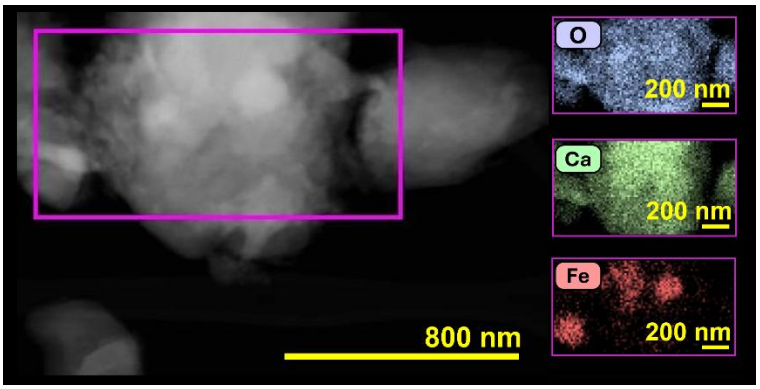

Fig 5.3. HRTEM-EDS image of C2F after complete reduction in H_2.

From XRD (figure 4.4), the pristine $Ce_{0.8}Zr_{0.2}O_2$ powder appear as a single cubic phase, analogously to pure CeO_2 (PDF card 00-34–0394). A shift of the diffraction peaks towards higher angles is observed in respect of CeO_2, due to a decrease if the lattice parameter induced by the smaller Zr^{4+} cations. The surface area corresponds to 23.4 m^2/g. Comparatively, CZ reduction (figure 4.5) starts at lower temperatures than C2F, exhibiting a first weight loss between 460 and 620 °C, attributed to the reduction of surface Ce^{4+} species and a partially overlapped second contribution up to 900 °C, attributed to the reduction of Ce^{4+} cations in the bulk [20]. Zr doping is known to significantly enhance the reducibility of CeO_2, as well as the O^{2-} transport in the lattice [20].

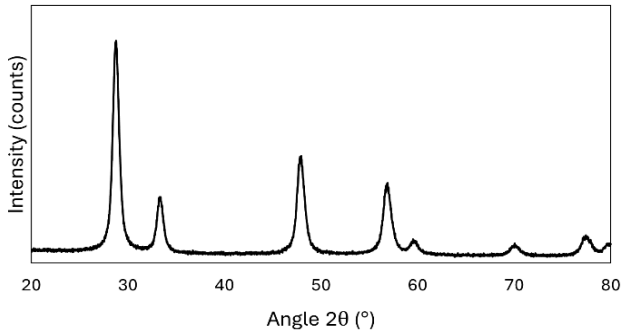

Fig. 4.4. Diffraction pattern of pristine $Ce_{0.8}Zr_{0.2}O_2$.

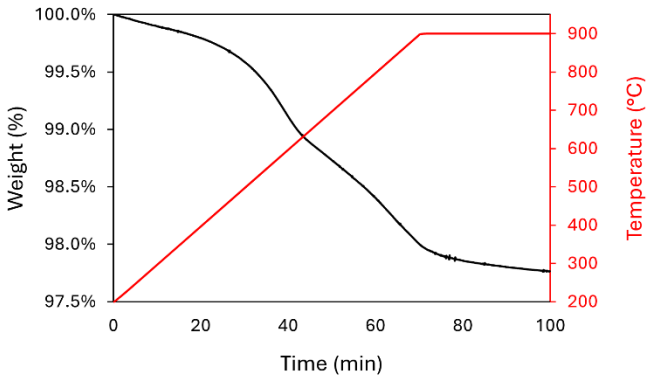

Fig. 4.5. Temperature-programmed reduction of $Ce_{0.8}Zr_{0.2}O_2$ in a TGA with 5% H_2.

Mechanical mixtures of C2F and CeO_2-ZrO_2 solid solutions were reported to exhibit faster reduction rates and higher effective OTC in respect of the single components [16]. To further investigate the role of the mixture, particularly regarding the reduction kinetics, the reactivity of C2F, CZ and their physical mixture, realized by physically mixing equal amounts of C2F and CZ, with CH_4 was evaluated by isothermal reduction at 800 °C in a microreactor. A uniform reduction time of 16.5 min was adopted for all samples, corresponding to a CH_4 to C2F molar ratio of 9 for the composite sample. The same reduction time was maintained for the following CL-SMR cycles performed on the samples. Figure 4.6 shows the molar fraction of the product gases at the outlet of the microreactor. C2F reduction begins with a short-lived evolution of mostly total combustion products (H_2O and CO_2). Afterwards, H_2 and CO production become dominant and keep increasing over time. CZ show a similar behaviour, beginning with a fast consumption of surface oxygen species that are selective for CH_4 total oxidation [21]. Later on, a stable syngas production with very little residual H_2O and CO_2 production took place. The physical mixture of C2F and CZ exhibit the same features of the individual components, but an enhanced H_2 and CO evolution is observed in respect of the linear combination of the two previous cases.

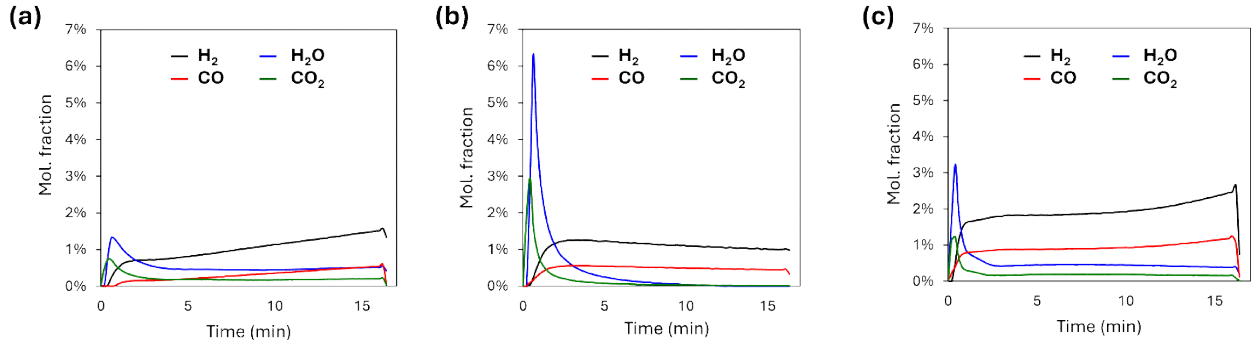

Fig. 2.6. Molar fraction of the reaction products measured at the reactor outlet during the isothermal reduction of (a) C2F, (b) CZ and (c) a 50:50 (wt.) physical mixture of C2F and CZ in 10% CH_4 at 800 °C.

To provide additional indications on the favourable effect of C2F-CZ interfaces on the reactivity, the physically mixed material was subjected to mild energy ball milling to increase the contact between the phases. The powders were milled in a Pulverizette 2 apparatus operated with a single 10mm ⌀ stabilized ZrO_2 ball for 10 min at 15 Hz. While the milling process did not significantly affect the surface area (11.4 m^2/g and 12.0 m^2/g before and after the milling), a faster reduction was observed for the milled sample (figure 4.7). After approximately 10 minutes, a steady rise in the syngas production was observed. Given the observed behaviour of C2F, whose oxygen exchange

rate increase with the reduction degree, it is hypothesized that the mechanical energy introduced by the milling induced the dispersion of the phases and the creation of superficial lattice defects, in turn promoting its reducibility. A further indication of this is provided by the H_2-TPR profiles (figure 4.8). The milled sample displays a shift of approximately 90 °C towards lower temperatures of the low temperature contribution, while after 550 °C the two profiles are almost superimposable. Further investigations (such as high-resolution electron microscopy) are required to verify the effect of milling on the morphological and surface features of the sample.

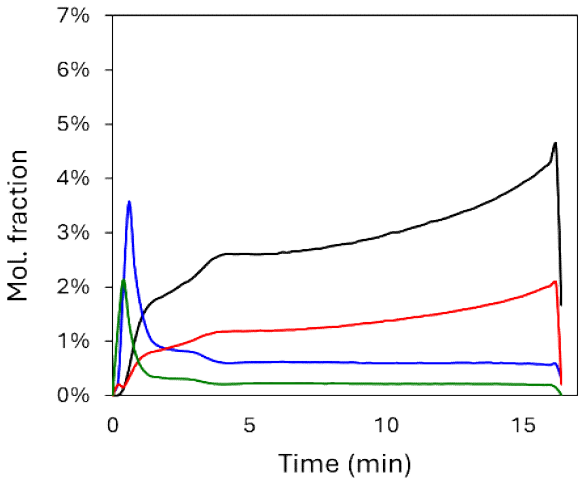

Fig. 4.7. Molar fraction of the reaction products measured at the reactor outlet during the isothermal reduction of a 50:50 (wt.) physical mixture of C2F and CZ subjected to mild energy ball milling prior to the test.

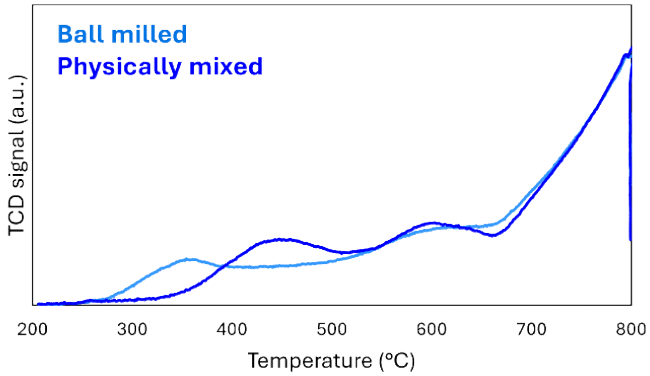

Fig. 4.8. H_2-TPR profiles of C2F-CZ composite samples after 20 CL-SMR cycles.

Figure 4.9 reports the fuel conversion and the CO gas phase selectivity of the composite OC materials in respect of the single components, referred to the reduction step of isothermal CL-SMR cycles. Both the composite samples exhibit a higher fuel conversion in respect of the individual components, further indicating the promotional effect of their co-presence. The enhanced syngas productivity of the composite samples is reflected in their higher CO selectivity. The ball milled sample initially showed a higher fuel conversion in respect of the physically mixed one. Nevertheless, a slight decrease was observed in the first 5 cycles, after which it stabilized at around 13%. X-ray diffraction patterns (figure 4.10) of the physically mixed and the milled samples after 20 CL-SMR cycles do not provide evidence of solid-state interaction between the two components, showing only a minor segregation of Fe_2O_3 and CaO. Some crystalline SiO_2 is present due to contamination from the quartz wool plug used to hold the reactive material inside the reactor. In the milled sample, the milling procedure induced a slight decrease of the

C2F average crystallite size according to the Sherrer equation (table 4.1). After the test, in both cases the C2F crystallite size decreased, while CZ crystallite size increased. The increase is slightly larger in the physically mixed sample.

Tab. 4.1. Average components crystallite size of the physically mixed and ball milled composite C2F-CZ samples before and after 20 CL-SMR cycles, calculated by Sherrer equation.

	Average crystallite size (nm)	
	C2F	**CZ**
	Physically mixed	
Pristine	49	10
Tested for 20 CL-SMR cycles	36	25
	Ball milled	
Pristine	46	10
Tested for 20 CL-SMR cycles	34	21

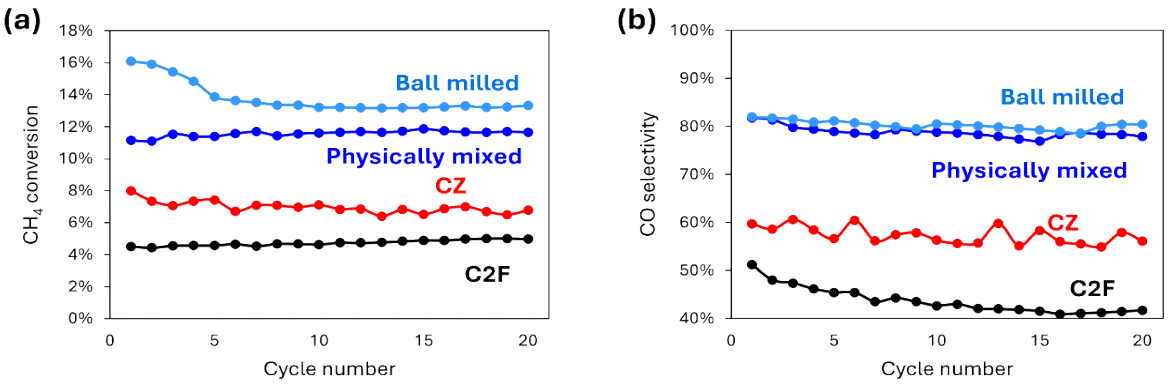

Fig. 4.9. (a) CH_4 conversion and (b) CO selectivity of C2F, CZ and C2F-CZ composite samples in 20 CL-SMR cycles.

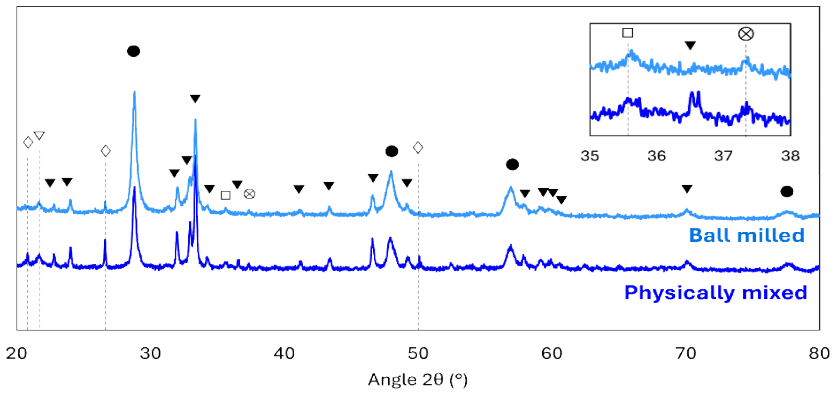

Fig. 4.10. XRD patterns of C2F-CZ composite samples after 20 CL-SMR cycles. (●) CZ. (▼) C2F. (⊗) CaO, PDF card 01-075-0264. (□) Fe_2O_3, PDF card 01-084-0311. (◊) Quartz, PDF card 01-078-1254. (▽) Cristobalite, PDF card 01-076-0941.

4.3.2. Nickel introduction

Given the observed favourable effect of blending C2F and CZ to realize composite oxygen carriers, a further assessment has been made on the introduction into such systems of Ni as catalytically active phase towards CH_4 activation and steam reforming [22, 23]. Ni is widely known in the chemical looping literature to improve both C2F [10, 24-30] and Ce-based materials [31-36] reduction kinetics and effective OTC with various fuels, including CH_4. Nevertheless, some authors report a progressive decrease in the reduction rates due to the chemical interaction between C2F and Ni, since it induces the migration of Ni and Fe outside the brownmillerite (C2F) structure and the agglomeration of catalytically active particles. It is believed that the observed deactivation is linked with the continuous formation and destruction of mixed Ni and Fe phases, such as Ni-Fe alloys and $NiFe_2O_4$ spinel-type oxides. [10, 26, 28, 30]. In some cases, the interposition of a physical barrier (such as extra framework CaO) between C2F and Ni could prevent undesired phases formation and improve Ni particles dispersion [30]. In the present work, a catalytic amount of Ni (Ni/Fe molar ratio equal to 0.0256) was introduced in the composite OC system by three different methods, namely (i) by selective wet impregnation of C2F, (ii) by selective wet impregnation of CZ and (iii) by doping the C2F lattice. A series of composite OC materials has been prepared by physical mixing of Ni-modified C2F and CZ, keeping the 50:50 C2F:CZ mass ratio and the Ni/Fe molar ratio to 0.05. The investigated combinations are reported in table 4.2.

Tab. 4.2. Ni-containing composite samples prepared by simple mixing of unmodified and Ni-modified C2F and CZ in a 50:50 weight ratio.

Sample ID	C2F-based component	CZ-based component
C2F-CZ (reference)	C2F	CZ
impC2F-CZ	Ni-impregnated C2F (1.06% wt.)	CZ
dopC2F-CZ	$Ca_2Fe_{1.95}Ni_{0.05}O_5$	CZ
C2F-impCZ	C2F	Ni-impregnated CZ (1.06% wt.)

The redox properties and the CH_4 activation capability of the individual components prepared has been investigated respectively by H_2 temperature-programmed reductions in a TGA and by CH_4 temperature-programmed reduction in a microreactor setup. Figure 4.11 shows the diffraction patterns of the pristine C2F, the Ni-impregnated C2F (impC2F) and the Ni-doped C2F (dopC2F). The impregnated sample do not show any peak pertaining to NiO (the expected product of the impregnation procedure). The phenomenon is attributed to the small size of the particles and the high content of Fe atoms of the sample, which increase the X-ray background due to fluorescent radiation emitted Fe atoms following inelastic X-ray scattering [37]. The doped C2F show a clear shift of diffraction peaks towards higher angles, attributed to the substitution of Fe^{3+} cations with Ni^{2+} and the related generation of oxygen vacancies needed to maintain charge neutrality in the lattice, that in turn induced a lattice shrinkage. Another indication of the successful insertion of Ni into the brownmillerite lattice is the absence of peaks related to segregated NiO and $NiFe_2O_4$, although the measurement suffers from the same limitations discussed above. The nanoscale homogeneity of the doped C2F was checked by HRTEM-EDS analysis (figure 4.12), which confirmed a homogeneous Ni distribution at the individual particles level.

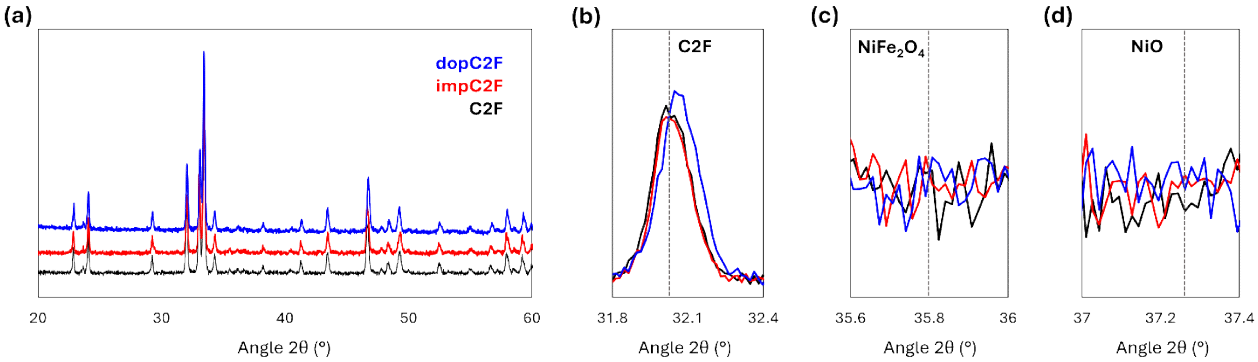

Fig. 4.11. XRD profiles of pristine C2F (black curve), Ni-impregnated C2F (impC2F, red curve) and Ni-doped C2F (dopC2F, blue curve) in the (a) 20-60, (b) 31.8-32.4, (c) 35.6-36 and (d) 37-37.4 2 ranges. The position of characteristic peaks pertaining to C2F, $NiFe_2O_4$ (PDF card 01-086-2267) and NiO (PDF card 00-004-0835) are shown.

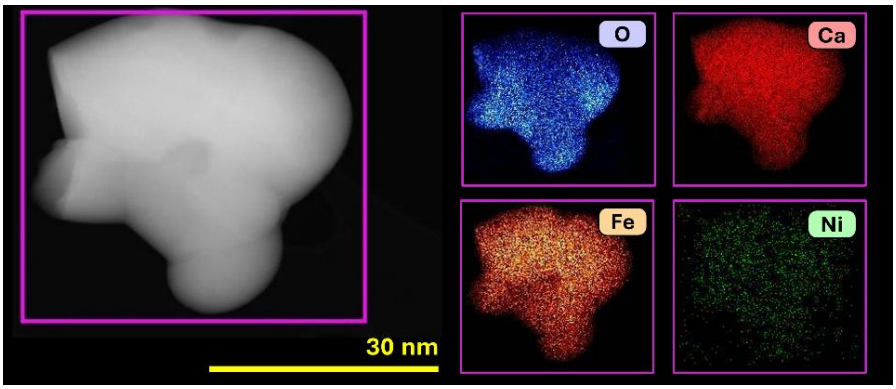

Fig. 4.12. HRTEM-EDS analysis of pristine $Ca_2Fe_{1.95}Ni_{0.05}O_5$ (dopC2F).

Figure 4.13 shows the weight loss of the modified C2F materials with 5% H_2 in N_2. The impregnated sample show a first weight loss between 520 and 580 °C, attributed to the reduction of NiO to Ni (which accounts for a 0.22% weight loss in respect of the total sample mass, according to the nominal Ni loading) and of Fe species in contact with Ni, which promote their reduction [38, 39]. The bulk of C2F follows the same reduction trend as the unmodified sample. The Ni-doped material start losing lattice oxygen at 650 °C and reach the full reduction before 860 °C. Experimental investigations and density functional theory (DFT) simulations report that the substitution of Fe^{3+} with Ni^{2+} induces a distortion in the C2F lattice which lowers the oxygen vacancies energy of formation and the lattice oxygen diffusion energy barrier [27, 28].

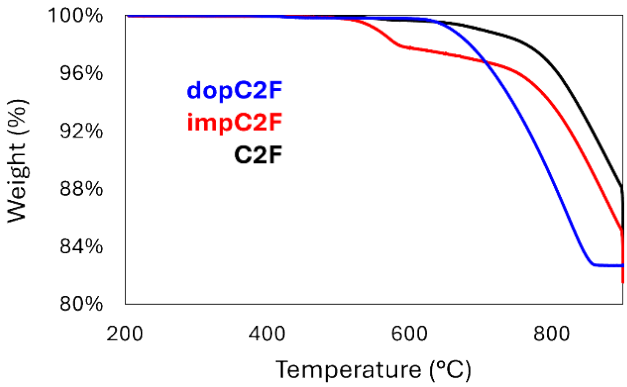

Fig. 4.13. Temperature-programmed reduction of pure and Ni-modified C2F in a TGA with 5% H_2.

Figure 4.14 shows the temperature-programmed reduction of the same three materials with CH_4. Pure C2F start reacting with CH_4 at 750 °C. The oxygen exchange proceeds at an increasing rate until the maximum temperature is reached. After 12 minutes at 880°C, the evolution of oxygen-containing gas stops abruptly, and only H_2 is produced by CH_4 pyrolysis. The impC2F sample starts reacting with CH_4 at a much lower temperature. Once reached 490 °C, a spike in the outlet concentration of H_2 and CO is observed, attributed to Superficial NiO reduction. Subsequently the production of H_2 and CO increases until 660 °C, when the CO production decreases quickly and only H_2 is observed. The dopC2F sample shows the same features as the undoped one but at lower temperatures. The material starts to react at 660 °C and the oxygen exchange stops before reaching the maximum temperature. After the test, the samples have been oxidized back (20 minutes in 10% H_2O followed by 10 minutes in 5% O_2) and brought back to ambient temperature for XRD analysis.

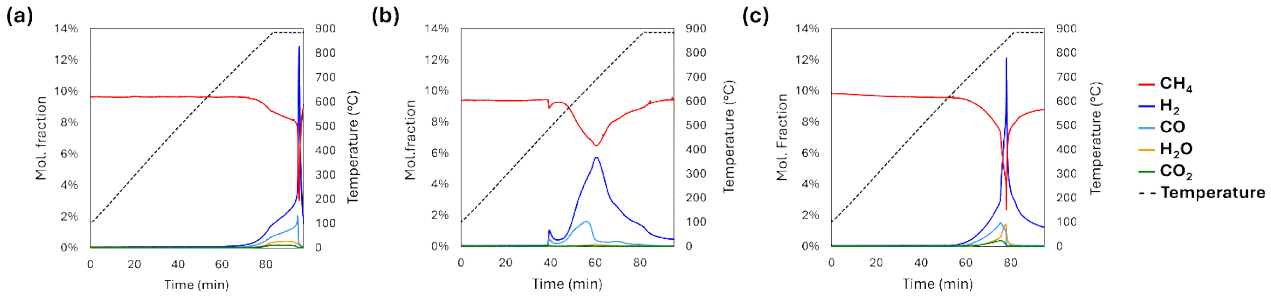

Fig. 4.14. Temperature-programmed reduction in a microreactor of (a) C2F, (b) Ni-impregnated C2F and (c) Ni-doped C2F in 10% CH_4.

The diffraction patterns of the samples before and after the test are reported in figure 4.15. All the three samples show a decrease in the intensity of the main C2F peak at 33.4°, less evident for the Ni-doped C2F sample. The phenomenon is due to the C2F recrystallization that takes place at 800 °C after the temperature programmed reduction. Given the large difference between the calcination temperature (1150 °C for the C2F, 950 °C for the Ni-doped C2F) and the oxidation temperature, the newly formed C2F crystallites have a smaller average size [40]. Both the Ni-modified samples show the presence of segregated phases, identified as spinel $NiFe_2O_4$ for the impC2F and both $NiFe_2O_4$ and NiO for the doped sample. The formation of segregated phases was reported to reduce oxygen carrier performances [10, 26].

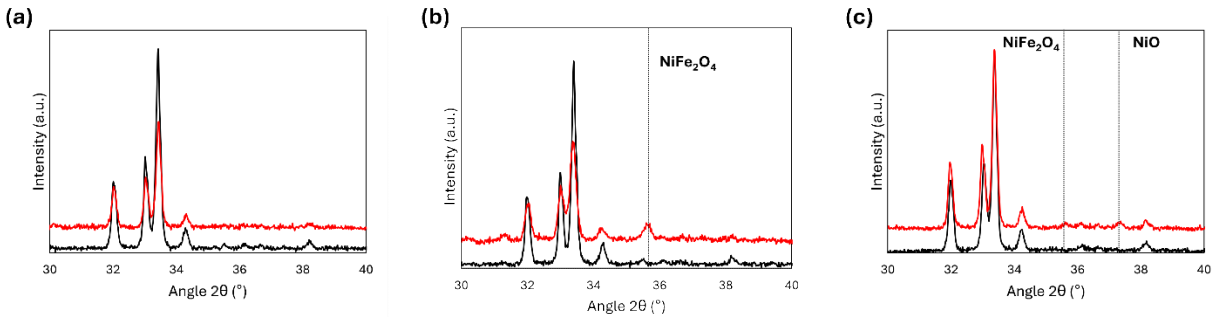

Fig 4.15. XRD detail of (a) C2F, (b) Ni-impregnated C2F and (c) Ni-doped C2F before and after CH_4-TPRs. Peak position of characteristic peaks pertaining to $NiFe_2O_4$ (PDF card 01-086-2267) and NiO (PDF card 00-004-0835) are shown.

Figure 4.16 shows the reduction behaviour in 5% H_2 of the Ni-impregnated CZ. Ni nanoparticles improve the reducibility of CZ at low temperatures (below 500 °C), promoting the reduction of surface Ce^{4+} species [41]. The bulk reduction takes place above 600 °C in a similar fashion for the modified and unmodified samples. As for the C2F-based materials, impCZ reactivity with CH_4 was investigated by CH_4-TPR in a microreactor and compared with pure CZ. Results are shown in figure 4.17. Pure CZ starts reacting with CH_4 at 680°C, producing H_2 and CO with an almost complete selectivity. Above 830°C the oxygen exchange rate (observed from the CO production) decreases, indicating the depletion of available lattice oxygen. Simultaneously, a significant amount of H_2 is produced by CH_4 pyrolysis. The Ni-doped sample show a spike in CH_4 conversion at 490 °C, analogously to Ni-impregnated C2F in figure 4.14, attributed to the reduction of NiO. The spike is followed by a significant production of H_2 accompanied by a limited CO evolution. While the CO production continues approximately at the same rate, H_2 concentration decreases after 540°C, supposedly due to the inhibition effect of solid carbon deposits on metallic Ni active sites, formed by pyrolysis reactions. Another increase in the H_2 production can be observed from 750 to 850 °C, attributed to the lattice oxygen depletion of CZ and the onset of pyrolysis reaction on the surface of CZ, as observed for the unmodified sample. in consequence, it can be observed how metallic Ni deposited on the surface of CZ could promote oxygen exchange at temperatures below 700 °C, but at the cost of drastically increase the selectivity towards unwanted solid carbon, thanks to the well-known catalytic activity of Ni metal [42].

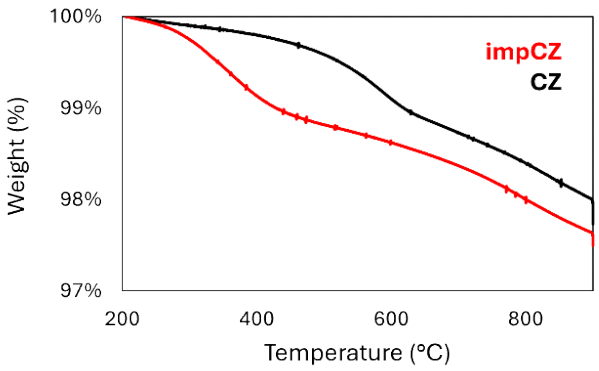

Fig. 4.16. Temperature-programmed reduction of pure and Ni-impregnated CZ in a TGA with 5% H_2.

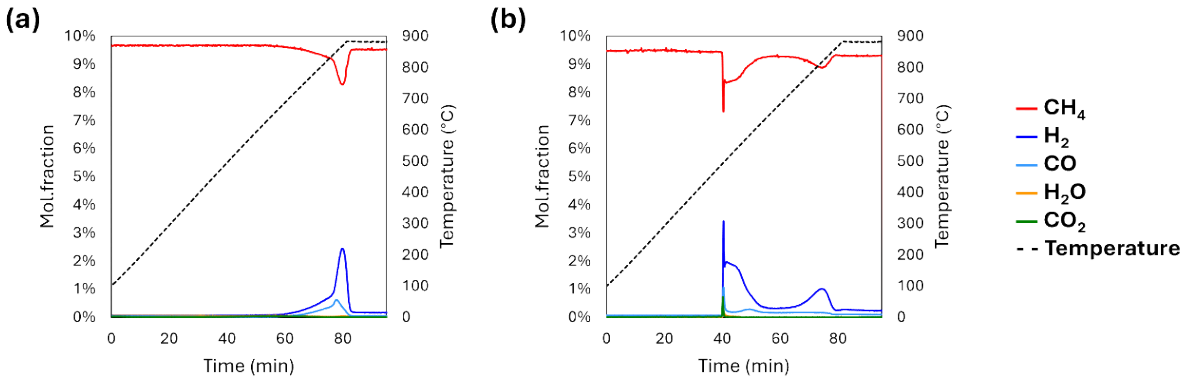

Fig. 4.17. Temperature-programmed reduction in a microreactor of (a) pure and (b) Ni-impregnated CZ in 10% CH_4.

The reactivity of the composite OC materials, listed in table 2.1, was evaluated by means of isothermal reduction in a TGA, using 5% CH_4 in He as reducing gas. Results are reported in figure 4.18. All the Ni-containing samples exhibit a faster weight loss in respect of the reference sample. However, in the impC2F and dopC2F samples, in which Ni is present in the bulk or on the surface of C2F the reduction rates are slower than the C2F-impCZ sample, in which Ni is selectively impregnated on the CZ only. In the latter case, the chemical interaction between C2F and Ni is prevented, while in the others Ni-Fe alloys and mixed oxides may form, as seen in figure 4.15. These mixed phases may reduce the number of Ni active sites, thus affecting the oxygen exchange rate.

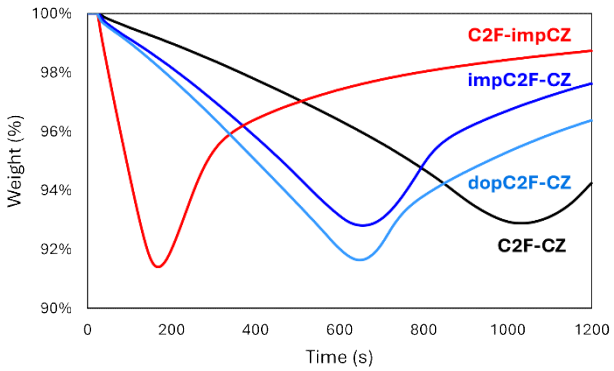

Fig. 4.18. Isothermal reduction of Ni-modified C2F-CZ composite samples at 800 °C and 5% CH_4 in a TGA.

Testing the composite OCs for CL-SMR cycles gave coherent results, with the C2F-impCZ showing an almost complete fuel conversion at the first cycle, far higher than the other samples (figure 4.19). While all samples showed a decrease in the reactivity from the first and the last cycle, for the C2F-impCZ the drop in CH_4 conversion was drastic, going from 95 to 30% in the first 10 cycles and then stabilizing afterwards. X-ray diffraction shows only minor amount of segregated impurities, such as CaO and Fe_2O_3. No Ni-containing crystalline phase was observed within the analysis detection range (figure 4.20).

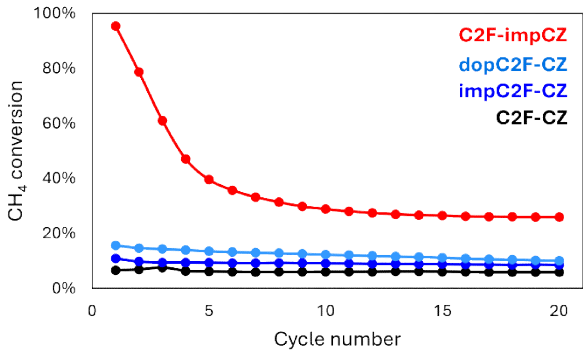

Fig. 4.19. CH_4 conversion of Ni-modified C2F-CZ composite samples in 20 CL-SMR cycles.

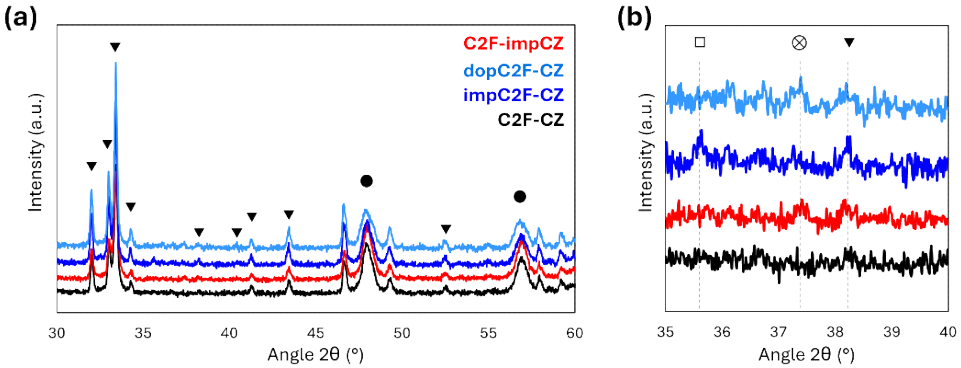

Fig. 4.20. XRD patterns of Ni-modified C2F-CZ composite samples after 20 CL-SMR cycles in the (a) 30-60 and (b) 30-35 ° 2θ range. (●) CZ. (▼) C2F. (⊗) CaO, PDF card 01-075-0264. (□) Fe_2O_3, PDF card 01-084-0311.

To evaluate the effect of the reducible CZ support on the Ni reactivity, a comparative test was performed using Ni-loaded ZrO_2 and Ni-loaded CeO_2. Commercial ZrO_2 and CeO_2 powder was calcined at 850 °C and impregnated with Ni to obtain the same metal loading as the impCZ sample. The surface area of the prepared catalysts was equal to 13.6 and 3.9 m^2/g for the impregnated ZrO_2 and CeO_2 respectively, significantly lower than that of CZ (23.4 m^2/g) due to the lower thermal stability of the materials in respect of CZ and the differences in the synthesis procedure [43]. Figure 4.21a shows the CH_4-TPR of the three catalysts. Ni reduction clearly takes place at a lower temperature on CeO_2 (490 °C) and CZ (495 °C) in respect of ZrO_2 (590 °C), as observed from the spike in CH_4 consumption. Despite having a significantly different surface area, which may influence the dispersion of Ni and its interaction with the support, NiO reduction takes place at a very similar temperature for both the Ce-containing supports. In fact, CeO_2 has been widely reported to enhance the interaction between NiO and methane [44]. Overall, the amount of converted methane is significantly lower for the ZrO_2 case, indicating the positive effect of the CZ support not only on NiO reducibility but also on CH_4 activation itself. In CL-SMR cycles (figure 4.21b), the composite C2F-impZrO_2 sample displays a significantly lower initial performance in respect of the CZ-containing counterpart, reflecting the lower activity of impZrO_2 towards CH_4 activation. In the successive redox cycles, the two samples follow a significantly different reactivity pattern, with the C2F-impZrO_2 sample showing an oscillating behaviour in terms of CH_4 conversion in the first 4 cycles and then slowly deactivating later on. After

the first 8 cycles, the reactivity of the two samples is almost superimposable, and the advantages of using the CZ support are somewhat lost.

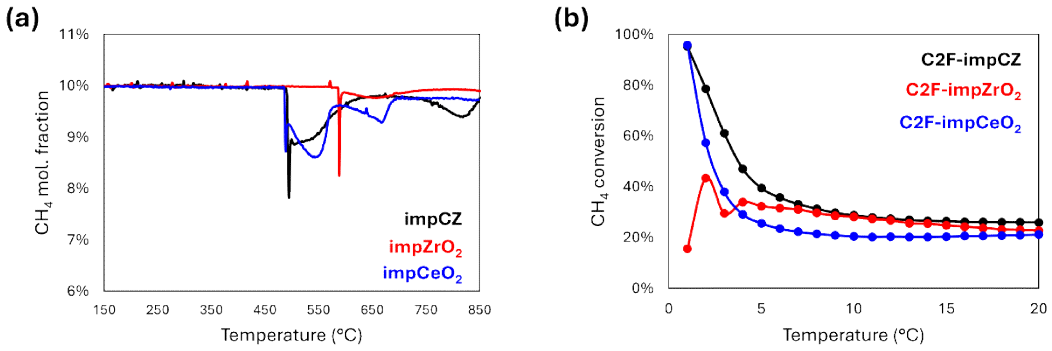

Fig. 4.21. (a) CH_4-TPR of Ni-impregnated CZ (impCZ, black curve), ZrO_2 (impZrO$_2$, red curve) and CeO_2 (impCeO$_2$, blue curve). Ni loading 1.06% wt. (b) CH_4 conversion of C2F-impCZ (black curve), C2F-impZrO$_2$ (red curve) and C2F-impCeO$_2$ (blue curve) composite samples in 20 CL-SMR cycles.

To elucidate the causes of the fast deactivation of the C2F-impCZ sample, the composite material was tested for 1 and 10 cycles, in addition to the 20 cycles test, and characterized by N_2 physisorption and X-ray photoelectron spectroscopy (XPS). A strong loss of specific surface area is observed over the redox cycles, following a similar decreasing trend as the sample CH_4 conversion (the black curve in figure 4.21b). Given the very low surface area of pristine C2F (0.6 m^2/g), the surface area loss is attributed to a strong sintering of CZ support, which in turn can greatly affect the number of Ni active sites exposed to the gaseous environment by facilitating metallic nanoparticles sintering and embedment in the support matrix. The loss of surface area well correlates to a decrease in the superficial (Ce,Zr)/(Ca,Fe) ratio, as evaluated by XPS.

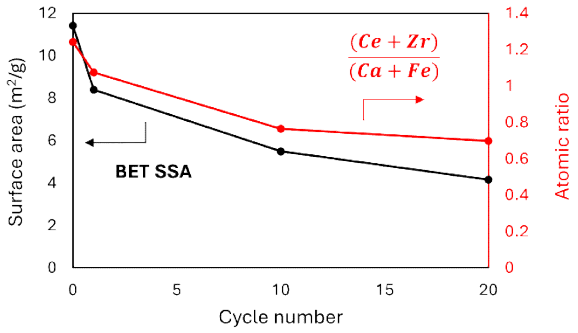

Fig 4.22. Evolution of the specific surface area (black curve) and surface (Ce,Zr)/(Ca,Fe) atomic ratio of the composite C2F-impCZ OC material subjected to CL-SMR cycles.

The amount of Ni exposed to the surface could be only roughly estimated due to the partial overlapping of the Ni 2p and the Ce 3d regions, the low Ni content of the sample and the high noise-to-signal ratio that affected the measurements following samples charging phenomena under the X-ray beam. To improve the accuracy of the evaluation of the area belonging to Ni $2p_{3/2}$ photoelectron lines, the XPS spectra were fitted following the spectral fitting parameters relative to NiO and $Ni(OH)_2$ provided in [45], since those compounds are the most likely to form upon exposure to steam and O_2 at high temperature and to ambient air [46]. Nevertheless, for the

abovementioned reasons the results have to be considered qualitative rather than quantitative. Figure 4.23 shows the variation of the Ni atomic coverage, together with the fitted spectral profiles of Ni $2p_{3/2}$. The analysis suggests a notable reduction in the number of Ni atoms on the surface after one CL-SMR cycle, and a progressive decrease during the following cycles, although very difficult to quantify. XPS spectra of the Ce 3d region (figure 4.24 show that all the cycled samples have a higher content of Ce^{4+} on the surface, as evidenced by the lower area of the V^0 and V' doublets, attributed to Ce^{3+} [47]. Superficial defect sites and oxygen vacancies has been found to enhance the redox properties of CeO_2 [48] and promote the metal-support interaction in CeO_2-supported catalysts [49].

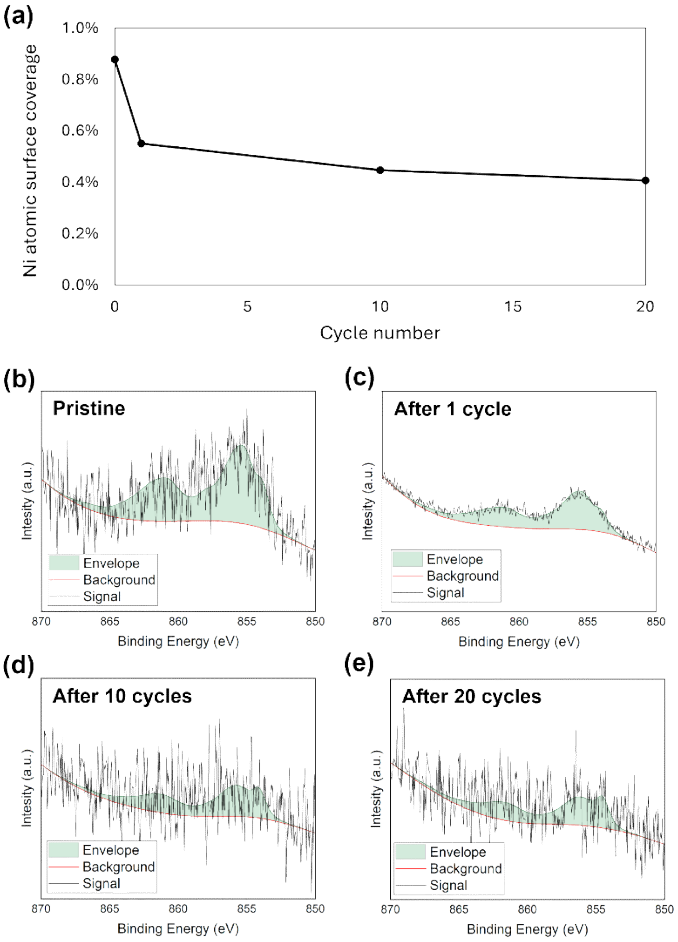

Fig. 4.23. (a) Estimated Ni atomic surface coverage of the composite C2F-impCZ OC material subjected to CL-SMR cycles. Ni $2_{p3/2}$ fitted spectral profiles of the (b) pristine, (c) cycled 1 time, (d) cycled 10 times and (d) cycled 20 times OC material.

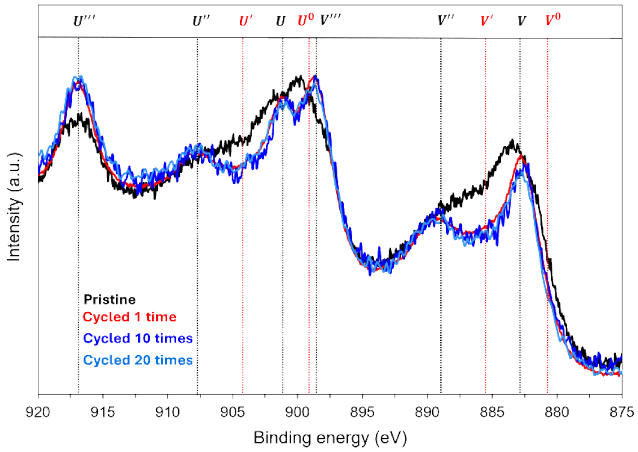

Fig. 4.24. Ce 3d spectral profiles of the pristine (black), cycled 1 time (red), cycled 10 times (blue) and cycled 20 times (bright blue) OC material.

The evolution of the composite sample morphology due to redox cycling was further investigated by SEM-EDS. The pristine sample (figure 4.25a, b) is composed by fine CZ particles (bright spots in the SEM image, as evinced by EDS) fairly spread over large C2F agglomerates. Moreover, the CZ particles appear as porous agglomerates of fine crystallites. After the test (figure 4.25c, d) the overall morphology appears preserved, but a certain sintering of the CZ particles is visible, as their porosity appears to be significantly reduced. Also the C2F agglomerates appear highly sintered. Overall, the undertaken analyses evidenced significant changes in the morphology of the Ni-loaded CZ. The non-optimal stability of the OC components, particularly the support material for the Ni catalyst, is believed to be the critical factor affecting the composite OC reactivity, causing the reduction in the reactivity observed over subsequent CL-SMR cycles.

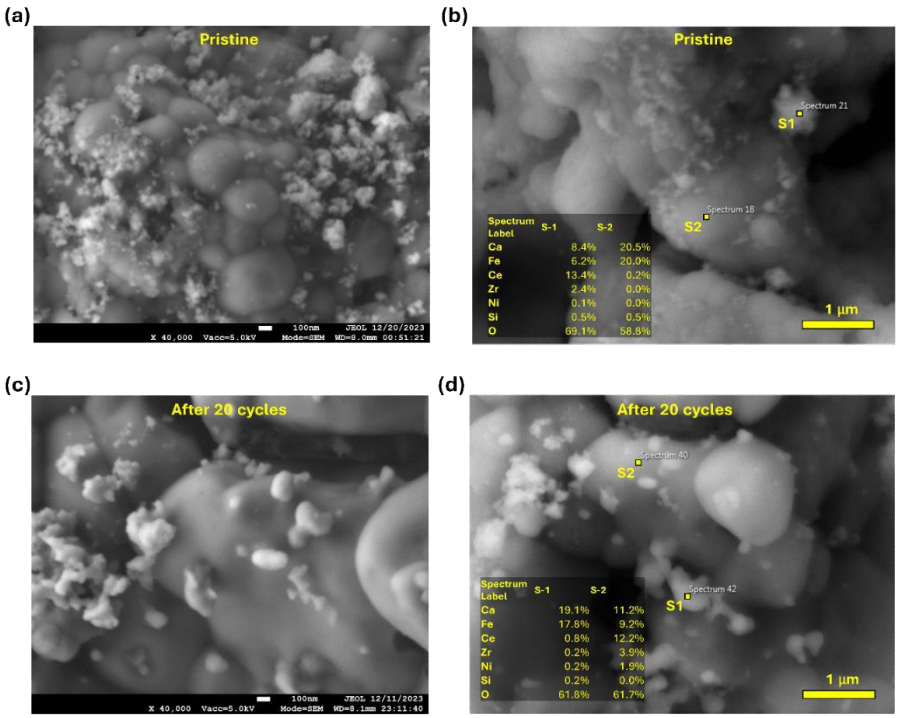

Fig. 2.24. SEM images and SEM-EDS analyses of C2F-impCZ before and after 20 CL-SMR cycles. The bright spots visible in the images are attributed to CZ particles, as for EDS spectra.

4.4. Conclusions

The present contribution investigates a novel strategy to enhance the reduction kinetics and overall CL-SMR performances of C2F-based OCs. First, C2F-CZ composite samples were prepared, characterized, and tested for CL-SMR cycles, finding that even the simple physical mixing of the two powders can enhance the fuel conversion in the reduction step and improve the syngas selectivity at a fixed step time. The enhancement was found not related to bulk solid-state interactions between the C2F and the CZ. A further reactivity enhancement was obtained by introducing catalytic amounts of Ni, thanks to its well-known ability towards CH_4 activation. Among the different Ni deposition methods investigated (C2F lattice doping, selective impregnation of C2F and of CZ), the largest improvement in the OC reduction kinetics was obtained by depositing Ni selectively over CZ. While in the aforementioned case the chemical interaction between Fe and Ni is prevented by the CZ support, which acts as a physical barrier, in the other cases involving Ni-modified C2F the formation of mixed oxides was observed, a phenomenon known to be detrimental for the stability and reactivity with CH_4 [10]. The rapid loss of activity of the C2F – Ni-impregnated CZ sample over CL-SMR cycles was found to be linked to the sintering of CZ, which in turn affected the stability of the catalyst. The interplay between the C2F and the Ni-based catalyst will be thoroughly investigated in the following chapter.

4.5. References

[1] IEA (2022), World Energy Outlook 2022, IEA, Paris https://www.iea.org/reports/world-energy-outlook-2022, Licence: CC BY 4.0 (report); CC BY NC SA 4.0 (Annex A)

[2] Bachmann, M., Völker, S., Kleinekorte, J., & Bardow, A. (2023). Syngas from What? Comparative Life-Cycle Assessment for Syngas Production from Biomass, CO2, and Steel Mill Off-Gases. *ACS Sustainable Chemistry & Engineering*, *11*(14), 5356–5366. https://doi.org/10.1021/acssuschemeng.2c05390

[3] Zheng, H., Jiang, X., Gao, Y., Tong, A., & Zeng, L. (2022g). Chemical looping reforming: process fundamentals and oxygen carriers. *Discover Chemical Engineering*, *2*(1). https://doi.org/10.1007/s43938-022-00012-3

[4] Voitic, G., & Hacker, V. (2016). Recent advancements in chemical looping water splitting for the production of hydrogen. *RSC Advances*, *6*(100), 98267–98296. https://doi.org/10.1039/c6ra21180a

[5] Svoboda, K., Slowinski, G., Rogut, J., & Baxter, D. (2007b). Thermodynamic possibilities and constraints for pure hydrogen production by iron based chemical looping process at lower temperatures. *Energy Conversion and Management*, *48*(12), 3063–3073. https://doi.org/10.1016/j.enconman.2007.05.019

[6] Yu, Z., Yang, Y., Yang, S., Zhang, Q., Zhao, J., Fang, Y., Hao, X., & Guan, G. (2018b). Iron-based oxygen carriers in chemical looping conversions: A review. *Carbon Resources Conversion*, *2*(1), 23–34. https://doi.org/10.1016/j.crcon.2018.11.004

[7] Ismail, M., Liu, W., Dunstan, M. T., & Scott, S. A. (2016c). Development and performance of iron-based oxygen carriers containing calcium ferrites for chemical looping combustion and production of hydrogen. *International Journal of Hydrogen Energy*, *41*(7), 4073–4084. https://doi.org/10.1016/j.ijhydene.2015.11.066

[8] Shaula, A., Pivak, Y., Waerenborgh, J., Gaczyñski, P., Yaremchenko, A., & Kharton, V. (2006b). Ionic conductivity of brownmillerite-type calcium ferrite under oxidizing conditions. *Solid State Ionics*, *177*(33–34), 2923–2930. https://doi.org/10.1016/j.ssi.2006.08.030

[9] Shah, V., Cheng, Z., Baser, D. S., Fan, J. A., & Fan, L. (2020). Highly Selective Production of Syngas from Chemical Looping Reforming of Methane with CO_2 Utilization on MgO-supported Calcium Ferrite Redox Materials. *Applied Energy*, *282*, 116111. https://doi.org/10.1016/j.apenergy.2020.116111

[10] Hosseini, D., Donat, F., Abdala, P. M., Kim, S. M., Kierzkowska, A. M., & Müller, C. R. (2019c). Reversible exsolution of dopant improves the performance of $Ca_2Fe_2O_5$ for chemical looping hydrogen production. *ACS Applied Materials & Interfaces*, *11*(20), 18276–18284. https://doi.org/10.1021/acsami.8b16732

[11] Hu, J., Buelens, L., Theofanidis, S., Galvita, V. V., Poelman, H., & Marin, G. B. (2016). CO_2 conversion to CO by auto-thermal catalyst-assisted chemical looping. *Journal of CO_2 Utilization*, *16*, 8–16. https://doi.org/10.1016/j.jcou.2016.05.006

[12] Zeng, D., Qiu, Y., Li, M., Ma, L., Cui, D., Zhang, S., & Xiao, R. (2020b). Spatially controlled oxygen storage materials improved the syngas selectivity on chemical looping methane conversion. *Applied Catalysis B Environment and Energy*, *281*, 119472. https://doi.org/10.1016/j.apcatb.2020.119472

[13] Hu, J., Galvita, V., Poelman, H., & Marin, G. (2018b). Advanced Chemical looping Materials for CO_2 utilization: A review. *Materials*, *11*(7), 1187. https://doi.org/10.3390/ma11071187

[14] Hu, J., Galvita, V. V., Poelman, H., Detavernier, C., & Marin, G. B. (2018). Catalyst-assisted chemical looping auto-thermal dry reforming: Spatial structuring effects on process efficiency. *Applied Catalysis B Environment and Energy, 231*, 123–136. https://doi.org/10.1016/j.apcatb.2018.03.004

[15] Shafiefarhood, A., Hamill, J. C., Neal, L. M., & Li, F. (2015b). Methane partial oxidation using FeO_x@$La_{0.8}Sr_{0.2}FeO_{3-\delta}$ core–shell catalyst – transient pulse studies. *Physical Chemistry Chemical Physics*, *17*(46), 31297–31307. https://doi.org/10.1039/c5cp05583k

[16] Wang, L., Lin, Y., Huang, Z., Zeng, K., & Huang, H. (2022). Conversion of carbon dioxide to carbon monoxide: Two-step chemical looping dry reforming using $Ca_2Fe_2O_5$–$Zr_{0.5}Ce_{0.5}O_2$ composite oxygen carriers. *Fuel*, *322*, 124182. https://doi.org/10.1016/j.fuel.2022.124182

[17] Pans, M. A., Gayán, P., Abad, A., García-Labiano, F., De Diego, L. F., & Adánez, J. (2013). Use of chemically and physically mixed iron and nickel oxides as oxygen carriers for gas combustion in a CLC process. *Fuel Processing Technology*, *115*, 152–163. https://doi.org/10.1016/j.fuproc.2013.05.013

[18] More, A., & Veser, G. (2016b). Physical mixtures as simple and efficient alternative to alloy carriers in chemical looping processes. *AIChE Journal*, *63*(1), 51–59. https://doi.org/10.1002/aic.15380

[19] Sukma, M. S., Zheng, Y., Hodgson, P., & Scott, S. A. (2022b). Understanding the Behavior of Dicalcium Ferrite ($Ca_2Fe_2O_5$) in Chemical Looping Syngas Production from CH_4. *Energy & Fuels*, *36*(17), 9410–9422. https://doi.org/10.1021/acs.energyfuels.2c01065

[20] Trovarelli, A. (2002). Catalysis by Ceria and related materials. In *Catalytic science series*. https://doi.org/10.1142/p249

[21] Zheng, Y., Li, K., Wang, H., Zhu, X., Wei, Y., Zheng, M., & Wang, Y. (2015). Enhanced activity of CeO_2–ZrO_2 solid solutions for Chemical-Looping reforming of methane via tuning the macroporous structure. *Energy & Fuels*, *30*(1), 638–647. https://doi.org/10.1021/acs.energyfuels.5b02151

[22] Ighalo, J. O., & Amama, P. B. (2023b). Recent advances in the catalysis of steam reforming of methane (SRM). *International Journal of Hydrogen Energy*, *51*, 688–700. https://doi.org/10.1016/j.ijhydene.2023.10.177

[23] Angeli, S. D., Monteleone, G., Giaconia, A., & Lemonidou, A. A. (2014). State-of-the-art catalysts for CH_4 steam reforming at low temperature. *International Journal of Hydrogen Energy*, *39*(5), 1979–1997. https://doi.org/10.1016/j.ijhydene.2013.12.001

[24] Cai, Y., Wang, C., Zhang, Z., Zhong, M., Wu, Q., Xiao, B., Xu, T., & Wang, X. (2023). Performance optimization of $Ca_2Fe_2O_5$ oxygen carrier by doping different metals for coproduction syngas and hydrogen with chemical looping gasification and water splitting. *Journal of the Energy Institute*, *111*, 101391. https://doi.org/10.1016/j.joei.2023.101391

[25] Shah, V., Cheng, Z., Mohapatra, P., & Fan, L. (2021). Enhanced methane conversion using Ni-doped calcium ferrite oxygen carriers in chemical looping partial oxidation systems with CO_2 utilization. *Reaction Chemistry & Engineering*, *6*(10), 1928–1939. https://doi.org/10.1039/d1re00150g

[26] Tang, G., Gu, J., Wei, G., Yuan, H., & Chen, Y. (2022). Reaction performance and mechanism of a $NiO/Ca_2Fe_2O_5$ oxygen carrier in Chemical looping gasification of cellulose. *Chemical Engineering Journal*, *451*, 137516. https://doi.org/10.1016/j.cej.2022.137516

[27] Xu, T., Wang, X., Zhao, H., Xiao, B., Liu, D., & Liu, W. (2022). Modulating lattice oxygen activity of $Ca_2Fe_2O_5$ brownmillerite for the co-production of syngas and high purity hydrogen via chemical looping steam reforming of toluene. *Applied Catalysis B Environment and Energy*, *320*, 122010. https://doi.org/10.1016/j.apcatb.2022.122010

[28] Zhang, S., & Guo, X. (2024). Co, Ni and Cu-doped $Ca_2Fe_2O_5$-based oxygen carriers for enhanced chemical looping hydrogen production. *Journal of the Energy Institute*, *114*, 101659. https://doi.org/10.1016/j.joei.2024.101659

[29] Alkhatib, K., Sukma, M. S., Scott, S. A., & Zheng, Y. (2024). Investigation of simultaneous production of H_2 and separable carbon from CH_4 in a fluidised bed of $NiO/Ca_2Fe_2O_5/CaO$ particles. *Fuel*, *377*, 132816. https://doi.org/10.1016/j.fuel.2024.132816

[30] Zheng, Y., Sukma, M. S., & Scott, S. A. (2023b). The exploration of $NiO/Ca_2Fe_2O_5/CaO$ in chemical looping methane conversion for syngas and H_2 production. *Chemical Engineering Journal*, *465*, 142779. https://doi.org/10.1016/j.cej.2023.142779

[31] Bhavsar, S., & Veser, G. (2013a). Reducible supports for Ni-based oxygen carriers in chemical looping combustion. *Energy & Fuels*, *27*(4), 2073–2084. https://doi.org/10.1021/ef400184b

[32] Pantaleo, G., La Parola, V., Deganello, F., Calatozzo, P., Bal, R., & Venezia, A. (2014). Synthesis and support composition effects on CH_4 partial oxidation over Ni–CeLa oxides. *Applied Catalysis B Environment and Energy*, *164*, 135–143. https://doi.org/10.1016/j.apcatb.2014.09.011

[33] Löfberg, A., Guerrero-Caballero, J., Kane, T., Rubbens, A., & Jalowiecki-Duhamel, L. (2017). Ni/CeO_2 based catalysts as oxygen vectors for the chemical looping dry reforming of methane for syngas production. *Applied Catalysis B Environment and Energy*, *212*, 159–174. https://doi.org/10.1016/j.apcatb.2017.04.048

[34] Liu, R., Zhang, X., Liu, T., Yao, X., Zhao, Z., Pei, C., & Gong, J. (2023). Dynamic oxygen migration and reaction over ceria-supported nickel oxides in chemical looping partial oxidation of methane. *Applied Catalysis B Environment and Energy*, *328*, 122478. https://doi.org/10.1016/j.apcatb.2023.122478

[35] Grams, J., Niewiadomski, M., Ryczkowski, R., Ruppert, A. M., & Kwapiński, W. (2016). Activity and characterization of Ni catalyst supported on CeO_2–ZrO_2 for thermo-chemical conversion of cellulose. *International Journal of Hydrogen Energy*, *41*(20), 8679–8687. https://doi.org/10.1016/j.ijhydene.2015.11.140

[36] Han, Y., Tian, M., Wang, C., Kang, Y., Kang, L., Su, Y., Huang, C., Zong, T., Lin, J., Hou, B., Pan, X., & Wang, X. (2021). Highly Active and Anticoke Ni/CeO_2 with Ultralow Ni Loading in Chemical Looping Dry Reforming via the Strong Metal–Support Interaction. *ACS Sustainable Chemistry & Engineering*, *9*(51), 17276–17288. https://doi.org/10.1021/acssuschemeng.1c06079

[37] Mos, Y. M., Vermeulen, A. C., Buisman, C. J. N., & Weijma, J. (2018). X-Ray diffraction of iron containing samples: the importance of a suitable configuration. *Geomicrobiology Journal*, *35*(6), 511–517. https://doi.org/10.1080/01490451.2017.1401183

[38] Sun, S., He, S., & Wu, C. (2022). Ni promoted Fe-CaO dual functional materials for calcium chemical dual looping. *Chemical Engineering Journal*, *441*, 135752. https://doi.org/10.1016/j.cej.2022.135752

[39] Huang, J., Liu, W., Yang, Y., & Liu, B. (2018b). High-Performance Ni–Fe redox catalysts for selective CH_4 to syngas conversion via chemical looping. *ACS Catalysis*, *8*(3), 1748–1756. https://doi.org/10.1021/acscatal.7b03964

[40] Okpara, E. C., Wojuola, O. B., Fayemi, O. E., Oyewo, O. A., & Onwudiwe, D. C. (2022). Sol–Gel synthesis and electrochemical sensing properties of brownmillerite calcium Ferrite–$Ca_2Fe_2O_5$ nanoparticles. *Journal of Inorganic and Organometallic Polymers and Materials*, *32*(9), 3445–3458. https://doi.org/10.1007/s10904-022-02397-8

[41] Zhang, F., Liu, Z., Chen, X., Rui, N., Betancourt, L. E., Lin, L., Xu, W., Sun, C., Abeykoon, A. M. M., Rodriguez, J. A., Teržan, J., Lorber, K., Djinović, P., & Senanayake, S. D. (2020). Effects of Zr Doping into Ceria for the Dry Reforming of Methane over Ni/$CeZrO_2$ Catalysts: In Situ Studies with XRD, XAFS, and AP-XPS. *ACS Catalysis*, *10*(5), 3274–3284. https://doi.org/10.1021/acscatal.9b04451

[42] Abbas, H. F., & Daud, W. W. (2009). Hydrogen production by methane decomposition: A review. *International Journal of Hydrogen Energy*, *35*(3), 1160–1190. https://doi.org/10.1016/j.ijhydene.2009.11.036

[43] Alifanti, M., Baps, B., Blangenois, N., Naud, J., Grange, P., & Delmon, B. (2002). Characterization of CeO_2−ZrO_2 mixed oxides. Comparison of the citrate and Sol−Gel preparation methods. *Chemistry of Materials*, *15*(2), 395–403. https://doi.org/10.1021/cm021274j

[44] Pakulska, M. M., Grgicak, C. M., & Giorgi, J. B. (2007). The effect of metal and support particle size on NiO/CeO_2 and NiO/ZrO_2 catalyst activity in complete methane oxidation. *Applied Catalysis A General*, *332*(1), 124–129. https://doi.org/10.1016/j.apcata.2007.08.003

[45] Biesinger, M. C., Payne, B. P., Lau, L. W. M., Gerson, A., & St C Smart, R. (2009). X-ray photoelectron spectroscopic chemical state quantification of mixed nickel metal, oxide and hydroxide systems. *Surface and Interface Analysis*, *41*(4), 324–332. https://doi.org/10.1002/sia.3026

[46] Lambers, E. S., Dykstal, C. N., Seo, J. M., Rowe, J. E., & Holloway, P. H. (1996). Room-temerature oxidation of Ni(110) at low and atmospheric oxygen pressures. *Oxidation of Metals*, *45*(3–4), 301–321. https://doi.org/10.1007/bf01046987

[47] Garcia, X., Soler, L., Vendrell, X., Serrano, I., Herrera, F., Prat, J., Solano, E., Tallarida, M., Llorca, J., & Escudero, C. (2022). Operando NAP-XPS studies of a ceria-supported Pd catalyst for CO oxidation. *Chemistry*, *5*(1), 1–18. https://doi.org/10.3390/chemistry5010001

[48] Wu, Z., Li, M., Howe, J., Meyer, H. M., & Overbury, S. H. (2010). Probing Defect Sites on CeO2 Nanocrystals with Well-Defined Surface Planes by Raman Spectroscopy and O_2 Adsorption. *Langmuir*, *26*(21), 16595–16606. https://doi.org/10.1021/la101723w

[49] Wang, F., He, S., Chen, H., Wang, B., Zheng, L., Wei, M., Evans, D. G., & Duan, X. (2016). Active Site Dependent Reaction Mechanism over Ru/CeO_2 Catalyst toward CO_2 Methanation. *Journal of the American Chemical Society*, *138*(19), 6298–6305. https://doi.org/10.1021/jacs.6b02762

5. Oxygen carrier-catalyst interactions in composite materials for chemical looping steam methane reforming

Abstract

The addition of a CeO_2-supported Ni catalyst to a $Ca_2Fe_2O_5$ (C2F) Oxygen Carrier (OC) has been observed to drastically promote the reactivity of such composite OCs toward CH_4, significantly improving the performances of those materials in Chemical Looping Steam Methane Reforming (CL-SMR) cycles. Nevertheless, the limited stability of the composites is a critical factor hindering their applicability in CL-SMR processes. Here, the development of stable Ni/CeO_2-SiO_2 - $Ca_2Fe_2O_5$ OC materials is reported. The interplay between C2F and the supported catalyst was investigated both in the solid state and in the gas phase. The promotional effect of the Ni catalyst was related to a gas-phase mediated collaborative mechanism established between C2F and the catalyst, that results in a faster OC reduction without affecting the syngas selectivity during the reduction step. The optimal weight ratio between C2F and the catalyst was found to be 10:4. After 50 CL-SMR cycles, the optimized OC was able to obtain a syngas ($CO+H_2$) yield of 13.4 mmol/g during the reduction step and a H_2 yield of 6.6 mmol/g during the oxidation step. The stoichiometry of the process agrees with the oxidation of methane fully mediated by the OC without a degradation of the activity due to the formation of solid carbon. This validates the use of composite materials as rationally designed OCs for the CL-SMR process.

5.1. Introduction

In the previous chapter it was observed how the introduction of Ni as the catalytically active component towards CH_4 activation is beneficial for the reactivity of composite C2F-$Ce_{0.8}Zr_{0.2}O_2$ oxygen carriers. It has been found that the highest reduction kinetics improvement was obtained when Ni was selectively deposited on the $Ce_{0.8}Zr_{0.2}O_2$ (CZ), thus avoiding detrimental chemical interactions between Ni and Fe and exploiting the promotional effect of Ce on the catalytic activity and coking resistance of metallic Ni nanoparticles [1]. Despite this, the sample underwent a rapid decrease in fuel conversion (and in the amount of exchanged lattice oxygen) in the first few CL-SMR cycles. This decrease has been shown to be related to the low stability of the Ni/CZ component when exposed to reaction conditions, which induced a significant loss of surface area and possibly reduced the number of catalytically active sites for CH_4 activation. Following these observations, the present work reports the development of composite $Ca_2Fe_2O_5$ - Ni/modified CeO_2 OCs for the CL-SMR process, prepared by simple physical mixing. The present contribution corroborates previous results, providing further confirmation of the effectiveness of physical mixtures of iron-based OC materials and Ni-based catalysts for enhancing reduction kinetics in CL-SMR cycles in a simple and cost-effective way, minimizing the content of expensive and harmful Ni. Furthermore, it investigates the microstructural evolution of the OC material through *in situ* X-ray diffraction, providing insights on the changes that occur at the solid state. The effect of catalyst introduction on the fuel

conversion, products yield, and selectivity and the stability of such OC materials were evaluated in actual reaction conditions.

5.2. Experimental

The details on samples preparation and characterization methods are reported in chapter 2. Synchrotron x-ray powder diffraction (XPD) experiments were performed at the BL04 beamline (MSPD) at the ALBA synchrotron (Barcelona, Spain). The beamline was operated at 30 keV (wavelength corresponding to 0.4139 Å) in transmission (Debye-Sherrer) mode. Diffraction patterns were acquired every 15 s using the MYTHEIN-II detector, in the 0.55 to 60° 2θ range. The *in situ* XPD investigation during isothermal (800 °C) CL-SMR cycles was conducted on two samples. The first consisted solely of Ni/CeO_2-SiO_2, while the second was a physical mixture of equal amounts (by weight) of Ni/CeO_2-SiO_2 and $Ca_2Fe_2O_5$. The CL-SMR cycles were carried out as follows, with a 2-minute purge between each step: 7-minute reduction in 2.5% CH_4 in He, 6-minute oxidation in 10% CO_2 in He, 3-minute oxidation in 20% O_2 in He. The first sample underwent 5 full cycles. The second sample was subjected to 14 cycles, with the final 4 cycles alternating between CO_2-only or O_2-only and standard cycles. When a single reactant was used to perform the oxidation, the step time was fixed at 7 minutes. Phase quantification was performed on relevant diffraction patterns acquired for the Ni/CeO_2-SiO_2 Sample. The procedure involved the identification of the different phases, followed by their quantitative analysis via application of the full profile Rietveld refinement method with the FullProf Suite software. The following parameters were refined: scale factors for all phases, zero-shift parameter, unit-cell parameters for each phase, half-width parameters.

5.3. Results and discussion

5.3.1. Materials reactivity with CH_4

The reactivity of the single reference components ($Ca_2Fe_2O_5$ and Ni/CeO_2) with CH_4 was investigated performing temperature-controlled reductions with 10% CH_4. Figure 5.1a depicts the molar composition of the outlet gas during $Ca_2Fe_2O_5$ reduction. CH_4 consumption begins at a very slow pace from 750 °C onward, and it becomes appreciable after reaching 800 °C. The main reaction products are H_2 and CO, although the formation of total combustion products (CO_2, H_2O) is observed from 820 °C. During the isothermal step at 870 °C, the sample gradually become depleted of lattice oxygen, and a fast increase in both H_2 and CO yield and selectivity take place. Once reached almost complete conversion, methane pyrolysis become the predominant reaction, which produces a sharp peak in H_2 concentration at the outlet. The reason for this behaviour is the formation of large amounts of metallic iron following C2F reduction, which is known to catalyse hydrocarbons pyrolysis reactions [2]. Following the peak, H_2 production decrease steadily due to solid carbon accumulation over the metallic surfaces, which limits the accessibility of the catalytic sites [3]. Figure 5.1b depicts the reduction of Ni/CeO_2 catalyst. A first sharp CH_4 consumption peak is observed at 437 °C, ascribable to the reduction of at least part of the NiO to metallic Ni [4]. Total combustion products are observed along with H_2 and CO. Following the first peak, methane consumption increases and reaches a maximum at 540 °C. Between 440°C and 520 °C, only H_2 is detected as reaction product, indicating that the CH_4 consumption in this low temperature range is driven by its pyrolysis. From 520 °C onward

some CO is observed along with H_2, indicating an oxygen exchange between the gas and the residual NiO and/or the CeO_2 support, the latter thanks to its well-known oxygen transfer capacity (OTC) [5].

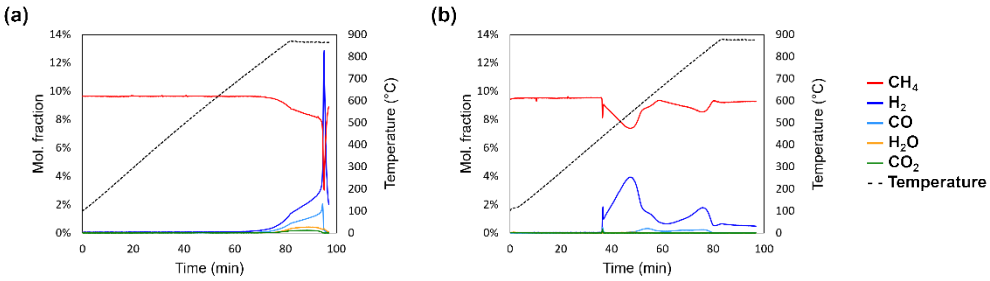

Fig. 5.1. CH_4-TPR of (a) $Ca_2Fe_2O_5$ and (b) Ni/CeO_2.

Isothermal reduction behaviour of C2F and Ni/CeO_2 was investigated performing isothermal CL-SMR cycles at 800 °C. The reduction step duration was set to limit the amount of solid carbon deposited on the samples by CH_4 pyrolysis. Given the different reactivity of the two materials, the duration was set to 45 min and 5.5 min respectively. Figure 5.2a shows the instantaneous CH_4 conversion during the reduction step of C2F. A first consumption peak is observed at the very beginning of the reduction. Successively, the CH_4 conversion increases continuously until the end of the reduction step, suggesting an autocatalytic behaviour of the solid. Fuel conversion does not exceed 18% even after 45 min of exposure to CH_4. It is also observed that the total CH_4 conversion increases over cycles. As visible in figure 5.2b, the reduction of Ni/CeO_2 is much faster, and almost complete CH_4 conversion is obtained at the beginning of the reaction. After 2 minutes, the conversion starts to decrease and reaches 20% at the end of the cycle. Figure 5.2c shows the behaviour of the composite sample obtained by physically mixing equal amounts of C2F and Ni/CeO_2. CH_4 conversion is almost complete in the whole reaction step, indicating that the presence of the catalyst drastically promotes the OC reduction rate. After 5 reduction-oxidation cycles, the composite rapidly lost its initial activity, exhibiting a stable 20% conversion for the entire duration of the step. Figure 5.3 shows the product gases concentration profiles referred to the first reduction step. The reduction of $Ca_2Fe_2O_5$ (figure 5.3a) begins with a short-lived evolution of CO_2 and H_2O, which can be ascribed to the reduction of segregated FeO_x phases or of weakly bound surface oxygen species [6]. Successively, H_2 and CO become the main reaction products, and the syngas selectivity stabilizes to a value of about 81%. The productivity is very low during the entire reaction step. The reduction of Ni/CeO_2 (figure 5.3b) produces initially large volumes of H_2 and CO. Between 2 and 3 minutes, the production of CO starts to decrease, indicating the depletion of the available lattice oxygen, while H_2 production remains high thanks to CH_4 pyrolysis. After three minutes, also H_2 production decrease. This behaviour is likely due to the accumulation of solid carbon produced by CH_4 pyrolysis, which prevents the access of the reactant to the catalytic sites. The C2F-Ni/CeO_2 composite (figure 5.3c), after an initial production peak of CO_2 and H_2O, shows a stable syngas production with a selectivity higher than 90% and a H_2/CO ratio of around 2 until the end of the reaction step.

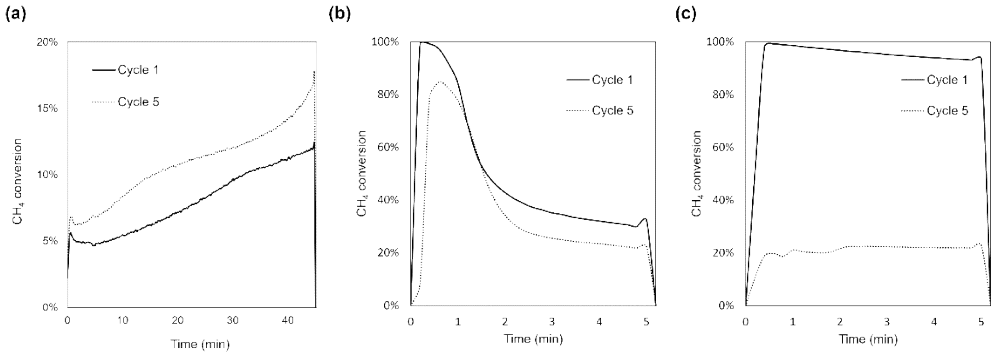

Fig. 5.2. CH_4 conversion profiles during the first and fifth reduction step of CL-SMR cycles conducted with (a) $Ca_2Fe_2O_5$, (b) Ni/CeO_2, (c) a 50:50 (wt.) physical mixture of $Ca_2Fe_2O_5$ and Ni/CeO_2.

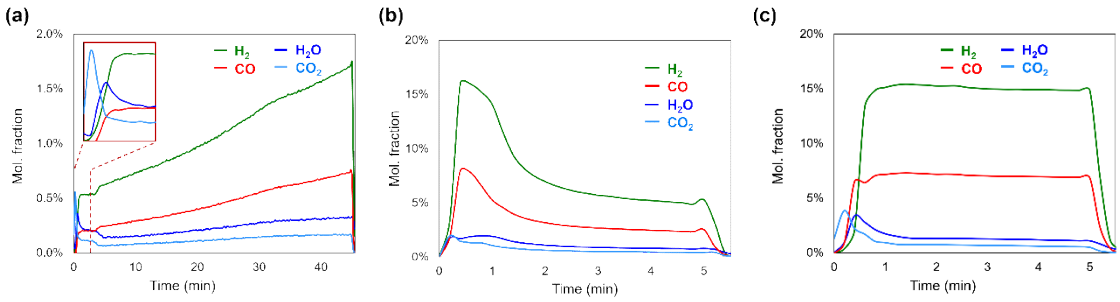

Fig. 5.3. Molar fraction of the reaction products measured at the reactor outlet during the first reduction step of CL-SMR cycles conducted with (a) $Ca_2Fe_2O_5$, (b) Ni/CeO_2, (c) a 50:50 (wt.) physical mixture of $Ca_2Fe_2O_5$ and Ni/CeO_2.

5.3.2. Deactivation of the composite OC material

Results shown in the previous section indicate that the simple physical mixture of C2F and Ni/CeO_2 can effectively enhance both the OC reduction kinetics and the syngas selectivity. Nevertheless, the composite sample experienced a rapid loss of activity upon redox cycling (figure 5.2c). Figure 5.4 shows the x-ray diffractogram of the composite sample before and after 20 CL-SMR cycles. The crystalline structure of the original phases is preserved, although a partial segregation of hematite could be seen at 35.6 °. Following this observation, it is hypothesized that the cause of deactivation could be related to a reduced stability of the Ni/CeO_2 catalyst when put in contact with C2F.

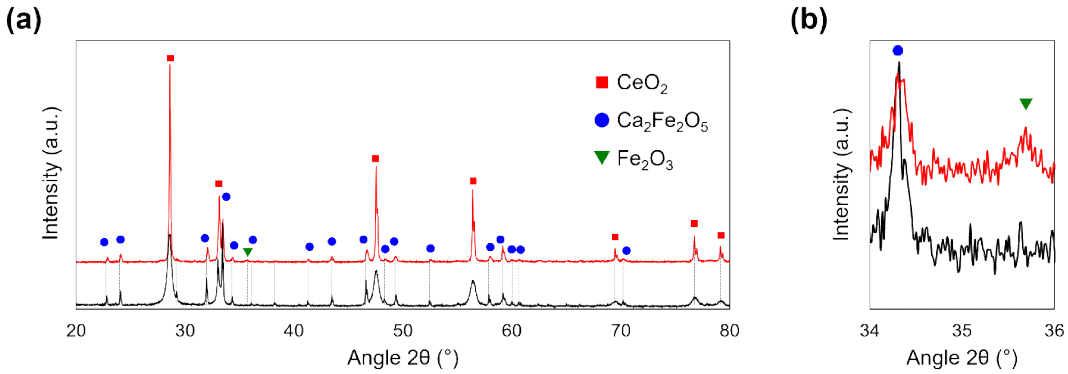

Fig. 5.4. X-ray diffraction profiles of a 50:50 (wt.) physical mixture of $Ca_2Fe_2O_5$ and Ni/CeO_2 before (black curve) and after (red curve) 20 CL-SMR cycles. (■) CeO_2 (PDF card: 01-075-0151). (●) $Ca_2Fe_2O_5$ (PDF card: 00-047-1744). (▼) Fe_2O_3 (PDF card: 01-078-1166).

To evaluate the hypothesis, Al and Si-modified CeO_2 supports (10% mol. Al_2O_3 or SiO_2) were synthesized by coprecipitation to evaluate the effect of the modification with unreducible and thermally stable oxides on the stability of the composite C2F-Ni/CeO_2 samples. The dopants were chosen because of their known ability to improve CeO_2 thermal stability and to facilitate the oxygen vacancies formation and transport [7, 8]. Diffraction profiles of the as-prepared supports are shown in figure 5.5. No significant peak shift of the cubic CeO_2 lattice was observed in the doped materials, suggesting that a complete solid solution between CeO_2 and the dopants may not have been formed, and the latter can be present in an amorphous or poorly crystalline phase [9]. Table 5.1 shows the physical properties of the reference and doped samples calculated from diffraction patterns and N_2 physisorption isotherms.

Tab 5.1. Physical properties of the supports used, as calculated from X-ray diffraction patterns and N_2 physisorption isotherms.

	Main peak position (°)	Average crystallite size from Sherrer eq. (nm)	BET surface area (m^2/g)
CeO_2	28.55	18	60.9
CeO_2-Al_2O_3	28.54	17	23.2
CeO_2-SiO_2	28.54	18	22.6

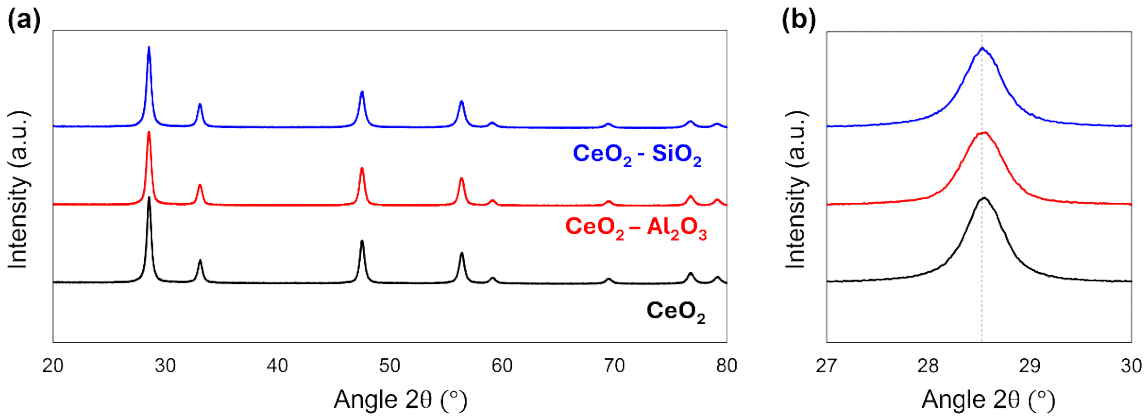

Fig. 5.5. X-ray diffraction profiles of the reference and modified supports in the (a) 20-80 and (b) 27-30 ° 2θ range.

Figure 5.6 shows CH_4 conversion trends of composite samples realized by simple physical mixing of C2F and Ni-loaded CeO_2-Al_2O_3 and CeO_2-SiO_2, compared to the reference C2F-Ni/CeO_2 sample. The Al-modified sample exhibits a similar trend in respect to the reference, with a significant drop in the first 5 redox cycles. On the contrary, the Si-doped sample shows a more stable behaviour, with a slight and gradual loss of activity over cycles. A drastic increase (to 60 nm, +233%) in the support's average crystallite size, calculated from Sherrer equation, is observed after the test for the reference sample. For both the doped samples, a significantly smaller increase was observed, respectively to 34 (+100%) and 32 (+78%) nm for the Al and Si modified CeO_2. This observation is reflected in the evolution of the surface area and pore volume of the samples following the test. For those quantities, the contribution of $Ca_2Fe_2O_5$ is almost negligible, having it a starting surface area of 0.57 m^2/g (measured by Hg porosimetry). As shown in table 5.2, the Ni/CeO_2 – C2F experienced a major loss of both values, while the change was less significative for the other two samples. The least variation was observed for the Ni/CeO_2-SiO_2 – C2F, coherently with the observed CeO_2 particle size increase calculated from XRD.

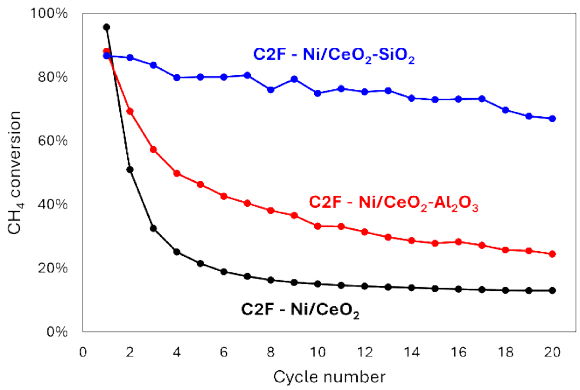

Fig. 5.6. CH_4 conversion of composite OCs realized by physically mixing 50:50 (wt.) of $Ca_2Fe_2O_5$ and Ni-loaded CeO_2 (black curve), CeO_2-Al_2O_3 (red curve) and CeO_2-SiO_2 (blue curve) upon 20 CL-SMR cycles.

Tab. 5.2. Superficial area and pore volume of the samples before and after 50 CL-SMR cycles at 800 °C.

Sample	BET superficial area (m^2/g)		BJH pore volume (mm^3/g)	
	Pristine	After test	Pristine	After test
Ni/CeO_2 – C2F	30	1	231	8
$Ni/Ce_{0.9}Al_{0.1}O_2$ – C2F	11	3	50	23
Ni/CeO2-SiO2 – C2F	15	5	144	91

The effect of the (Si) dopant in limiting the effect of sintering and preserving the morphological features of the support can be observed using Scanning Electron Microscopy (SEM). Figure 5.7 shows SEM micrographs of the Ni/CeO_2 component from the composite C2F-Ni/CeO_2 sample (5.7a) before and (5.6b) after 20 CL-SMR cycles. Figure 5.7c shows the Ni/CeO_2 sample after being tested for 20 CL-SMR cycles without the C2F. The fresh material appears as porous aggregates of very fine particles. The morphology of the cycled material shows remarkable differences. The CeO_2 underwent strong sintering, resulting in a significant restructuring of the crystallites. The transformation of the porous structure can significantly alter the accessibility to the catalytic sites due to pore blockage and Ni nanoparticles encapsulation in the support matrix. Such a severe morphological evolution is not observed when Ni/CeO_2 alone is subjected to CL-SMR cycles, indicating that the co-presence of C2F in the reactive bed enhances the catalyst's degradation. Similarly, figure 5.8 shows images of Ni/CeO_2-SiO_2 before (5.8a) and after 20 cycles with (5.8b) and without (5.8c) being mixed with C2F. Pristine Ni/CeO_2-SiO_2 exhibits a coarser morphology which appears to be preserved even after 20 redox cycles. The co-presence of the C2F in the same reactive bed doesn't significantly affect the microstructural evolution of the support.

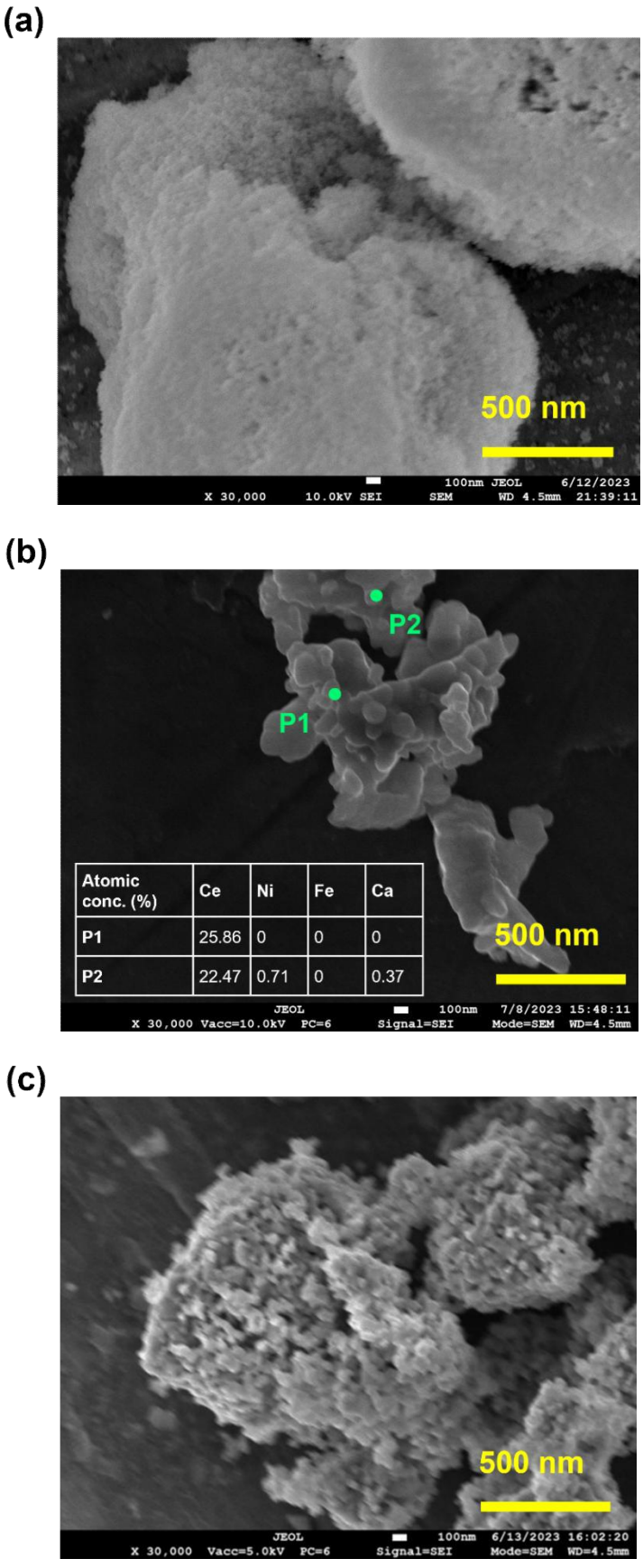

Fig 5.7. SEM images of Ni/CeO_2 particles (a) before and after 20 CL-SMR cycles performed on (b) a 50:50 physical mixture of $Ca_2Fe_2O_5$ and Ni/CeO_2 and (c) on Ni/CeO_2 alone.

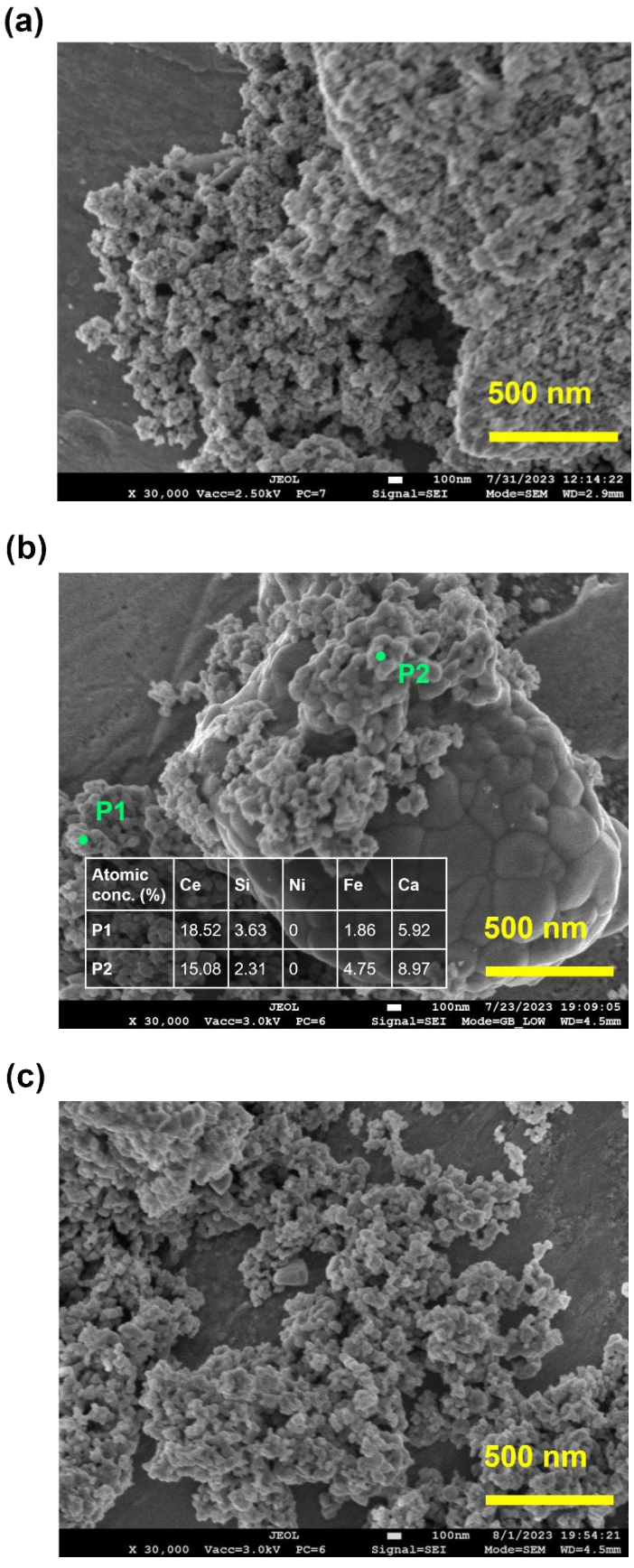

Fig 5.8. SEM images of CeO_2-SiO_2 particles (a) before and after 20 CL-SMR cycles performed on (b) a 50:50 physical mixture of $Ca_2Fe_2O_5$ and Ni/CeO_2-SiO_2 and (c) on Ni/CeO_2-SiO_2 alone.

5.3.3. Solid state interactions between the components

To understand of the solid-state chemistry underlying the Ni/CeO_2-SiO_2 - $Ca_2Fe_2O_5$ system, a series of *in situ* X-ray diffraction analysis has been performed on the prepared OC materials subjected to actual CL-SMR cycles. CO_2 was used as a substitute for H_2O to avoid issues with steam feeding and condensation. The analysis has been carried out for 5 CL-SMR cycles on the sole Ni/CeO_2-SiO_2 and for 10 cycles on a 50:50 physical mixture of Ni/CeO_2-SiO_2 and $Ca_2Fe_2O_5$. For the latter case 4 additional cycles were performed alternating between cycles with CO_2-only or O_2-only oxidation steps and standard cycles, to investigate the effect of the oxidizing agent on the system's dynamics. To qualitatively and quantitatively describe the phase changing phenomena taking place during CL-SMR cycles, two different indicators were used for each component of the OC material. Since CeO_2-based solid solutions are non-stoichiometric compounds, CeO_2-SiO_2 reduction-oxidation process was described by the chemical expansion and contraction of its lattice induced by the generation of defects. In this sense, an increase of the lattice parameter is indicative of the formation of oxygen vacancies and of larger Ce^{3+} ions from Ce^{4+} [10]. The relationship between the d-spacing and the cubic cell parameter is reported in eq. 5.1, where a is the cell parameter and h, k, l the Miller indices.

$$d^2 = \frac{a^2}{(h^2 + k^2 + l^2)} \tag{5.1}$$

Ca, Fe and Ni were found to be present as stable crystalline phase only in $Ca_2Fe_2O_5$, CaO, α-Fe and Fe_3C, and Ni and NiO respectively. Thus, the temporal evolution of these phases was determined evaluating the changes over time of the integrated intensity of a characteristic peak for each phase, which is approximately proportional to the amount present in the sample [11]. The integrated peaks were chosen to avoid overlapping with peaks pertaining to other phases. During the whole test performed on the sole Ni/CeO_2-SiO_2, no other stable crystalline phases else than cubic $Ce_{1-x}Si_xO_2$ and cubic Ni/NiO were observed. It cannot be excluded that part of the SiO_2 exists in an amorphous form. Diffraction patterns *vs.* time collected during the first reduction step are shown in figure 5.9. The reduction process is very fast, taking place in the first 2 minutes. Particularly, the Ni oxide readily reacts with methane to give metallic Ni, which in turn promote the support reduction [12]. The detailed phase change kinetics is shown in figure 5.10.

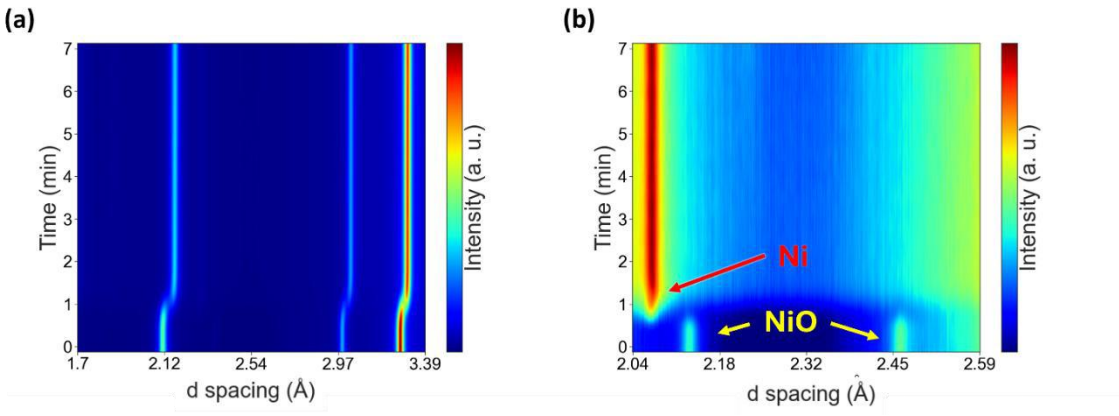

Fig. 5.9. Evolution as a function of time of the Ni/CeO_2-SiO_2 sample during the first reduction step (a) between 1.7 and 3.39 Å and (b) between 2.04 and 2.59 Å.

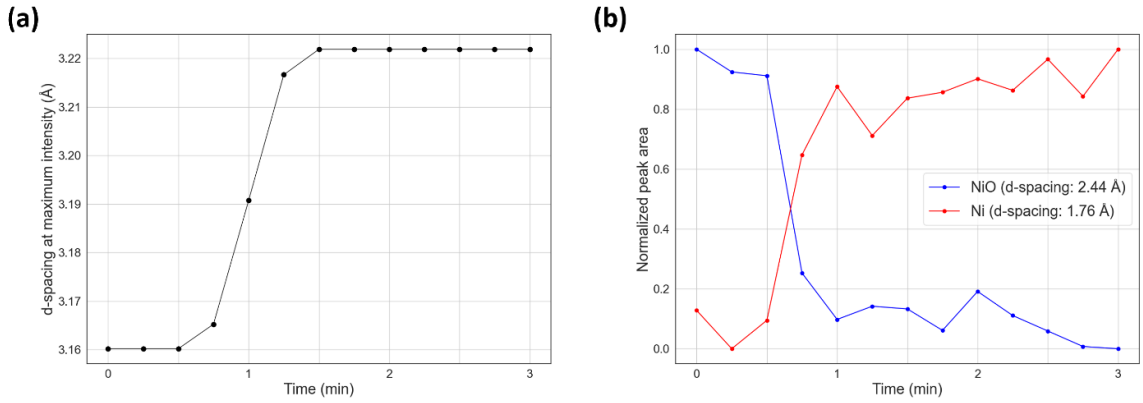

Fig. 5.10. (a) Evolution over time of the d-spacing corresponding to the position of the main $Ce_{1-x}Si_xO_2$ phase peak during the first 3 minutes of the first reduction step. (b) Evolution over time of the area of peaks attributed to NiO (blue) and Ni (red). The areas are expressed as fractions of the maximum value for each phase. Peaks taken as reference for each phase are: 2.44 Å for NiO and 2.76 Å for Ni.

Full profile structure refinement was employed to obtain quantitative data on the crystalline phases present before and after the reduction process (figure 5.11). A significant growth of the average crystallite size of NiO/Ni was observed over cycles (table 5.3), suggesting that the metal particles stability could be the critical factor affecting the durability of the OC material.

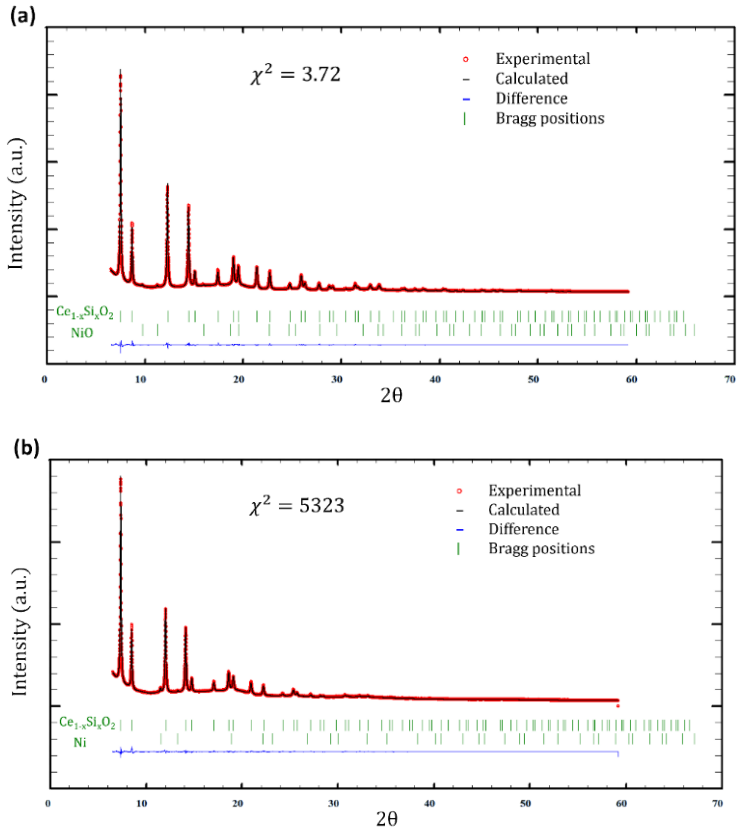

Fig.5.11. X-ray diffraction patterns and full profile refinement (6.5-60° 2θ) of Ni/CeO_2-SiO_2, acquired at 800 °C (a) before and (b) after the first reduction with 2.5% CH_4.

Tab. 3.3. Physical properties of Ni/CeO_2-SiO_2 tested for CL-SMR cycles at 800 °C, calculated by performing Rietveld refinement over the diffraction patterns.

	Before the first reduction		After the first reduction		After the fifth oxidation	
Phase	$Ce_{1-x}Si_xO_2$	NiO	$Ce_{1-x}Si_xO_2$	Ni	$Ce_{1-x}Si_xO_2$	NiO
Space group	F m -3 m	F m -3 m	F m -3 m	F m -3 m	F m -3 m	F m -3 m
Apparent Crystallite size (nm)	20.8	22.1	19.1	80.2	16.0	369.2
Cell parameter (Å)	5.46	4.22	5.76	3.57	5.46	4.22

Reduction-oxidation cycles performed on the composite Ni/CeO_2-SiO_2 - $Ca_2Fe_2O_5$ sample showed that the OC material was able to reversibly cycle between the original (oxidised) composition to oxygen deficient $Ce_{1-x}Si_xO_{2-\delta}$, CaO and Fe (Figure 5.12). The formation of Fe_3C was also observed at the end of the reduction phase, after the consumption of approximately 75% of C2F. An analogous observation was made using pure $Ca_2Fe_2O_5$ as OC in a Fluidized Bed Reactor (FBR) [6]. The formation of the carbide is linked to CH_4 pyrolysis reaction and solid-state carbon diffusion inside the metallic Fe matrix. No carbonate (in particular $CaCO_3$) formation was observed both during the reduction and CO_2 oxidation. Observing the kinetics of the phase evolution (Figure 5.13), is it possible to distinguish two distinct steps in both the reduction and oxidation processes. During the first part of the reduction, a fast lattice expansion of the cubic $Ce_{1-x}Si_xO_2$ lattice is observed. Simultaneously, a comparatively slower decrease of the $Ca_2Fe_2O_5$ content takes place. In the second part (after 4 minutes), a fraction of the metallic Fe previously formed is converted to Fe_3C. At the same time, a significant lattice expansion is observed in the $Ce_{1-x}Si_xO_2$. It is hypothesized that the phenomenon is driven by the local increase of the H_2 partial pressure, due to CH_4 pyrolysis. In the initial stage of oxidation, a gradual decrease in the lattice parameter of $Ce_{1-x}Si_xO_2$ is observed, accompanied by the conversion of Fe_3C to Fe. After the complete consumption of iron carbide, a simultaneous decrease in Fe and CaO occurs, along with the formation of $Ca_2Fe_2O_5$. The fact that the formation of C2F only occurs when all iron has become completely available supports the hypothesis that this is a single-step process, as previously observed in the literature [13]. The reoxidation of the OC material appear complete already after the exposure to 10% CO_2, as expected from thermodynamics and previously reported data [14, 15]. Similar features were observed in the subsequent cycles, indicating a certain stability of the system (figures 5.14 and 5.15).

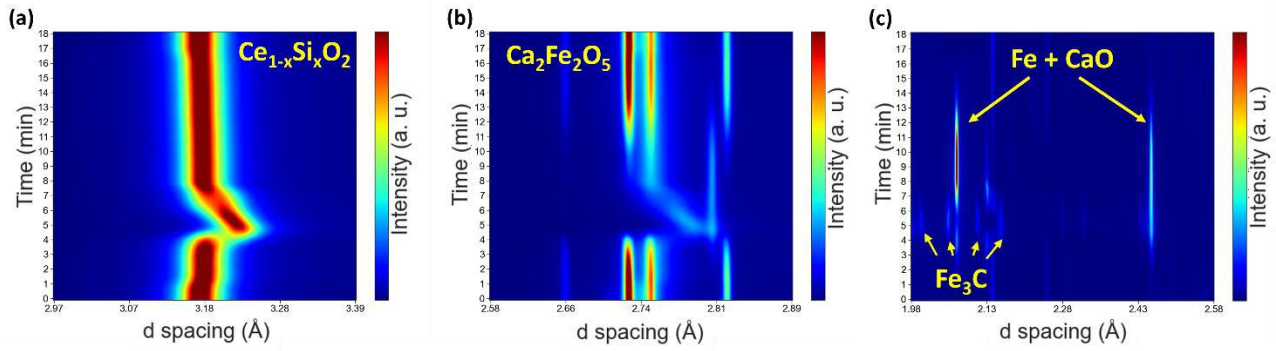

Fig. 5.12. Evolution as a function of time of the main peaks of (a) $Ce_{1-x}Si_xO_2$ (PDF card: 01-075-0076), (b) $Ca_2Fe_2O_5$ (PDF card: 01-071-2264), (c) CaO (PDF card: 01-082-1691) and α-Fe (PDF card: 00-001-1252) during the first CL-SMR cycle undergone by the composite Ni/CeO_2-SiO_2 - $Ca_2Fe_2O_5$ sample. Peaks attributed to the Fe_3C phase (PDF card: 00-034-0001) are pointed out.

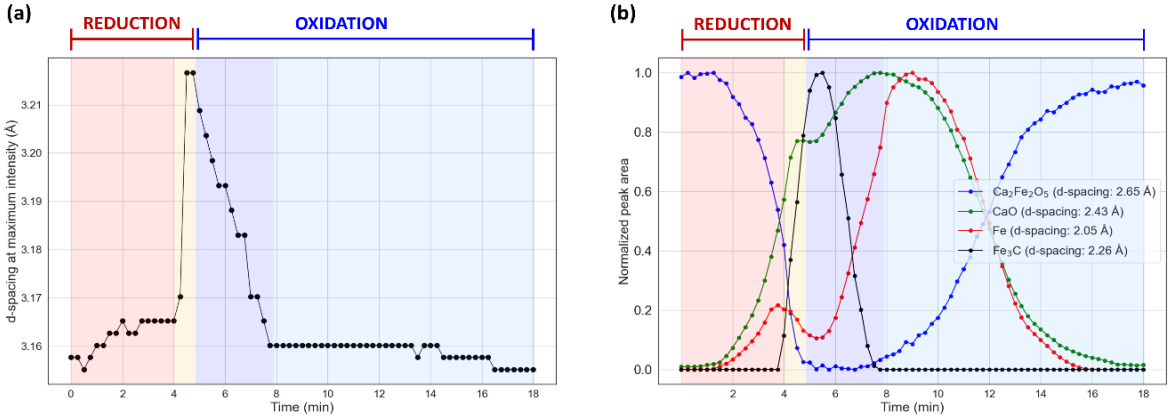

Fig. 5.13. (a) Evolution over time of the d-spacing corresponding to the position of the main $Ce_{1-x}Si_xO_2$ phase peak during the first CL-SMR cycle undergone by the composite Ni/CeO_2-SiO_2 - $Ca_2Fe_2O_5$ sample. (b) Evolution over time of the area of peaks attributed to $Ca_2Fe_2O_5$ (blue), CaO (green), Fe (red), and Fe_3C (black). The areas are expressed as fractions of the maximum value for each phase. Peaks taken as reference for each phase are: 2.65 Å for $Ca_2Fe_2O_5$, 2.44 Å for CaO, 2.06 Å for Fe and 2.26 Å for Fe_3C.

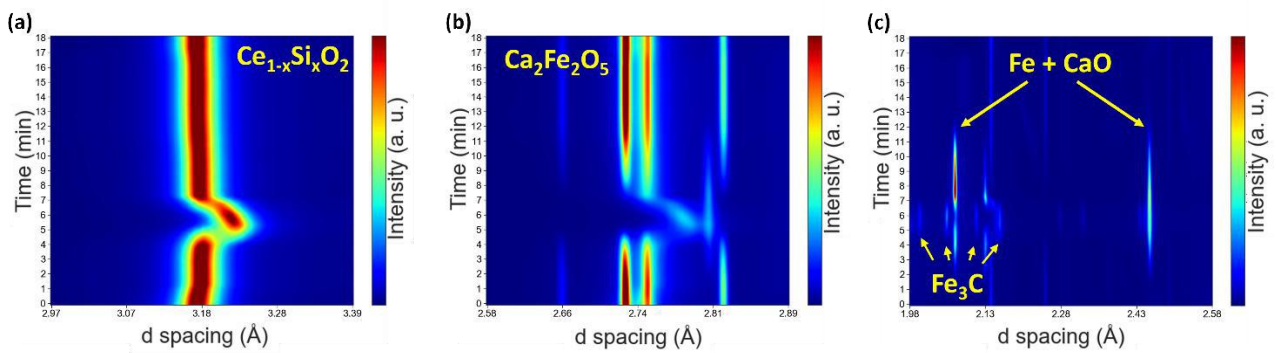

Fig. 5.14. Evolution as a function of time of the main peaks of (a) $Ce_{1-x}Si_xO_2$ (PDF card: 01-075-0076), (b) $Ca_2Fe_2O_5$ (PDF card: 01-071-2264), (c) CaO (PDF card: 01-082-1691) and α-Fe (PDF card: 00-001-1252) during the tenth CL-SMR cycle undergone by the composite Ni/CeO_2-SiO_2 - $Ca_2Fe_2O_5$ sample. Peaks attributed to the Fe_3C phase (PDF card: 00-034-0001) are pointed out.

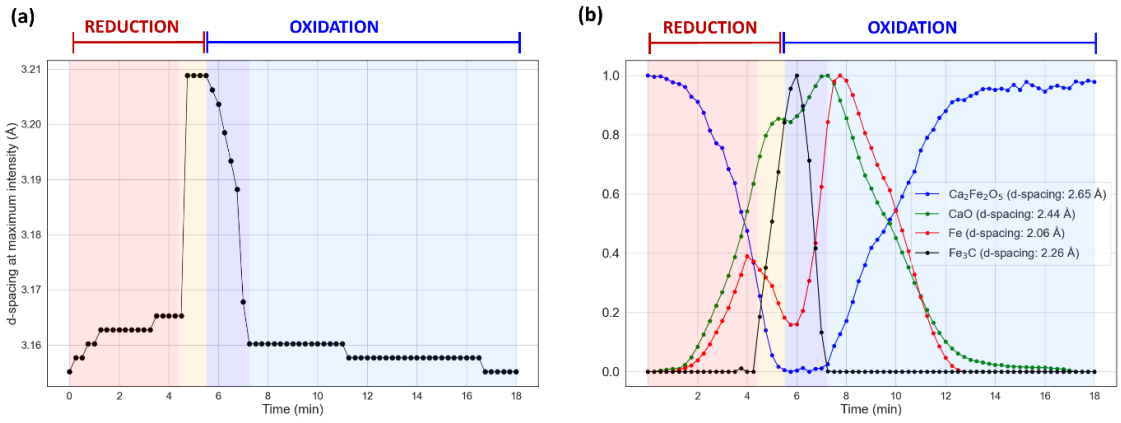

Fig. 5.15. (a) Evolution over time of the d-spacing corresponding to the position of the main $Ce_{1-x}Si_xO_2$ phase peak during the tenth CL-SMR cycle undergone by the composite Ni/CeO_2-SiO_2 - $Ca_2Fe_2O_5$ sample. (b) Evolution over time of the area of peaks attributed to $Ca_2Fe_2O_5$ (blue), CaO (green), Fe (red), and Fe_3C (black). The areas are expressed as fractions of the maximum value for each phase. Peaks taken as reference for each phase are: 2.65 Å for $Ca_2Fe_2O_5$, 2.44 Å for CaO, 2.06 Å for Fe and 2.26 Å for Fe_3C.

Further cycles were performed to assess whether carrying out the oxidation without CO_2 or O_2 could affect the phases generated or induce segregations. Figure 5.16 shows the diffraction patterns of the sample at the end of the oxidation step carried out either with O_2 or CO_2 only. The patterns don't show any noticeable difference. Direct reoxidation of the OC with 20% O_2 (figures 5.17a and 5.17c) led to the disappearance of the Fe_3C phase prior to the reoxidation of $Ce_{1-x}Si_xO_2$, supposedly due to a fast local O_2 consumption related to carbon combustion. Overall, the composite Ni/CeO_2-SiO_2 - $Ca_2Fe_2O_5$ OC material shows a high reversibility under relevant CL-SMR conditions, also displaying a high degree of flexibility in respect of the oxidizing agent. The critical aspect remains perhaps the stability of the Ni nanoparticles on the CeO_2-SiO_2 support, which can significantly affect the activity of the catalyst [16].

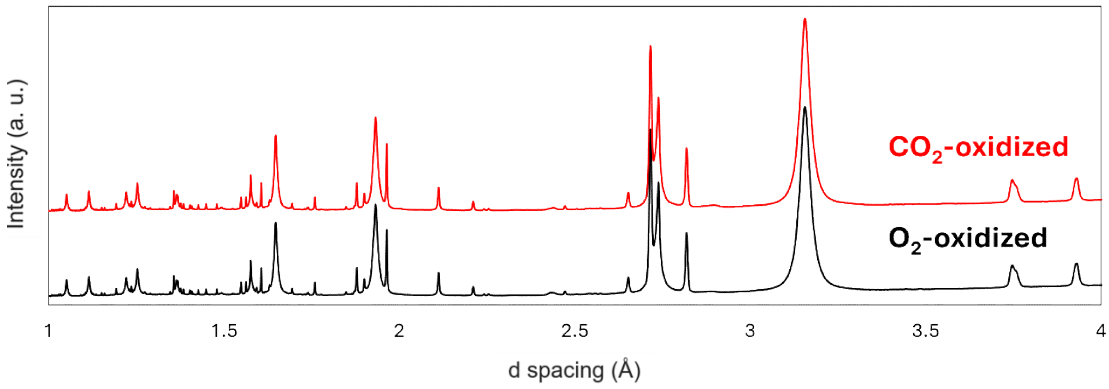

Fig. 5.16. Diffraction patterns of the Ni/CeO_2-SiO_2 - $Ca_2Fe_2O_5$ sample after single-step oxidation with O_2 (black) or CO_2 (red), acquired at 800 °C.

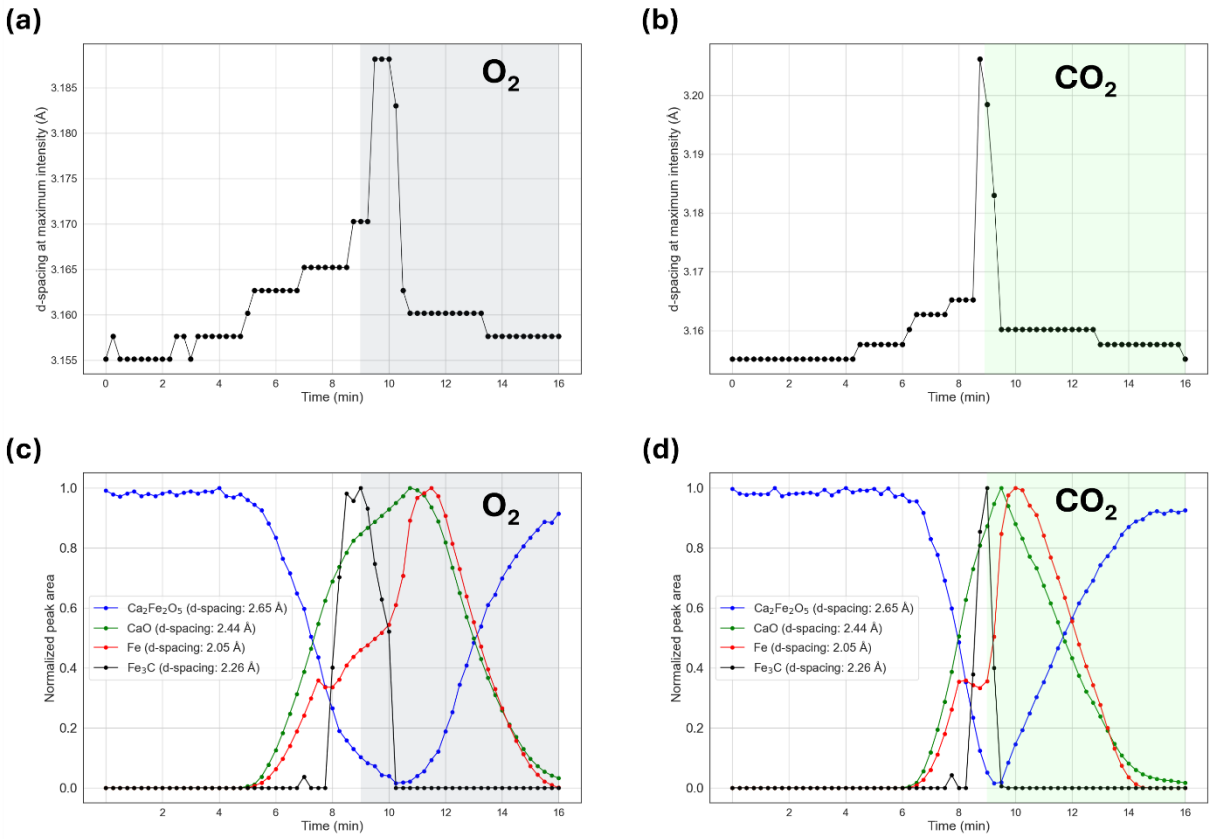

Fig 5.17. (a, b) Evolution over time of the d-spacing corresponding to the position of the main $Ce_{1-x}Si_xO_2$ phase peak during the (a) O_2-oxidation-only and (b) CO_2-oxidation-only cycles undergone by the composite Ni/CeO_2-SiO_2 - $Ca_2Fe_2O_5$ sample. (c, d) Evolution over time of the area of peaks attributed to $Ca_2Fe_2O_5$ (blue), CaO (green), Fe (red), and Fe_3C (black) during the (c) O_2-oxidation-only and (d) CO_2-oxidation-only cycles.

5.3.4. Gas phase interactions between the components

The interplay between C2F and the catalyst was investigated by comparing CL-SMR cycles of the physically mixed OC material (mixed bed configuration, labelled as MB) to a structured reactive bed in which the upstream part of is made by the catalyst alone, followed by a quartz wool plug and a C2F layer (dual bed configuration, labelled as DB), as depicted in figure 5.18.

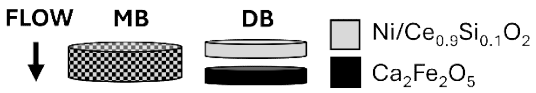

Fig. 5.18. Schematic representation of the mixed and structured reactive bed configurations tested.

As shown in figure 5.19a, the MB configuration exhibited a significantly higher CH_4 conversion during the entire duration of the test. Figure 5.19b reports CH_4 concentration and H_2/CO ratio at the reactor outlet for the two OC bed configurations during the first reduction step. In the structured bed (DB) case, the remarkable formation of solid carbon from CH_4 pyrolysis in the early stages of the reduction (as evidenced by a growth in the H_2/CO ratio) inhibited OC reactivity and limited the oxygen exchange, leading to a lower CH_4 conversion. The co-presence of C2F and the catalyst in the same reactive bed effectively limited the carbon formation at low OC conversion

degrees. In the previous section it was shown how at the solid-state bulk chemical interaction between the C2F and the Ni/ CeO_2-SiO_2 don't take place in the system in reaction conditions. Following this, it is believed that the collaborative behaviour shown by the two materials when placed in close proximity inside the reactive bed is mediated by gaseous intermediates. An explanation for such a behaviour on an analogous system has been proposed in a paper by More and Veser [17]. Briefly, metallic Ni is rapidly formed by the fast reduction of NiO by CH_4. Newly formed metallic Ni catalyse the CH_4 activation, leading to partial oxidation by O^{2-} ions from the CeO_2 in the support [12]. The H_2 and CO thus produced locally promote the reduction of the C2F, which is faster for H_2 and CO than CH_4. The C2F reduction by these gases generate H_2O and CO_2 as products, that can interact with CH_4 giving respectively steam and dry reforming reactions, for both of which metallic Ni is a very active catalyst. Moreover, the presence of a small fraction of oxidizing gases such as H_2O and CO_2 inhibit the deactivation of Ni nanoparticles by accumulation of solid carbon generated by pyrolysis reaction, since at the test conditions those molecules are able to gasify carbonaceous species [18]. This interplay lead to a fast oxygen exchange and to a stable syngas production as long as lattice oxygens in the OC material are available and accessible. In the DB case, in which gas-phase interaction between the two materials is prevented by the layered configuration and the quartz wool plug, the metallic Ni readily catalyse CH_4 pyrolysis, resulting in a rapid loss of activity at the beginning of the reduction step due to active sites blocking by solid carbon. Once the Ni has been deactivated, the C2F itself is no longer able to exchange lattice oxygen at a fast pace due to its scarce ability for CH_4 activation, negatively affecting the fuel conversion.

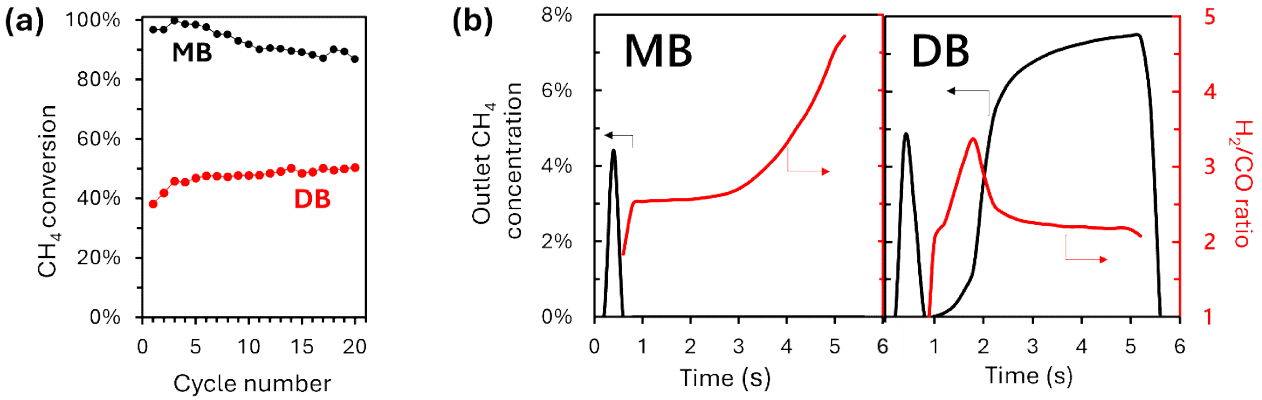

Fig. 5.19 (a) CH_4 conversion during CL-SMR cycles for the MB and DB configurations. (b) Outlet CH_4 concentration and H_2/CO ratio at the reactor outlet during the first reduction step.

The consequences of this behavior are reflected during the oxidation steps. During the steam oxidation step, the amount of H_2 produced by H_2O splitting is proportional to the degree of reduction obtained by the OC material during the previous reduction step. If solid carbon is generated during that step, additional H_2 may be produced by carbon gasification, along with the stoichiometric production of CO that reduce the purity of the H_2 produced. As can be seen from figure 5.20a, the higher fuel conversion of the MB configuration led to a higher H_2 yield. For the MB case, almost all the H_2 produced comes from the replenishment of the OC lattice oxygen (figure 5.20b). The DB sample instead produced a lower amount of H_2 despite a non-negligible contribution from carbon

gasification. Furthermore, not all the deposited carbon could be gasified by steam for the DB sample, meaning that part of it could be removed only by exposure to O_2 at the conditions adopted for the cycles (figure 5.21).

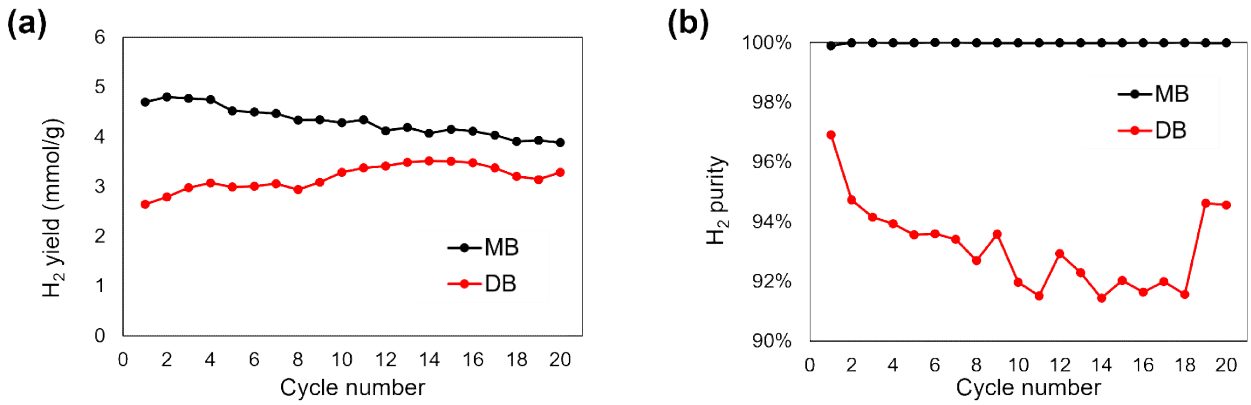

Fig. 3.20. Comparison of H_2 yield (a) and H_2 purity (b) relative to the oxidation step for the MB and DB configurations.

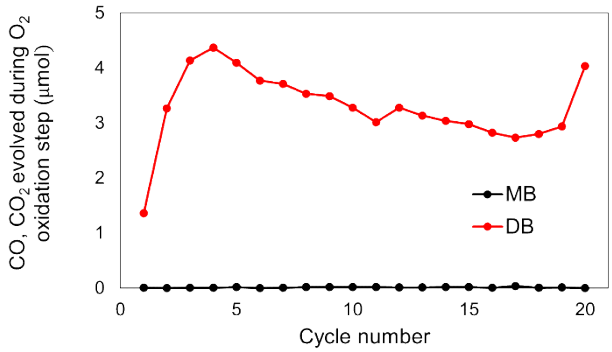

Fig. 3.21. Carbon-containing products evolved during the O_2-oxidation step for the MB and DB configurations.

5.3.5. OC durability

The durability of OCs is a factor of paramount importance for the economical sustainability of all chemical looping processes [19]. To evaluate the ability of the OC material to withstand a large number of reduction-oxidation cycles, samples with a higher Ni loading (2.12% wt. on CeO_2-SiO_2, corresponding to 1.06% wt. on 50:50 Ni/CeO_2-SiO_2 - C2F samples) were prepared and tested for 50 CL-SMR cycles. Additional tests were performed using respectively H_2O and O_2 as the sole oxidant, to evaluate the OC response to the use of a single oxidising agent. The three cases were compared by the fuel conversion and the gas-phase CO selectivity obtained in the reduction step. Results are shown in figure 5.22. In terms of CH_4 conversion, the samples exposed to O_2 exhibited a stable behaviour after 25-30 cycles, settling at 90% and 85% conversion respectively for the standard cycled and the O_2-oxidized only samples. The H_2O-only oxidized sample showed instead a remarkable decrease in the fuel conversion over the cycles, getting to 30% at the 45th cycle. In terms of CO selectivity, at a similar degree of fuel conversion (*i.e.* the first 10 cycles) the best and worst performances are obtained by the H_2O and O_2-only oxidised samples respectively. It has been shown that surface adsorbed oxygen species oxidise preferentially CH_4 to total combustion products [20, 21]. Thus, the way in which the oxidation step is carried out influence the product selectivity of the reduction step by altering the ratio between the different oxygen species exposed to the gaseous environment,

particularly at the beginning of the step. Figure 5.23 reports the gas composition at the reactor outlet during the 10th reduction step for the three cases. It is seen that exposing the sample to O_2 (standard and O_2-only cases) inhibits the reactivity at the very beginning of the step, due to the higher fraction of Ni found in an oxidized state, which decrease the catalytic activity [22]. Moreover, the O_2-only oxidised sample shows a higher selectivity towards H_2O and CO_2, more evidently in the first part of the reduction step. Diffraction patterns (figure 5.24) acquired after the test show notable differences between the three samples. While the sample cycled by the standard procedure shows no evidence of phase segregation, the use of only one oxidizing agent led to the formation of different crystalline phases. In the H_2O-only case, Si-containing compounds are observed, indicating the migration of at least part of the Si from the CeO_2 lattice. Differently, the O_2-only oxidised sample shows a large segregation of CaO and Fe_2O_3, indicating a reduced phase reversibility likely related to the faster oxidation kinetics in respect of the iron migration to form the C2F lattice.

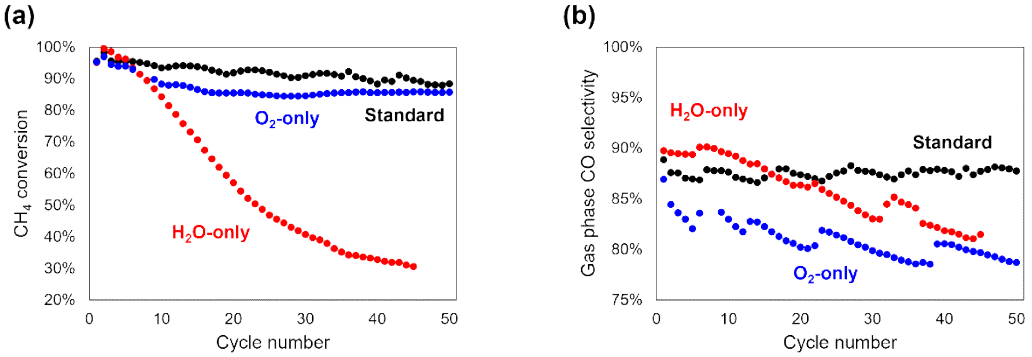

Fig. 5.22. (a) CH_4 conversion and (b) gas phase CO selectivity obtained from Ni/CeO_2-SiO_2 - $Ca_2Fe_2O_5$ samples tested for 50 cycles with subsequent H_2O and O_2 oxidations (standard cycles), H_2O-only and O_2-only cycles.

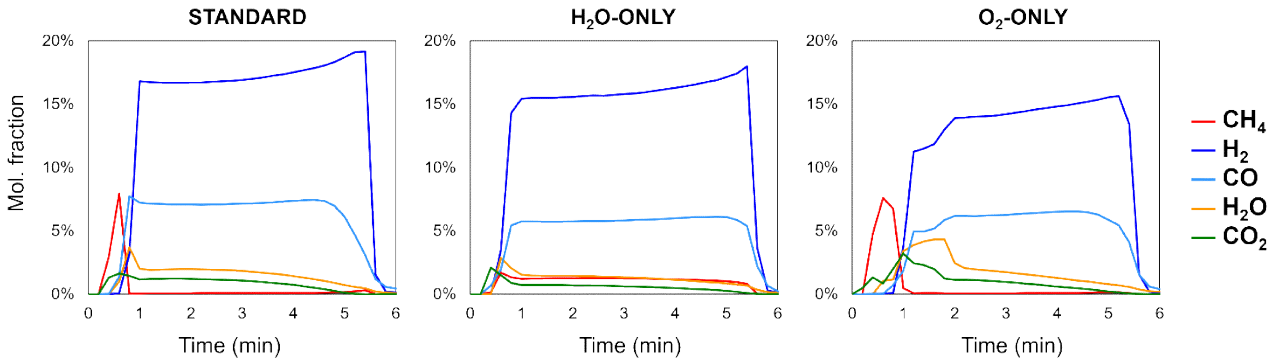

Fig. 5.23. Gas composition (balance He) measured at the reactor outlet during the 10th reduction step of Ni/CeO_2-SiO_2 - $Ca_2Fe_2O_5$ samples tested for 50 cycles with subsequent H_2O and O_2 oxidations (standard cycles), H_2O-only and O_2-only cycles.

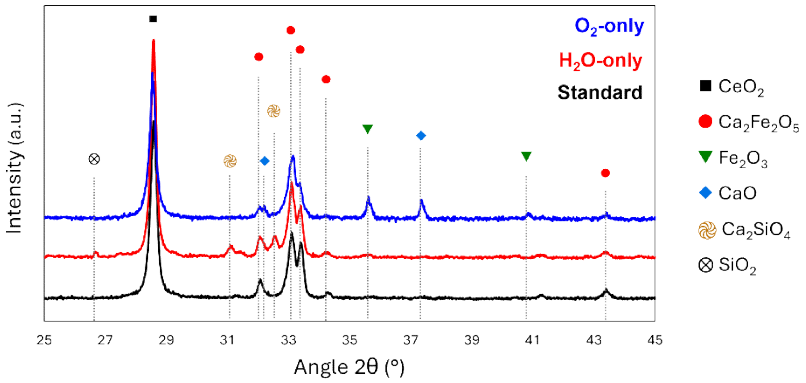

Fig. 5.24. Diffraction patterns of the Ni/CeO_2-SiO_2 - $Ca_2Fe_2O_5$ samples tested for 50 cycles with subsequent H_2O and O_2 oxidations (standard cycles, black curve), H_2O-only (red curve) and O_2-only (blue curve) cycles. (■) CeO_2 (PDF card: 01-075-0151). (●) $Ca_2Fe_2O_5$ (PDF card: 00-047-1744). (▼) Fe_2O_3 (PDF card: 01-078-1166). (◆) CaO (PDF card: 01-078-0649). (֍) Ca_2SiO_4 (PDF card: 01-087-1260). (⊗) Quartz (PDF card: 01-083-0539).

To understand the rapid deactivation of the sample oxidized by H_2O alone in respect of the standard cycled sample, HAADF-STEM images of the samples were acquired prior and after the tests. Although it was not possible to unambiguously identify the crystalline phase by the sole observation of lattice fringes, the analysis (figure 5.25) show that the sample tested for 50 standard CL-SMR cycles (2.25b) does not show a significant crystallite growth in respect of the as prepared OC (2.25a), while a significant degree of sintering is observed after the H_2O-only test (2.25c). For all the samples, EDS maps (figures 5.26-5.28) show homogeneously distributed Ca, Fe, Ce and Si, indicating an intimate contact between the C2F and the Ni/CeO_2-SiO_2. Some discrepancies between the Fe and Ca elemental maps could be observed in the O_2-only oxidized sample, supporting the CaO and Fe_2O_3 segregation observed by X-ray diffraction. Contrarily, Ni appear clustered in some areas, suggesting its presence as individual nanoparticles. The Ni domains in the tested samples appear bigger than the pristine sample, nevertheless the size increase appears to be more than double in the H_2O-only case (figure 5.28) in respect of the standard cycled sample (figure 5.27). In addition to that, in the H_2O-only cycled sample a common occurrence of Ni and Fe can be observed in some spots. From this, it is inferred that the exposure to O_2 contributes to counteract Ni sintering through its redispersion induced by cyclical reduction-oxidation [23].

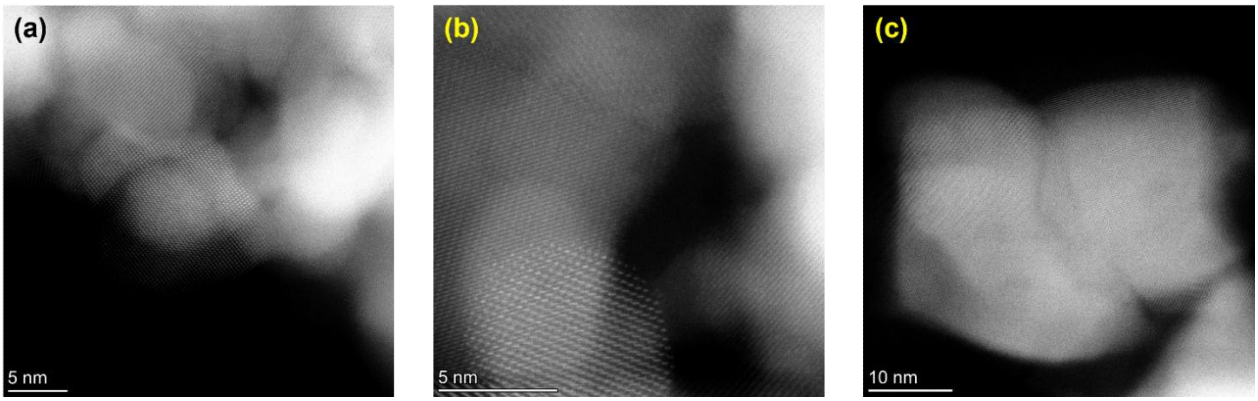

Fig. 5.25. HAADF-STEM images acquired on the (a) pristine, (b) tested for 50 standard CL-SMR cycles and (c) tested for 45 H_2O-only cycles Ni/CeO_2-SiO_2 - $Ca_2Fe_2O_5$ sample.

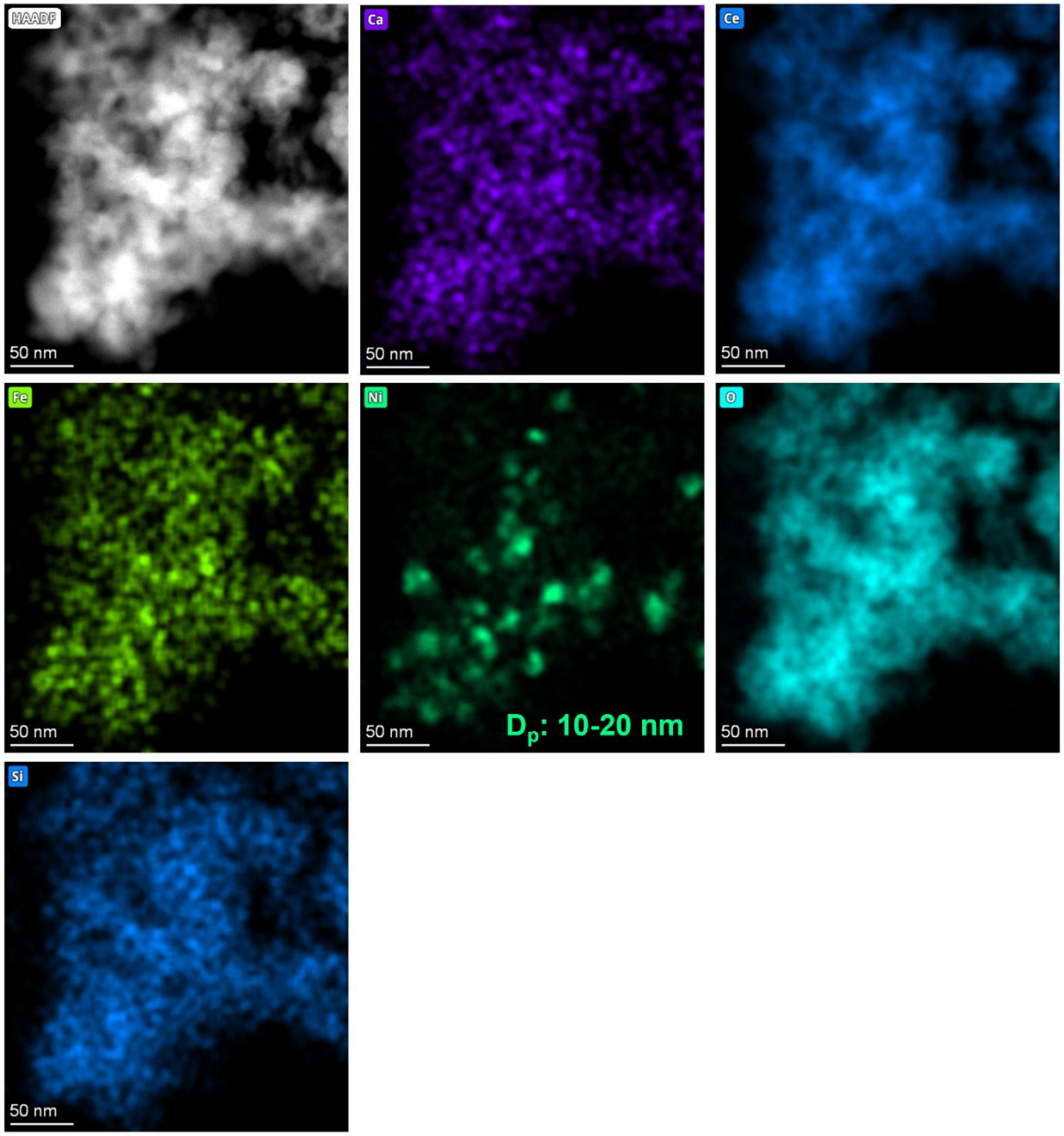

Fig. 5.26. EDS maps and the corresponding HAADF-STEM images acquired on the as-prepared Ni/CeO_2-SiO_2 - $Ca_2Fe_2O_5$ sample. Ni particle size, as inferred from the EDS map, is reported in the corresponding square.

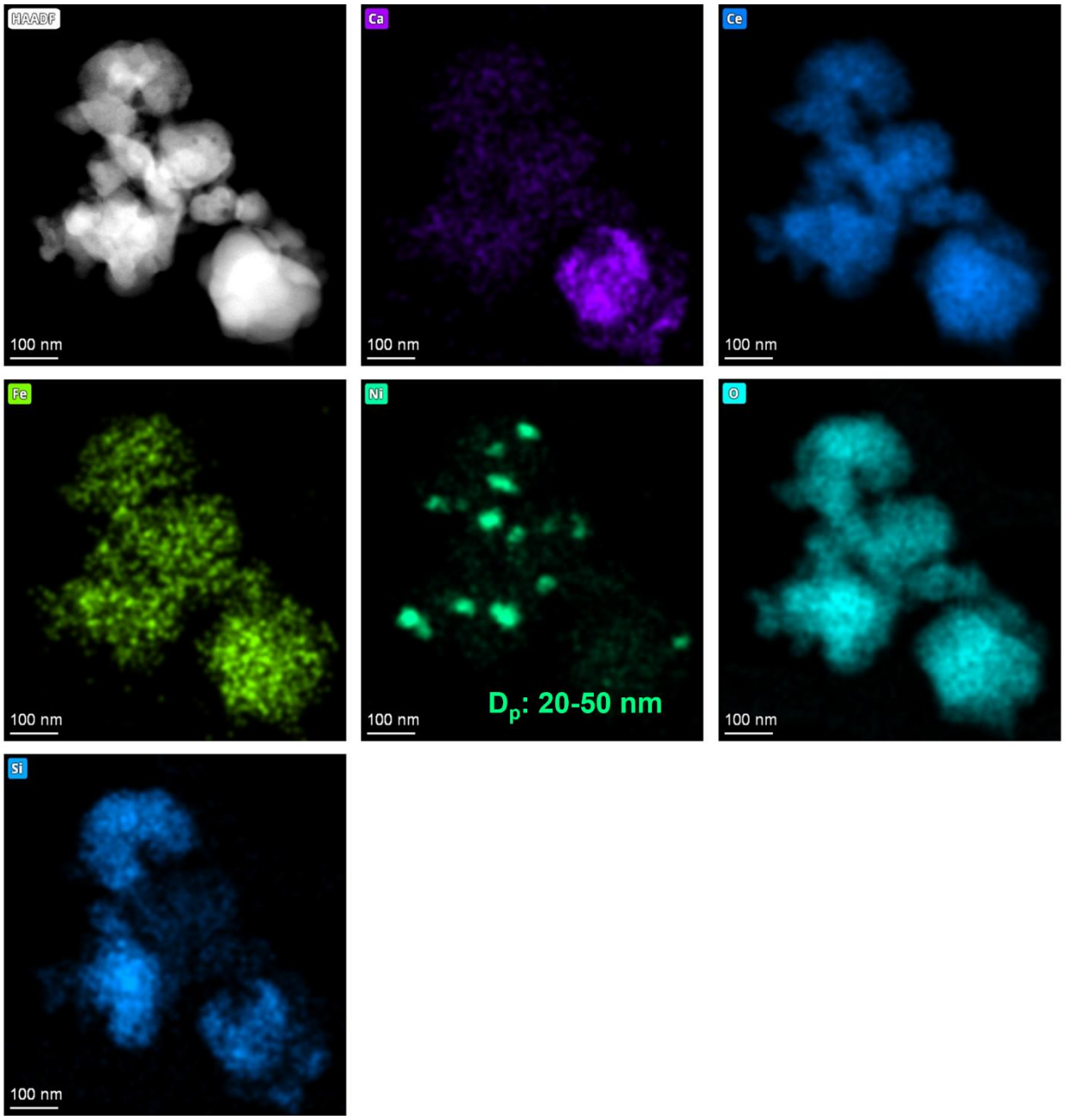

Fig 5.27. EDS maps and the corresponding HAADF-STEM images acquired on the Ni/CeO_2-SiO_2 - $Ca_2Fe_2O_5$ sample tested for 50 standard CL-SMR cycles. Ni particle size, as inferred from the EDS map, is reported in the corresponding square.

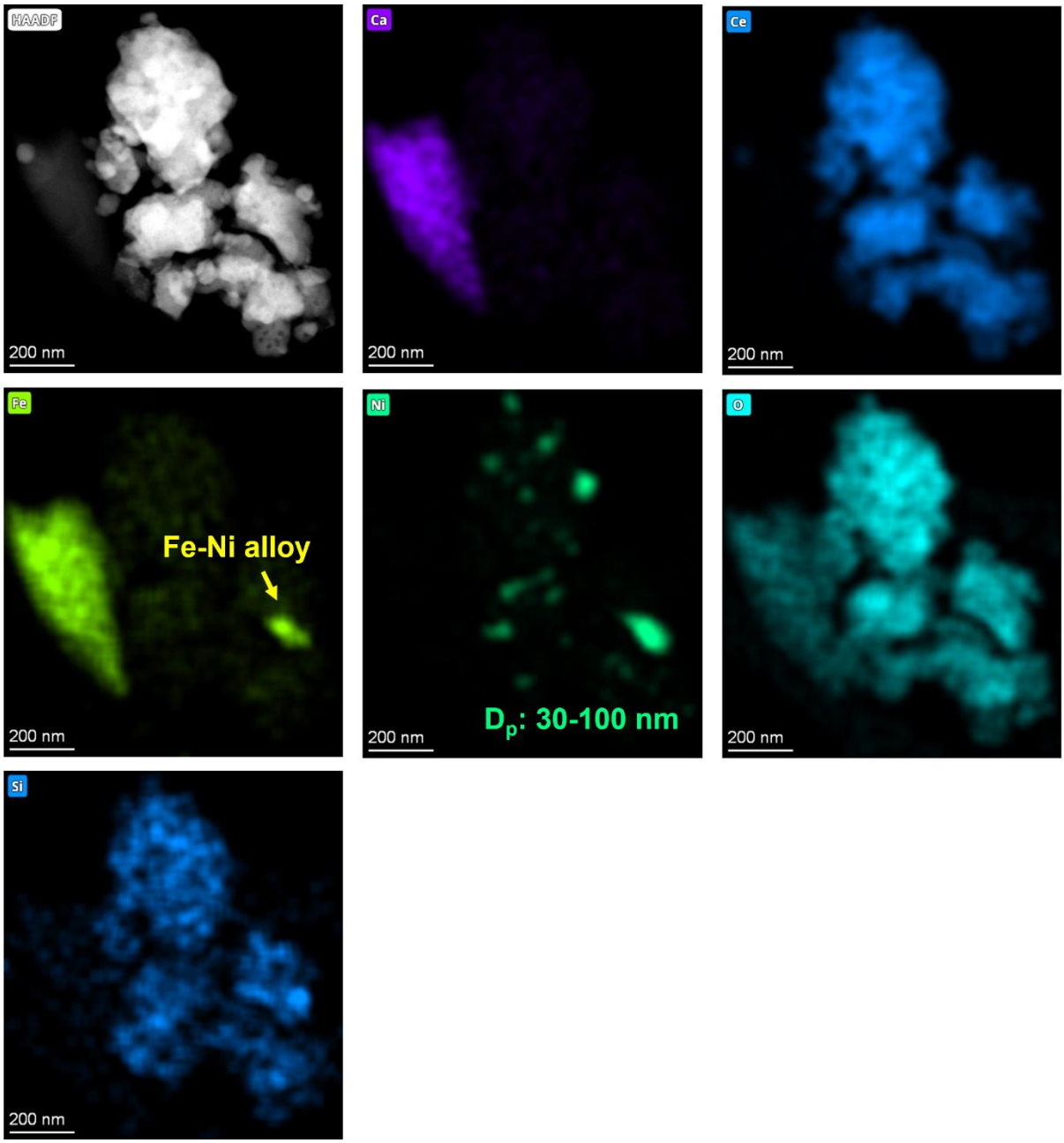

Fig 5.28. EDS maps and the corresponding HAADF-STEM images acquired on the Ni/CeO_2-SiO_2 - $Ca_2Fe_2O_5$ sample tested for 45 H_2O-only cycles. Ni particle size, as inferred from the EDS map, is reported in the corresponding square.

5.3.6. Optimization of the composition

The effect of the OC/catalyst ratio on the OTC of the composite was investigated performing CL-SMR tests on samples obtained by physically mixing a constant amount of C2F (100 mg) and a variable amount of catalyst (20-100 mg). This choice was made given the larger OTC of C2F in respect of that of Ni/CeO_2-SiO_2. As for the durability experiments, for these tests the Ni/CeO_2-SiO_2 catalyst with a 2.12% wt. Ni loading was used. The samples were compared in terms of the products yields obtained during both the reduction (H_2 and CO) and the H_2O-oxidation (H_2) steps. Table 5.5 summarizes the tested compositions.

Tab. 5.5. Composition of the samples with variable Ni/CeO_2-SiO_2 content (Ni loading: 2.12% wt.).

ID	C2F weight (mg)	Ni/CeO_2-SiO_2 weight (mg)
C2F10cat2	100	20
C2F10cat4	100	40
C2F10cat6	100	60
C2F10cat8	100	80
C2F10cat10	100	100

Figure 5.29 shows that the specific syngas and hydrogen productivity in the initial phase were inversely proportional to the amount of catalyst used. This confirms that the OTC of the composite is primarily provided by C2F. Nevertheless, the increase of the catalyst amount contributed to a more stable behaviour of the composites. At the 10th cycle, the highest specific syngas and H_2 yields are obtained with the C2F10cat4 sample, which take advantage of a low catalyst amount and an acceptable stability in 10 CL-SMR cycles.

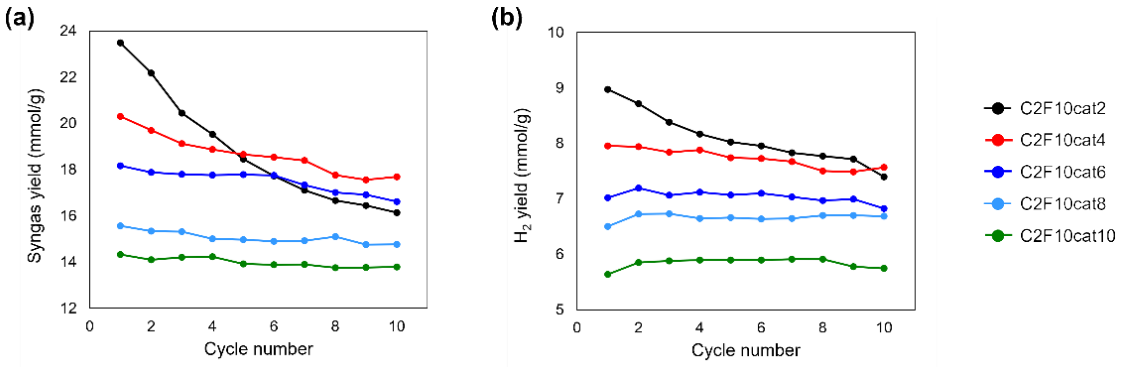

Fig. 5.29. Cyclic performance of physical mixtures of $Ca_2Fe_2O_5$ and Ni/CeO_2-SiO_2 with different weight ratios in 10 CL-SMR cycles. (a) Specific syngas yield in the reduction step. (b) Specific H_2 yield in the steam oxidation step.

The optimal composition C2F10cat4 was tested for 50 CL-SMR cycles to further assess its stability. Results are shown in figure 3.30. A decrease in the fuel conversion of about 30% was observed during the first 35 cycles, that led to a slight reduction of the syngas and H_2 yields with the cycles. The loss of activity was accompanied by a reduction of the amount of solid carbon deposited during the first stages of reduction, which led to high H_2 purity during the steam oxidation step from the first 10th cycle onward. Stable syngas and H_2 production were obtained after 35 redox cycles, producing at the 50th cycle 13.4 mmol/g of syngas in the reduction step with 66.6% CH4 conversion, and 6.6 mmol/g of H_2 in the steam oxidation step with 99.9% purity. These values are promising and comparable or superior to those reported in the open literature for other OC systems, as shown in table 5.6.

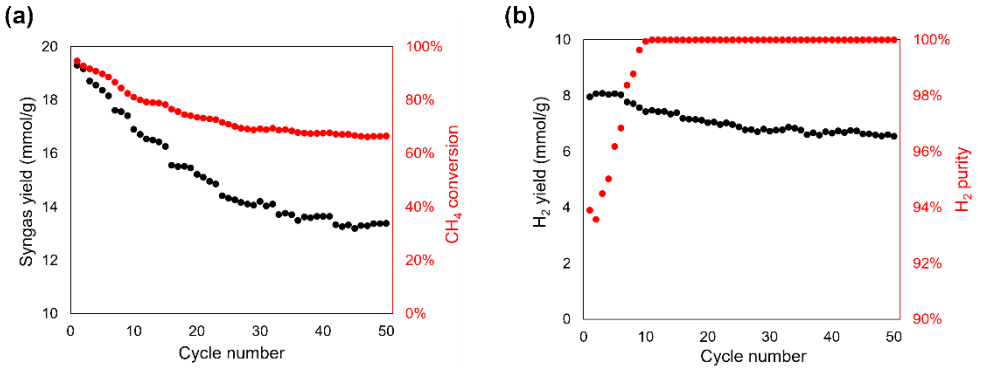

Fig. 5.30. Cyclic performance of a 10:4 (wt.) physical mixture of $Ca_2Fe_2O_5$ and 2.12 % wt. Ni/CeO_2-SiO_2 in 50 CL-SMR cycles. (a) syngas yield and CH_4 conversion in the reduction step. (b) H_2 yield and purity in the steam oxidation step.

Tab. 5.6. Selected studies on CL-SMR from literature along with the present work, adapted from [24].

Oxygen carrier	Temp. (°C)	syngas yield (mmol/g)	CH_4 conv. (%)	H_2 yield (mmol/g)	H_2 purity (%)	Number of cycles	Ref.
$Ca_2Fe_2O_5$ - Ni/CeO_2-SiO_2	**800**	**13.4**	**66.6%**	**6.6**	**99.9**	**50**	**This work**
$CuFe_2O_4$	900	9.3	54.5	11.3	>99	5	[25]
3DOM $LaFe_{0.9}Ni_{0.1}O_3$	850	-	95	6.39	84.3	10	[26]
$La_{1.6}Sr_{0.4}FeCoO_6$	850	10.25	90	5.9	-	20	[27]
$BaCoO_3/CeO_2$	860	11.84	-	3.9	94.3	25	[28]
$Ce_{0.5}Fe_{0.5}O_{2-\delta}$	850	7.94	51	3.72	>99	10	[29]
10% CeO_2/3DOM $LaFeO_3$	800	9.94	-	3.38	>99	30	[30]
$Ce_{0.8}Zr_{0.2}O_2$	800	-	55.89	1.88	-	10	[31]

5.4. Conclusions

The promotional effect of selectively introducing Ni onto a Ce-based support in composite C2F-Ni/CeO_2 OC materials for CL-SMR has been thoroughly investigated. A stable and active OC material was obtained by simple physical mixing of C2F and Ni-loaded CeO_2-SiO_2 powders. The silica-modification of CeO_2 has been shown to improve the active support morphological stability. *In situ* X-ray diffraction revealed that C2F and Ni/CeO_2-SiO_2 do not interact to form new crystalline phases, instead their reactivity could influence each other's by altering the local gaseous environment through chemical reactions. The analysis also individuated Ni particles sintering as a potential criticality for the long-term stability of the OC material. It was found that exposing the OC to O_2 after the steam oxidation step of CL-SMR cycles could significantly improve the OC stability by inhibiting Ni

nanoparticles growth and preventing the formation of undesired segregated phases, such as Fe-Ni mixed oxides and $CaSiO_4$.

The interplay between the two components was investigated by performing CL-SMR cycles in a microreactor. Interestingly, the co-presence of C2F and Ni/CeO_2-SiO_2 in the same reactive bed was found to inhibit deactivation by coking and to accelerate the oxygen exchange between the solid and the gaseous environment. An optimal composition for the maximization of product selectivity and yields was identified, corresponding to a Ni/CeO_2-SiO_2 to C2F weight ratio of 0.4. The optimized composition was tested for 50 CL-SMR cycles, showing an acceptable stability and performances comparable or superior to other OC systems reported in the open literature.

5.5. References

[1] Pantaleo, G., La Parola, V., Deganello, F., Singha, R., Bal, R., & Venezia, A. (2016). Ni/CeO_2 catalysts for methane partial oxidation: Synthesis driven structural and catalytic effects. Applied Catalysis B Environment and Energy, 189, 233–241. https://doi.org/10.1016/j.apcatb.2016.02.064

[2] Abbas, H. F., & Daud, W. W. (2009b). Hydrogen production by methane decomposition: A review. *International Journal of Hydrogen Energy*, *35*(3), 1160–1190. https://doi.org/10.1016/j.ijhydene.2009.11.036

[3] Koshi, M., Uehara, T., & Asahara, M. (2024). Problems in the reaction mechanism of methane pyrolysis for hydrogen production. *International Journal of Hydrogen Energy*, *72*, 850–860. https://doi.org/10.1016/j.ijhydene.2024.05.305

[4] Chen, J., Buchanan, T., Walker, E. A., Toops, T. J., Li, Z., Kunal, P., & Kyriakidou, E. A. (2021). Mechanistic understanding of methane combustion over Ni/CeO_2: A Combined Experimental and Theoretical Approach. ACS Catalysis, 11(15), 9345–9354. https://doi.org/10.1021/acscatal.1c01088

[5] Trovarelli, A. (1996). Catalytic properties of ceria and CeO_2-Containing materials. *Catalysis Reviews*, *38*(4), 439–520. https://doi.org/10.1080/01614949608006464

[6] Sukma, M. S., Zheng, Y., Hodgson, P., & Scott, S. A. (2022c). Understanding the behavior of dicalcium ferrite ($Ca_2Fe_2O_5$) in chemical looping syngas production from CH_4. *Energy & Fuels*, *36*(17), 9410–9422. https://doi.org/10.1021/acs.energyfuels.2c01065

[7] Pijolat, M., Prin, M., Soustelle, M., Touret, O., & Nortier, P. (1995). Thermal stability of doped ceria: experiment and modelling. *Journal of the Chemical Society Faraday Transactions*, *91*(21), 3941. https://doi.org/10.1039/ft9959103941

[8] Rocchini, E., Trovarelli, A., Llorca, J., Graham, G. W., Weber, W. H., Maciejewski, M., & Baiker, A. (2000). Relationships between Structural/Morphological Modifications and Oxygen Storage–Redox Behavior of Silica-Doped Ceria. *Journal of Catalysis*, *194*(2), 461–478. https://doi.org/10.1006/jcat.2000.2954

[9] Wang, J., Li, Z., Zhang, S., Yan, S., Cao, B., Wang, Z., & Fu, Y. (2017). Enhanced NH3 gas-sensing performance of silica modified CeO_2 nanostructure-based sensors. *Sensors and Actuators B Chemical*, *255*, 862–870. https://doi.org/10.1016/j.snb.2017.08.149

[10] Marrocchelli, D., Bishop, S. R., Tuller, H. L., & Yildiz, B. (2012). Understanding Chemical expansion in Non-Stoichiometric Oxides: Ceria and Zirconia case studies. *Advanced Functional Materials*, *22*(9), 1958–1965. https://doi.org/10.1002/adfm.201102648

[11] Cullity, B. D., & Stock, S. R. (2001). Elements of x-ray diffraction, Prentice Hall. Upper Saddle River, NJ, 388.

[12] Han, Y., Tian, M., Wang, C., Kang, Y., Kang, L., Su, Y., Huang, C., Zong, T., Lin, J., Hou, B., Pan, X., & Wang, X. (2021b). Highly Active and Anticoke Ni/CeO_2 with Ultralow Ni Loading in Chemical Looping Dry Reforming via the Strong Metal–Support Interaction. *ACS Sustainable Chemistry & Engineering*, *9*(51), 17276–17288. https://doi.org/10.1021/acssuschemeng.1c06079

[13] Miller, D. D., Riley, J., & Siriwardane, R. (2019c). Interaction of Methane with Calcium Ferrite in the Chemical Looping Partial Oxidation Application: Experimental and DFT Study. *Energy & Fuels*, *34*(2), 2193–2204. https://doi.org/10.1021/acs.energyfuels.9b03623

[14] Löfberg, A., Guerrero-Caballero, J., Kane, T., Rubbens, A., & Jalowiecki-Duhamel, L. (2017c). Ni/CeO_2 based catalysts as oxygen vectors for the chemical looping dry reforming of methane for syngas production. *Applied Catalysis B Environment and Energy*, *212*, 159–174. https://doi.org/10.1016/j.apcatb.2017.04.048

[15] Shah, V., Cheng, Z., Baser, D. S., Fan, J. A., & Fan, L. (2020b). Highly Selective Production of Syngas from Chemical Looping Reforming of Methane with CO_2 Utilization on MgO-supported Calcium Ferrite Redox Materials. *Applied Energy*, *282*, 116111. https://doi.org/10.1016/j.apenergy.2020.116111

[16] Prasad, D. H., Ji, H., Kim, H., Son, J., Kim, B., Lee, H., & Lee, J. (2010). Effect of nickel nano-particle sintering on methane reforming activity of Ni-CGO cermet anodes for internal steam reforming SOFCs.

Applied Catalysis B Environment and Energy, *101*(3–4), 531–539. https://doi.org/10.1016/j.apcatb.2010.10.026

[17] More, A., & Veser, G. (2016c). Physical mixtures as simple and efficient alternative to alloy carriers in chemical looping processes. *AIChE Journal*, *63*(1), 51–59. https://doi.org/10.1002/aic.15380

[18] Tamai, Y., Watanabe, H., & Tomita, A. (1977). Catalytic gasification of carbon with steam, carbon dioxide and hydrogen. *Carbon*, *15*(2), 103–106. https://doi.org/10.1016/0008-6223(77)90024-0

[19] Di Giuliano, A., Capone, S., Anatone, M., & Gallucci, K. (2022). Chemical Looping Combustion and Gasification: a review and a focus on European research projects. *Industrial & Engineering Chemistry Research*, *61*(39), 14403–14432. https://doi.org/10.1021/acs.iecr.2c02677

[20] Chang, H., Bjørgum, E., Mihai, O., Yang, J., Lein, H. L., Grande, T., Raaen, S., Zhu, Y., Holmen, A., & Chen, D. (2020b). Effects of oxygen mobility in La–Fe-Based perovskites on the catalytic activity and selectivity of methane oxidation. *ACS Catalysis*, *10*(6), 3707–3719. https://doi.org/10.1021/acscatal.9b05154

[21] Yao, X., Zhang, X., Liu, R., Pei, C., Zhao, Z., & Gong, J. (2023). Oxygen activity regulation over $LaNiO_3$ perovskites by Ti substitution for chemical looping partial oxidation of methane. *Chemical Engineering Science*, *278*, 118911. https://doi.org/10.1016/j.ces.2023.118911

[22] Wu, C., Xiao, Z., Wang, L., Li, G., Zhang, X., & Wang, L. (2021d). Modulating oxidation state of Ni/CeO_2 catalyst for steam methane reforming: a theoretical prediction with experimental verification. *Catalysis Science & Technology*, *11*(5), 1965–1973. https://doi.org/10.1039/d0cy02197k

[23] Kwon, O., Foucher, A. C., Huang, R., Stach, E. A., Vohs, J. M., & Gorte, R. J. (2022). Evidence for redispersion of Ni on $LaMnO_3$ films following high-temperature oxidation. *Journal of Catalysis*, *407*, 213–220. https://doi.org/10.1016/j.jcat.2022.01.036

[24] Das, S., Biswas, A., Tiwary, C., & Paliwal, M. (2022b). Hydrogen production using chemical looping technology: A review with emphasis on H2 yield of various oxygen carriers. *International Journal of Hydrogen Energy*, *47*(66), 28322–28352. https://doi.org/10.1016/j.ijhydene.2022.06.170

[25] Kang, K., Kim, C., Cho, W., Bae, K., Woo, S., & Park, C. (2008). Reduction characteristics of $CuFe_2O_4$ and Fe_3O_4 by methane; $CuFe_2O_4$ as an oxidant for two-step thermochemical methane reforming. *International Journal of Hydrogen Energy*, *33*(17), 4560–4568. https://doi.org/10.1016/j.ijhydene.2008.05.054

[26] Shen, Y., Zhao, K., He, F., & Li, H. (2018). The structure-reactivity relationships of using three-dimensionally ordered macroporous $LaFe_{1-x}Ni_xO_3$ perovskites for chemical-looping steam methane reforming. *Journal of the Energy Institute*, *92*(2), 239–246. https://doi.org/10.1016/j.joei.2018.01.012

[27] Zhao, K., Li, L., Zheng, A., Huang, Z., He, F., Shen, Y., Wei, G., Li, H., & Zhao, Z. (2017). Synergistic improvements in stability and performance of the double perovskite-type oxides $La_{2-x}Sr_xFeCoO_6$ for chemical looping steam methane reforming. *Applied Energy*, *197*, 393–404. https://doi.org/10.1016/j.apenergy.2017.04.049

[28] Ding, H., Xu, Y., Luo, C., Wang, Q., Shen, C., Xu, J., & Zhang, L. (2018). A novel composite perovskite-based material for chemical-looping steam methane reforming to hydrogen and syngas. *Energy Conversion and Management*, *171*, 12–19. https://doi.org/10.1016/j.enconman.2018.05.088

[29] Zhu, X., Wei, Y., Wang, H., & Li, K. (2013). Ce–Fe oxygen carriers for chemical-looping steam methane reforming. *International Journal of Hydrogen Energy*, *38*(11), 4492–4501. https://doi.org/10.1016/j.ijhydene.2013.01.115

[30] Zheng, Y., Li, K., Wang, H., Tian, D., Wang, Y., Zhu, X., Wei, Y., Zheng, M., & Luo, Y. (2016). Designed oxygen carriers from macroporous $LaFeO_3$ supported CeO_2 for chemical-looping reforming of methane. *Applied Catalysis B Environment and Energy*, *202*, 51–63. https://doi.org/10.1016/j.apcatb.2016.08.024

[31] Zheng, Y., Wei, Y., Li, K., Zhu, X., Wang, H., & Wang, Y. (2014). Chemical-looping steam methane reforming over macroporous CeO_2–ZrO_2 solid solution: Effect of calcination temperature. *International Journal of Hydrogen Energy*, *39*(25), 13361–13368. https://doi.org/10.1016/j.ijhydene.2014.04.116

6. Preliminary investigation on exsolution-promoted $Sr_2FeMo_{0.6}Ni_{0.4}O_6$ double perovskite as oxygen carrier for chemical looping steam methane reforming

Abstract

This study investigates the performances of the double perovskite $Sr_2FeMo_{0.6}Ni_{0.4}O_{6-\delta}$ in Chemical Looping Steam Methane Reforming (CL-SMR) cycles, focusing on the effect of redox exsolution of Ni-rich nanoparticles on the CH_4 activation ability and the stability of the Oxygen Carrier (OC). The observed structural changes taking place upon high-temperature reduction in a CH_4-containing atmosphere has proven to improve the catalytic properties of the OC material, leading to an improved oxygen exchange in respect of the pristine material and a stable performance in 50 CL-SMR cycles. XRD, HAADF-STEM and EDS analyses enlightened the reversible migration of Fe from the perovskite backbone to the metallic particles upon exposure to reducing and oxidizing conditions. Further investigations are foreseen to clarify the role of this process on the OC redox properties.

6.1. Introduction

Previous chapters elucidated how the Ni-based catalyst's stability is crucial to provide a stable cyclical performance in CL-SMR cycles for composite Fe-based OCs. To overcome the unavoidable tendency of nanometric-sized supported Ni particles to grow by mechanisms such as coalescence and Ostwald ripening [1], an alternative design method was evaluated for the preparation of Ni-decorated oxygen carriers, namely redox exsolution. The latter is an approach to material design in which the guest elements, that are intended to form catalytically active metal particles exposed to the gaseous environment, are substituted into the lattice of a host oxide [2]. To provide the adequate thermodynamic drive for the exsolution process while retaining the stability of the host oxide lattice, the guest material should have a lower change in the Gibbs free energy of reduction from the oxidized to the metallic state in respect of the host elements. In this way, upon exposure to reducing conditions, a partial or total reduction of the guest element is obtained. Once reduced, the guest atoms migrate across the host lattice and coalesce, inducing the growth of nanometric-sized particles directly from the host lattice. The partially oxide-socketed nature of the so-produced particles, and the strong metal-oxide interaction that arises from the crystallographic alignment between the exsolved and the host phase provide some unique features to the particles, such as superior resistance against sintering, poisoning and carbon deposition, and higher catalytic activity induced by the strain applied on the metallic lattice [3]. The vast majority of the recent studies concerning exsolving materials for catalytic applications employs perovskites as the host structure [4]. This class of materials appears as the ideal candidate thanks to its generally high redox stability, provided by the ability to accommodate oxygen vacancies without affecting the lattice integrity, and his compositional flexibility [5]. Perovskites are oxides with the general chemical formula ABO_3, in which A is commonly an alkali earth or rare earth metal and B is a transition metal [6]. The

compositional flexibility is dependent on the ionic radii of the A and B-sites. Moreover, the structure can tolerate the substitution of A and B cations with other elements in large amounts, eventually leading to the formation of self-assembled layered structures [7]. An example of this are double perovskites, with general chemical formula $A_2BB'O_6$. The additional tunability provided by the double perovskite structure further expands the design space of this class of materials, in turn expanding the possibilities of exsolving materials. Few studies investigated the effect of redox exsolution on CH_4-fuelled CL processes. Exsolution of Ni particles from $La_{0.5}Ca_{0.4}Ni_{0.2}Ti_{0.8}O_{3-\delta}$ was reported to significantly improve the CH_4 conversion, being able to activate CH_4 at temperatures as low as 420 °C. The exsolved material displayed a superior stability against analogous materials prepared by impregnation [8]. The formation of metallic nanoclusters within the lattice of $La_{0.8}Ce_{0.1}Ni_{0.4}Ti_{0.6}O_3$ upon high-temperature reductive treatment notably improved the oxygen transport by inducing strain on the oxide backbone and on the particles themselves [9]. A similar composition, in which part of the Ni is substituted by Co ($La_{0.8}Ce_{0.1}Co_{0.3}Ni_{0.1}Ti_{0.6}O_3$) has been observed to be able to activate CH_4 at lower temperatures in respect of the Ni-only counterpart. The Co substitution resulted in the exsolution of Co-Ni alloy nanoparticles, evidencing the potential for the fine-tuning of the catalytic properties of the solid by controlling the particles composition [10]. Exsolution of Co nanoparticles from $La_{0.6}Sr_{0.4}Cr_{0.8}Co_{0.2}O_3$ has been found to increase not only the rate of OC reduction in CH_4 but also of oxidation with CO_2 [11]. This is particularly relevant considering that the thermodynamics and kinetics of oxidation can significantly limit the OTC of perovskite OC systems [12]. Furthermore, $Ca_2Fe_2O_5$ (C2F) was also considered as host material for exsolving transition metals more reducible than Fe, such as Cu and Ni. The Cu and Ni-doped C2F has been tested for CL-SMR cycles at 850 °C, strongly promoting in both case the reduction kinetics. Nevertheless, concerns on the stability of the produced OCs, linked to the kinetically limited reincorporation of the dopants inside the host lattice and on the segregation of dopant-containing phases such as alloys and spinel-type oxides has been raised, as also observed in chapter 4. While these works open up the potential of exsolving materials in a wide array of CL applications, the topic has not been extensively studied yet. In a recent investigation by our group, $Sr_2FeMo_{0.6}Ni_{0.4}O_{6-\delta}$ double perovskite was investigated as OC in the CL reverse water gas shift reaction (CL-RWGS). Exsolution of Ni-Fe alloy nanoparticles determined an increase in the oxygen exchange during both the reduction and the oxidation step. The exsolved OC also exhibited a remarkable cyclic stability, being able to retain good performances in more than 300 CL-RWGS cycles [12]. In the present work, we investigate the role of the Ni_3Fe exsolution on CL-SMR cycles, providing insights on the dynamics and role of the structural evolution of the carrier at reaction conditions.

6.2. Experimental

The details on samples preparation and characterization methods are reported in chapter 2.

Multicycle water splitting experiments were carried out at 550 °C and 850 °C with an Autochem II 2920 Micromeritics Analyzer equipped with a thermal conductivity detector. One cycle consisted of a reduction step with a temperature programmed heating ramp of 10 °C min^{-1} from room temperature up to the target temperature, using 5% of H_2 in N_2 flow (35 mL min^{-1}) as reductant. The sample was idled 30' (1 h in the experiment at 850 °C) in the same conditions, then purged with N_2 before of the oxidation step. This later was performed by subsequent

pulses of water vapor (0.15 μL) up to achieve a steady state for H_2 production. The sample was then cooled down to RT, to repeat the cycle. 10 cycles were executed, using different specimens for each selected temperature.
High-angle annular dark field scanning transmission electron microscopy (HAADF-STEM), high-resolution transmission electron microscopy (HRTEM) and energy-dispersive X-ray analysis (EDS) images were acquired on a FEI Tecnai G2 F20 instrument equipped with a field emission gun operating at an accelerating voltage of 200 kV. HAADF-STEM and EDS analysis on SFMN tested for CL-RWGS cycles were acquired at the National Institute of Materials Physics, Marguele (RO), with a JEM ARM200F probe-corrected analytical TEM/STEM operated at 200 kV.
Temperature-Programmed Reduction (TPR) in CH_4 atmosphere was conducted in a thermogravimetric analyser (TGA) (STA 2500 Regulus, Netzsch, Germany) at Politecnico di Torino, Torino (IT), both on a pristine SFMN sample and on a previously exsolved sample. The exsolution was induced exposing SFMN to 10% H_2/N_2 at 850 °C for 2 h in a microreactor, with a gas flow rate of 200 Nml/min. Once loaded into the TGA, the samples were heated to 850 °C (20 °C/min) in 100% Ar, kept for 30 min at 850 °C in 50% air/Ar and cooled down back to 250 °C (20 °C/min) in 100% Ar. The TPR was performed from 250 °C up to 850 °C (10 °C/min), under a 2.5% CH_4/Ar mixture. Isothermal reduction at 850 °C was avoided to limit CH_4 cracking and carbon deposition.
CL-SMR were run isothermally at 850 °C. Each step consisted in a reduction step, in which 5% CH_4 was fed to the reactor for 10 minutes and a steam oxidation step, in which approximately 10% H_2O was fed to the reactor for 10 minutes. 100 mg of sample was loaded onto a microreactor connected to a calibrated mass spectrometer (Hiden Analytical HPR20). CH_4, H_2, CO, CO_2 and O_2 calibration factors were periodically corrected using standard mixtures. H_2O calibration factor was inferred from the H_2 consumption of the reduction of a known amount of CuO. The accuracy was monitored performing carbon balances, closed to within 10%. Sample temperature was monitored through a K-type thermocouple placed close to the reactive bed. Gaseous reactants were fed to the reactor by mass flow controllers, while steam was fed by flowing He in a saturator operating at a constant temperature of 50 °C. All the inlet and outlet lines were heated to avoid condensation. The inlet flow rate was kept constant at 50 Nml/min, obtaining a GHSV ≈ 20.000 h^{-1}.

6.3. Results and discussion

6.3.1. Stability with steam

Literature regarding Ni doped $Sr_2Fe_{2-x}Mo_xO_6$ double perovskites report that reducing environments and relatively high temperatures (820-900 °C) are required to drive the B-site cations reduction and the nucleation of the metallic nanoparticles along with the phase transformation of the host perovskite matrix [12, 13, 14, 15]. A preliminary assessment of SFMN stability when repeatedly exposed to steam at high temperature was carried out before testing the material for CL-SMR. The assessment has been performed at two target temperatures, 550 °C and 850 °C, to draw a comparison between non-exsolving and exsolving conditions respectively. The lower temperature was selected to allow for the reduction of Ni^{2+} to Ni^0, Fe^{3+} to Fe^{2+} and Mo^{6+} to Mo^{5+} and Mo^{4+} without allowing significative cations migration and phase segregations [16]. TPRs up to the target temperature were performed, followed by isothermal H_2O pulses at the same temperature. Results for selected cycles are shown in figure 6.1. At 550 °C, the first TPR show two adjacent reduction peaks (at 350 and 420 °C), that could be attributed to the

reduction of surface oxygen species and high valence cations (Ni^{2+}, Fe^{3+} and Mo^{6+}) [15]. The first cycle shows a higher H_2 consumption in respect of the following ones, for which both the hydrogen consumption and the TPR profile remain stable. From the second cycle, the higher temperature reduction peak appears anticipated to 400 °C, and the appearance of a shoulder at 280 °C is observed. The overall H_2 production during water splitting pulse step is lower in the first cycle, while it remains stable from the second cycle onward, with H_2 yield quickly decreasing from the third H_2O pulse. At 850 °C, the first TPR shows a high temperature contribution starting from 700 °C, that can be ascribed to the reduction of bulk lattice oxygen [17]. From the second TPR onward, only a single reduction peak at 450 °C could be seen. At this temperature, the H_2 consumption grows from the first to the second cycle and stabilizes later on. Also in this case, H_2 production is lower in the first cycle, and stabilizes after the second. Overall, SFMN appears to be stable in H_2-H_2O cycles, with cycle temperature affecting both H_2 consumption upon reduction and H_2 yield during water splitting.

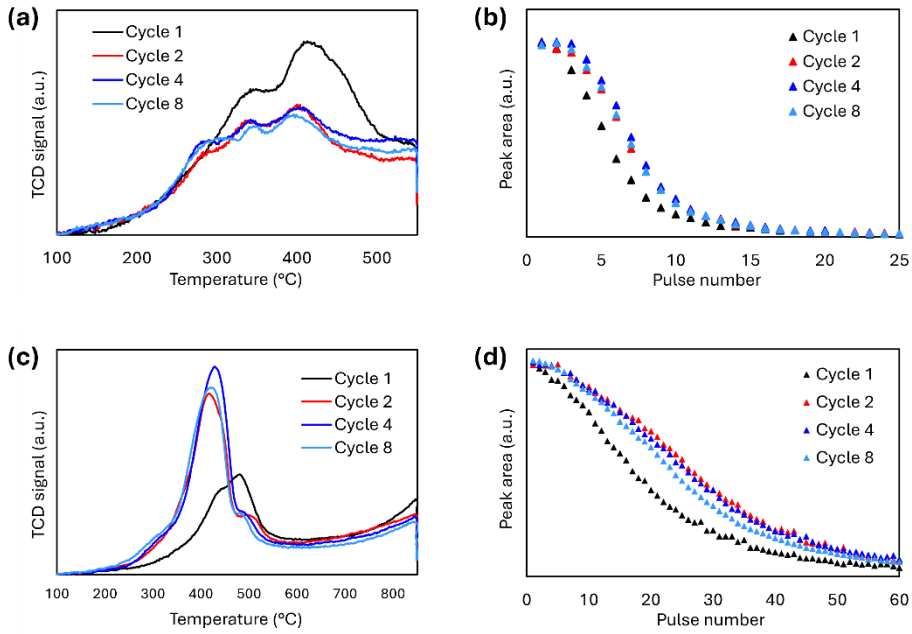

Fig. 6.1. Alternated H_2-TPRs and isothermal H_2O-pulses oxidations on SFMN samples up to (a-b) 550°C, (c-d) 850°C.

Figure 6.2 shows HAADF-STEM images and EDS analysis of the two samples after 10 TPR-H_2O pulses cycles. The sample tested at 550°C (figure 6.2a) appears constituted of large particles of about 100-250 nm, partially sintered. The area enclosed. It is possible to distinguish small, bright embedded particles of about 5-15 nm on the surface of the sample. EDS analysis of one of these spots shows the presence of a high concentration of Ni and Fe (spectrum in yellow), while the Sr and Mo signals are weak and probably originate from the matrix. In contrast, the EDS spectrum of the area marked by the orange rectangle shows nearly no Ni, but intense signals of Sr, Mo and Fe. Round-shaped particles embedded in a matrix, which measure around 30-80 nm can be clearly recognized in the sample tested at 850 °C (figure 6.2b). Interestingly, a magnification of these particles (Figure 6.2b) reveals that they are decorated with patches showing low contrast. The EDS analysis (green square) of these particles show that they are made by Ni and Fe, being Ni much more abundant. In contrast, the EDS spectra of the patches on top of the particles are constituted by solely Sr and Mo and minor Fe. It is possible to conclude that at low

temperature the exsolution remains incipient and that the growth of exsolved particles depends on the operating temperature. X-rays diffractograms of the cycled samples (figure 6.3) confirms that the sample tested at 850 °C underwent a structural transformation, with the appearance of the (100) peak of the cubic Ni-rich metallic phase at 44.5° 2θ and of a layered RP phase of composition $Sr_3FeMoO_{7-\delta}$ (shoulder at 31.5° 2θ) and a perovskite-like phase of composition $Sr_2Fe_{2-x}Mo_xO_{6-\delta}$, evidenced by the slight shift of the main SFMN peak at lower angles [13]. As observed from the TPRs (figure 6.1c, d), the development of this complex structure promoted the redox activity of the solid.

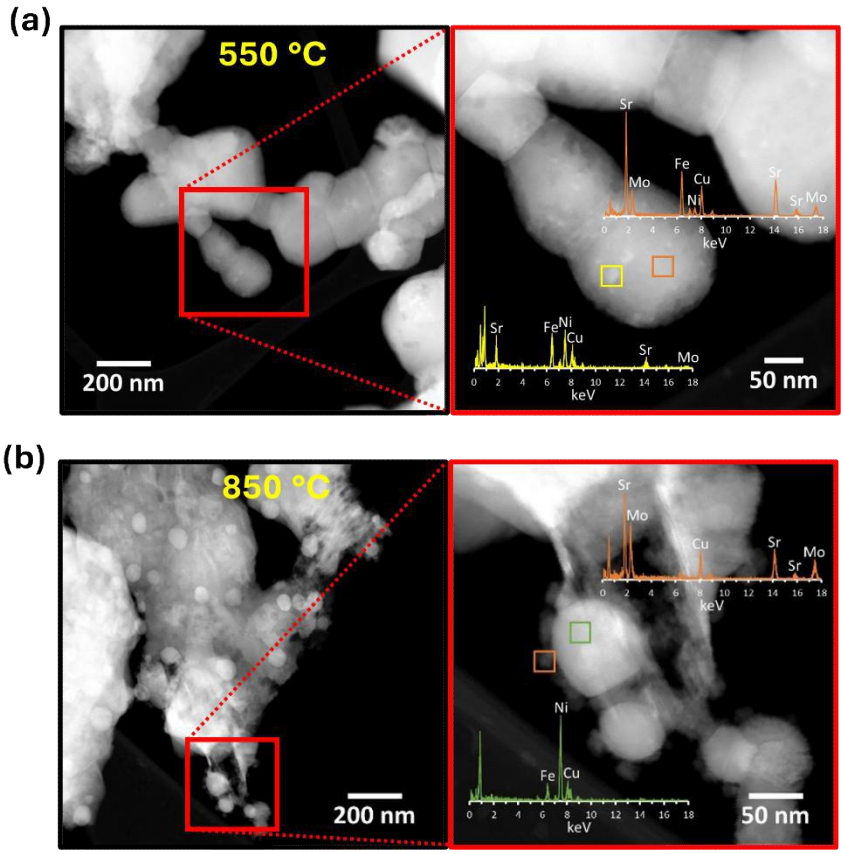

Fig. 6.2. HAADF-STEM images and EDS of samples subjected to 10 H_2-TPR – H_2O pulse oxidation cycles up to (a) 550 °C and (b) 850 °C.

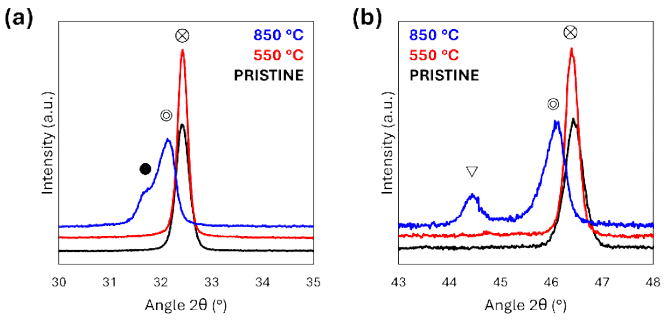

Fig. 6.3. Details of the diffraction patterns of the pristine and cycled samples in the (a) 30-35 and (b) 43-48 ° 2θ range. (⊗) SFMN [15]. (◎) Sr_2FeMoO_6 (PDF card 00-070-4093). (●) Sr_3FeMoO_7 (PDF card 00-052-1715). (▽) Ni (PDF card 00-004-0850).

6.3.2. Reactivity with CH_4

The effect of the exsolution on the catalytic properties was studied by performing CH_4-TPR in a thermobalance. Figure 6.4 shows the weight variation of pristine SFMN and of SFNM precedingly exposed to 10% H_2 at 850 °C for 2 h to induce the exsolution [12]. While the weight signal is similar for the two samples below 730 °C, above that temperature the exsolved sample shows an improved reactivity towards CH_4, indicating the beneficial effect of the structural transformations taking place on high-temperature reduction. SFMN reactivity was further studied by isothermal reduction at 850 °C in a microreactor. Figure 6.5a reports the gas composition at the outlet of the reactor. At the beginning of the reaction, only total combustion products are evolved, as commonly observed for OCs such as $Ca_2Fe_2O_5$, discussed in the previous chapters. After 3 minutes, the production of H_2O and CO_2 drops to almost zero, while H_2 and CO begins to be observed. The H_2 and CO productivity then increases almost linearly to 15 minutes, when the production of CO stabilizes and the formation of some solid carbon from pyrolysis is expected, as evidenced by the increasing H_2 to CO ratio. The reduction was stopped after 17 minutes to prevent the formation of large amounts of solid carbon on the sample, which may complicate further analyses. The X-ray diffractogram of the tested sample (figure 6.5b) shows that the exposure to a CH_4-containing atmosphere at high temperature induces the reconstruction of the crystalline structure in a similar fashion as already observed with H_2. Alongside the $Sr_2Fe_{2-x}Mo_xO_{6-\delta}$ perovskite-like phase and the $Sr_3FeMoO_{7-\delta}$ RP phase, the formation of a cubic phase, attributed to a Ni-rich Ni-Fe alloy (possibly corresponding to Ni_3Fe [12]) and of segregated Sr_3MoO_6 is observed. The cyclical exposure to CH_4 and H_2O-containing atmospheres is thus expected to induce similar modification of the crystalline structure as already observed with H_2-H_2O cycles.

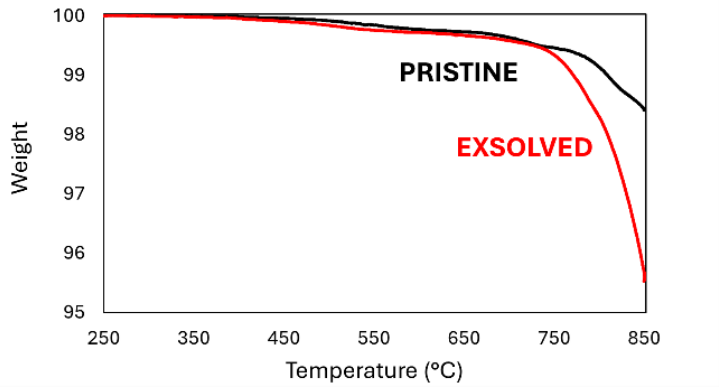

Fig. 6.4. CH_4 temperature-programmed reduction with 2.5% CH_4 in a TGA.

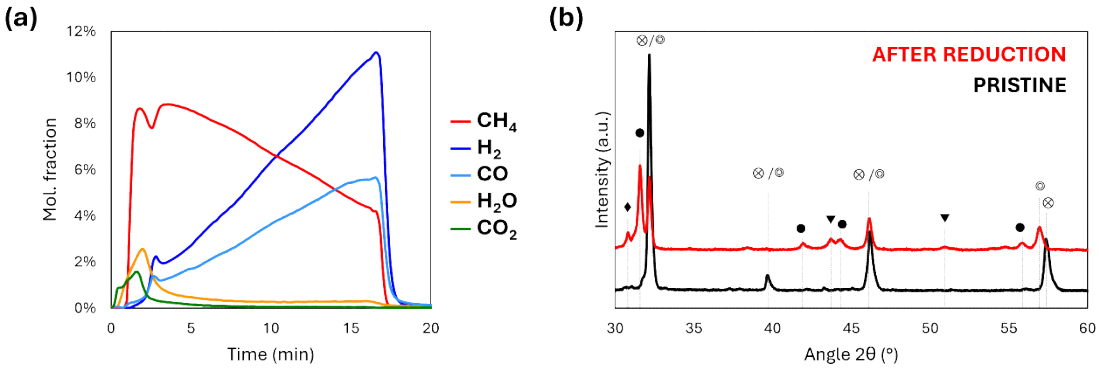

Fig. 6.5. (a) Isothermal reduction with 5% CH_4 at 850 °C. (b) Diffraction pattern of the sample before and after the reduction. (⊗) SFMN [15], (◎) Sr_2FeMoO_6 (PDF card 00-070-4093), (●) Sr_3FeMoO_7 (PDF card 00-052-1715), (▼) Ni_3Fe (PDF card 00-047-1417). (♦) Sr_3MoO_6 (PDF: 00-024-1215).

6.3.3. CL-SMR performance

Pristine SFMN was then tested for 50 CL-SMR cycles at 850 °C, to evaluate the evolution of its performances upon cycling and assess its stability at the reaction conditions. The results are quantified in terms of CH_4 conversion and CO selectivity for the reduction step, and H_2 yield and purity for the oxidation step. As shown in figure 6.6a, the fuel conversion exhibits a fast increase in the first 8 cycles, while stabilizing afterward to 35%. The increase in the CH_4 conversion corresponds to an increase in the CO production, while the amount of evolved CO_2 decreases in the first 3 cycles and stabilizes afterwards at 0.2 mmol/g (figure 6.6b). Thus, the structural evolution taking place upon redox cycling appear to be beneficial for the catalytic activity of the OC material towards CH_4 conversion and to promote the fuel partial oxidation against combustion, leading to a CO selectivity as high as 95%. This latter observation is believed to be related to the microstructural changes that take place upon cycling to the coordination environment of the reducible cations and to the stabilization of lattice oxygen vacancies, as previously observed on other perovskite-based OC materials [18]. The increased reactivity of the OC give rise to an increased amount of oxygen exchanged during the reduction, promoting the generation of H_2 by water splitting (figure 6.7). Nevertheless, at the conditions adopted for the cycles some solid carbon formation was observed, which resulted in a reduced H_2 purity due to CO and CO_2 evolution from the gasification of the deposited carbon. The amount of carbon formed increased during the first 8 cycles following the increase in the fuel conversion, likely because of a higher depletion of lattice oxygen related to the higher activity. A second increase was observed from the 20th cycle onward, which is hypothesized to be caused by sintering phenomena of the metallic and oxide particles, which can affect the catalytic activity and the oxygen mobility of the OC material [19, 20, 21]. At the 50th cycle, the H_2 yield was equal to 2.8 mmol/g.

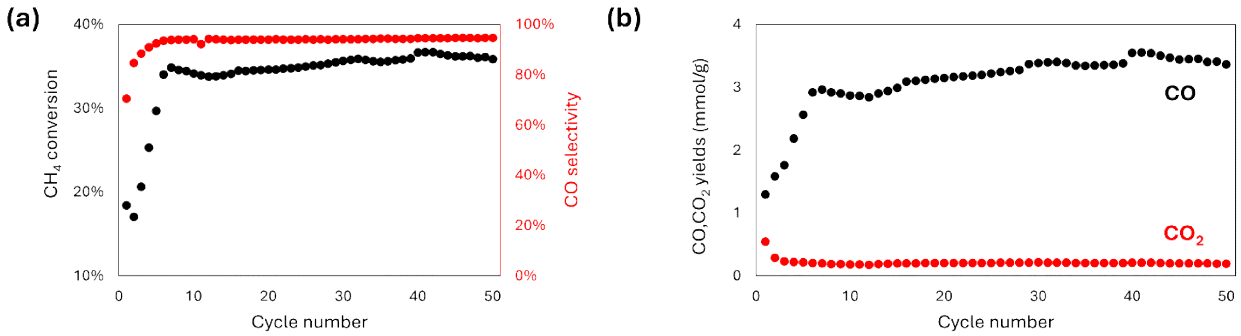

Fig. 6.6. (a) CH_4 conversion and CO selectivity of SFMN in 50 CL-SMR cycles. (b) CO, CO_2 yields in the reduction step.

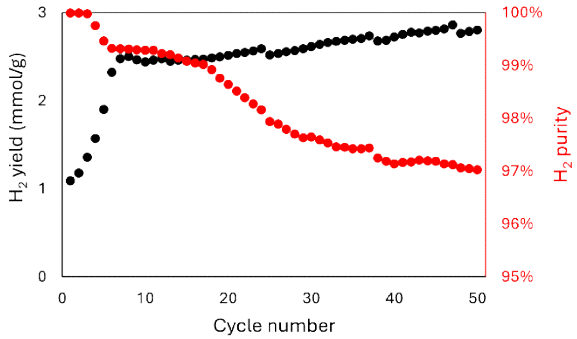

Fig. 6.7. H_2 yield and purity of SFMN in 50 CL-SMR cycles.

XRD patterns acquired on the sample after the 51st reduction and the 51st oxidation (figure 6.8) reveal that in reduced conditions part of the iron from the perovskite backbone migrates into the exsolved nanoparticles to form a Ni-rich alloy and an additional amount of RP phase. The phenomenon appears to be reversible upon exposure of the sample to steam.

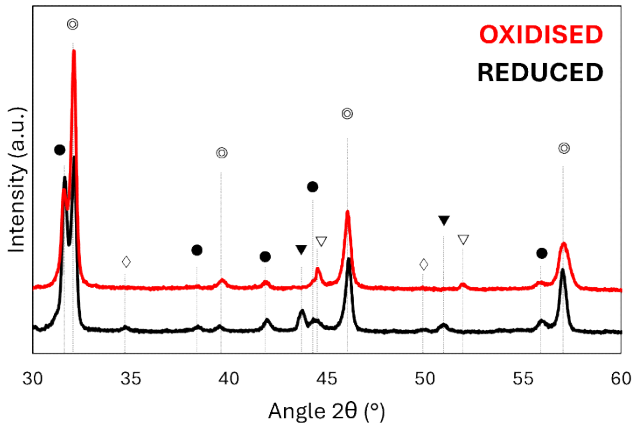

Fig. 6.8. X-ray diffractograms of SFMN after 50 CL-SMR cycles and brought to ambient temperature in reduced (black curve) and oxidised (red curve) conditions. (⊗) SFMN [15]. (◎) Sr_2FeMoO_6 (PDF card 00-070-4093). (●) Sr_3FeMoO_7 (PDF card 00-052-1715). (▽) Ni (PDF card 00-004-0850). (▼) Ni_3Fe (PDF card 00-047-1417). (◊) SrO (PDF card 01-075-0263).

The cyclic migration of Fe inside and outside the Ni-rich metallic exsolved nanoparticles respectively in reducing and oxidising conditions has been observed on the same material when tested for a different CL application, namely chemical looping reverse water-gas shift (CL-RWGS). HAADF-STEM and EDS investigation was performed on two SFMN samples subjected to 20 isothermal CL-RWGS cycles at 850 °C and brought back to ambient temperature in reduced and oxidized conditions. Cycles has been carried out in the same experimental setup as CL-SMR tests, reducing the sample in 5% H_2 for 30 min and oxidizing it in 20% CO_2 for 30 min, maintaining a constant flowrate of 35 ml/min. Figure 6.9 shows the HAADF-STEM image and the corresponding elemental mapping of the cycled sample in reduced conditions. The presence of round bright particles is clearly observed on the surface of the grain. The elemental analysis indicate that all the Ni is located in the particles, along with some Fe (site 3 in the figure). The grain matrix is instead composed by Sr along with Fe and O (site 2). A large hemispherical particle can be observed, which do not contain any Fe, but only Sr and O (site 1). EDS mapping of the same site (figure 6.10) confirms that Mo is present both in the grain matrix and in the Sr containing particle, indicating that the latter is composed by segregated Sr and Mo oxide, such as Sr_3MoO_6 observed on SFMN reduced by CH_4 (figure 6.5). The oxidised sample (figure 6.11) shows instead an exsolved nanoparticle exclusively composed by Ni, while Fe is present alongside O in the grain matrix, suggesting that it exist in an oxide structure. The Ni-Fe alloying process taking place during the reduction step could play a role in limiting the solid carbon formation on the active sites [22].

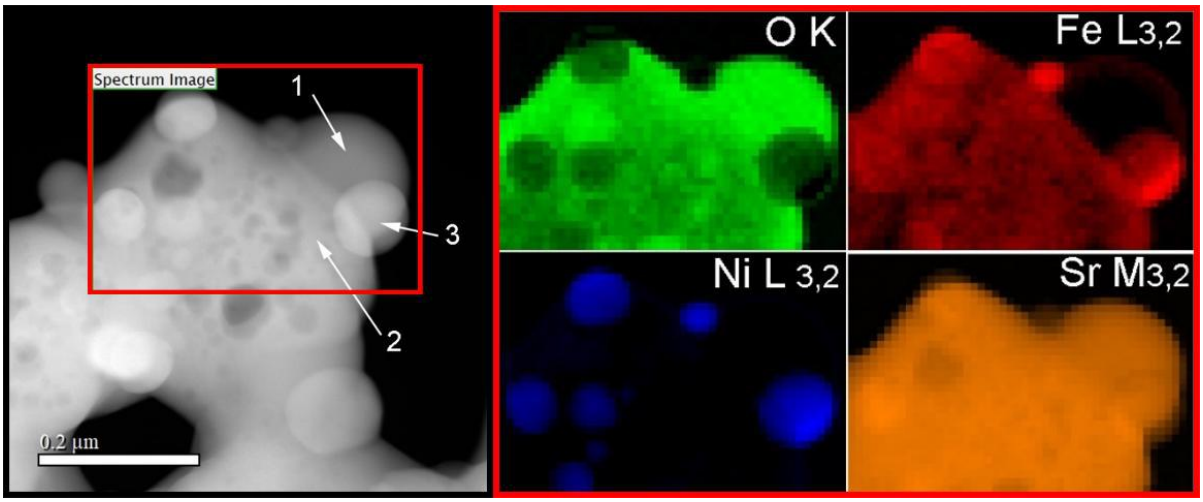

Fig. 6.9. HAADF-STEM image and elemental maps of a SFMN sample tested for 20 CL-RWGS cycles at 850 °C and brought to ambient temperature in reduced conditions.

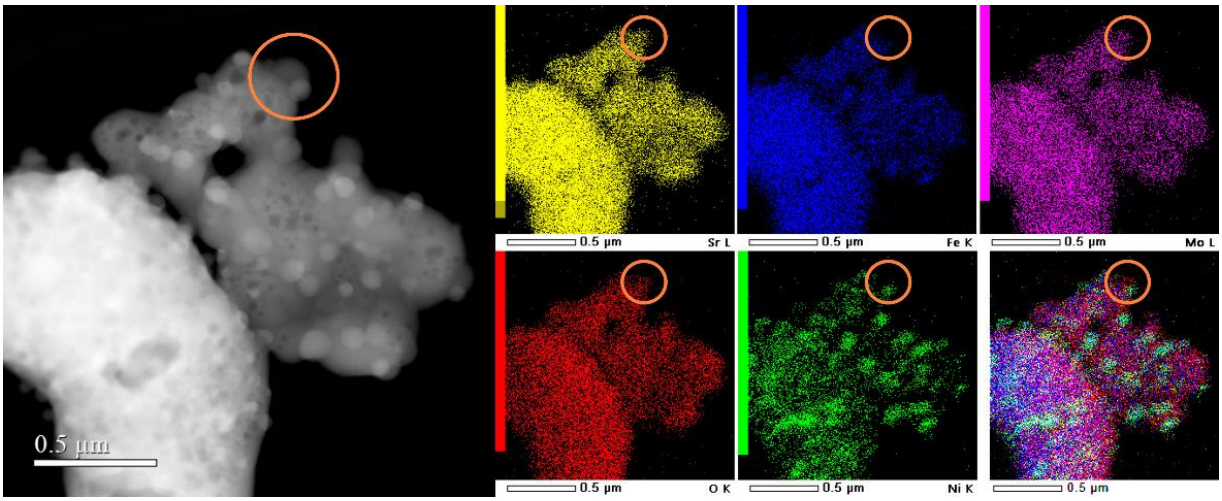

Fig. 6.10. HAADF-STEM image and EDS elemental maps of Sr, Fe, Mo, O and Ni of a SFNM sample tested for 20 CL-RWGS cycles at 850 °C and brought to ambient temperature in reduced conditions. The orange circle indicates the hemispherical particle labelled as site 1 in figure 6.9.

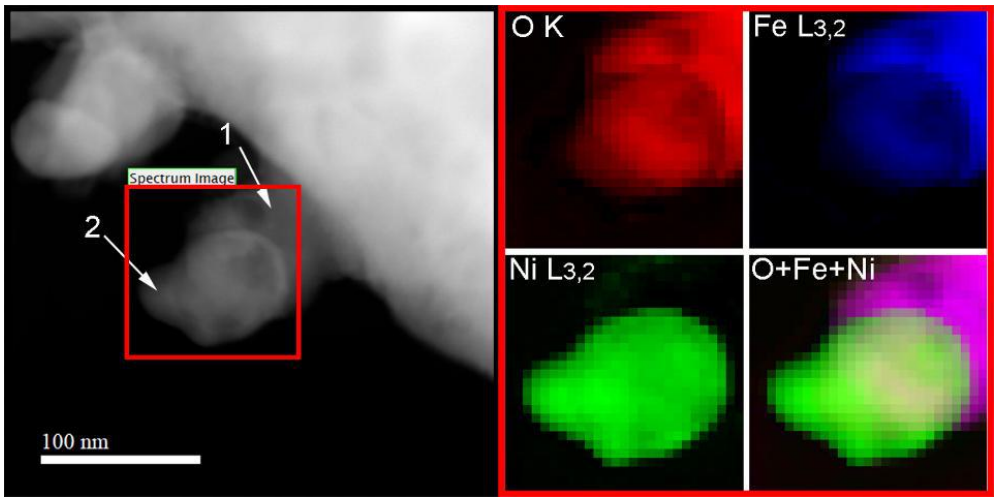

Figure 6.11. HAADF-STEM image and elemental maps of a SFMN sample tested for 20 CL-RWGS cycles at 850 °C and brought to ambient temperature in oxidised conditions.

The role of the structural transformations taking place upon exsolution on CL-SMR performances has been further investigated by comparing SFMN with a Ni-free reference sample of stoichiometry $Sr_2Fe_{1.5}Mo_{0.5}O_6$ (SFM), known for its stability in reducing and oxidizing conditions at high temperatures [23]. As shown in figure 6.12, the SFM sample subjected to 10 CL-SMR cycles at 850 °C do not show major variations in its crystalline structure. Only the appearance of small shoulders of at lower angles could be detected on the diffraction peaks at 32.3 and 57.6 ° 2θ, possibly related to the formation of small amounts of segregated $SrMoO_3$ [24]. In CL-SMR cycles, SFM shows stable performances in terms of fuel conversion and CO selectivity, in contrast with SFMN. Results clearly show that the phase evolution underwent by SFMN during the first 8 redox cycles lead to an improvement of catalytic activity.

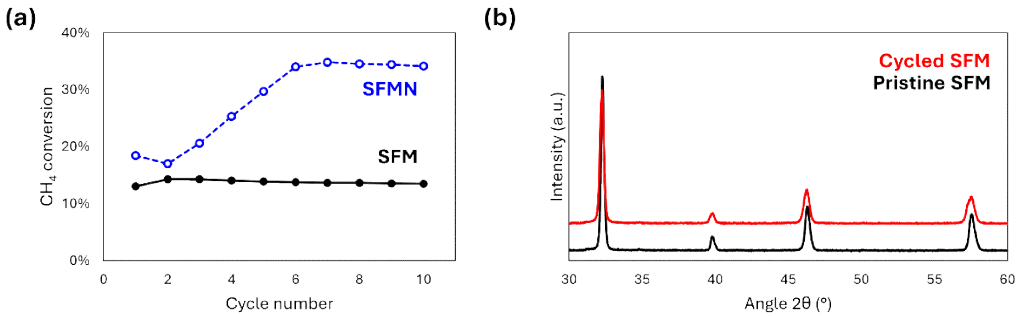

Fig. 6.12. (a) Fuel conversion of SFM in 10 CL-SMR cycles, compared with SFMN. (b) X-ray diffraction patterns of SFM before (black curve) and after (red curve) the test.

6.4. Conclusions

The activity and stability of the double perovskite $Sr_2FeMo_{0.6}Ni_{0.4}O_6$ (SFMN) as the OC in isothermal CL-SMR cycles at 850 °C has been investigated, together with the evolution of its redox, structural, and morphological properties upon exposure to steam at intermediate (550 °C) and high (850 °C) temperatures and upon cyclical reductions and oxidation. H_2-TPRs showed that increased redox properties could be obtained when SFMN is exposed to reducing conditions at high-temperature, in agreement with previous reports [12], while H_2O-pulse oxidation experiments reported a reproducible H_2 production following the structural evolution of the material. XRD provided insights on the decomposition of the original SFMN phase, that led to the formation of a Ruddesleden-Popper (RP) phase and of metallic Ni-rich nanoparticles along with the perovskite. Exsolved particles morphology and composition was further investigated by HAADF-STEM and EDS, revealing the formation of quasi-spherical particles of 50-100 nm in size onto the oxide backbone. The exsolution process was confirmed beneficial for the reactivity with CH_4, leading to methane activation at lower temperature (730 instead of 780 °C) and to a faster oxygen exchange between the solid and the gas. The exsolution process has been found to be enabled by direct reduction with CH_4, and a continuous improvement in the fuel conversion and in the oxygen transfer capacity (OTC) of the solid has been observed during the first 8 CL-SMR cycles performed on pristine SFMN. Once activated, the OC showed an excellent stability, which was related to the reversible formation of the $Sr_3FeMoO_{7-\delta}$ RP phase and the migration of Fe into the exsolved particles. The iron migration to form an alloy with Ni is observed also when testing the same material for CL-RWGS cycles, as seen from HAADF-STEM and EDS characterization. In respect of a non-exsolving Ni-free $Sr_2Fe_{1.5}Mo_{0.5}O_6$ (SFM), the exsolved material shows a clear improvement of the CL-SMR performance. The investigation, although preliminary in its nature, enlighten the potentialities of exsolving materials as highly stable and active OCs for CH_4-fuelled CL applications.

6.5. References

[1] Visser, N. L., Turner, S. J., Stewart, J. A., Vandegehuchte, B. D., Van Der Hoeven, J. E. S., & De Jongh, P. E. (2023). Direct Observation of Ni Nanoparticle Growth in Carbon-Supported Nickel under Carbon Dioxide Hydrogenation Atmosphere. ACS Nano, 17(15), 14963–14973. https://doi.org/10.1021/acsnano.3c03721

[2] Neagu, D., Tsekouras, G., Miller, D. N., Ménard, H., & Irvine, J. T. S. (2013). In situ growth of nanoparticles through control of non-stoichiometry. *Nature Chemistry*, *5*(11), 916–923. https://doi.org/10.1038/nchem.1773

[3] Kousi, K., Tang, C., Metcalfe, I. S., & Neagu, D. (2021). Emergence and future of exsolved materials. *Small*, *17*(21). https://doi.org/10.1002/smll.202006479

[4] Carrillo, A. J., López-García, A., Delgado-Galicia, B., & Serra, J. M. (2024). New trends in nanoparticle exsolution. *Chemical Communications*, *60*(62), 7987–8007. https://doi.org/10.1039/d4cc01983k

[5] Peña, M. A., & Fierro, J. L. G. (2001). Chemical structures and performance of perovskite oxides. *Chemical Reviews*, *101*(7), 1981–2018. https://doi.org/10.1021/cr980129f

[6] Bhalla, A., Guo, R., & Roy, R. (2000). The perovskite structure—a review of its role in ceramic science and technology. *Materials Research Innovations*, *4*(1), 3–26. https://doi.org/10.1007/s100190000062

[7] Xu, X., Zhong, Y., & Shao, Z. (2019). Double Perovskites in Catalysis, Electrocatalysis, and Photo(electro)catalysis. *Trends in Chemistry*, *1*(4), 410–424. https://doi.org/10.1016/j.trechm.2019.05.006

[8] Otto, S., Kousi, K., Neagu, D., Bekris, L., Janek, J., & Metcalfe, I. S. (2019). Exsolved nickel nanoparticles acting as oxygen storage reservoirs and active sites for redox CH_4 conversion. *ACS Applied Energy Materials*, *2*(10), 7288–7298. https://doi.org/10.1021/acsaem.9b01267

[9] Kousi, K., Neagu, D., Bekris, L., Papaioannou, E. I., & Metcalfe, I. S. (2019). Endogenous nanoparticles strain perovskite host lattice providing oxygen capacity and driving oxygen exchange and CH_4 conversion to syngas. *Angewandte Chemie International Edition*, *59*(6), 2510–2519. https://doi.org/10.1002/anie.201915140

[10] Kousi, K., Neagu, D., Bekris, L., Calì, E., Kerherve, G., Papaioannou, E. I., Payne, D. J., & Metcalfe, I. S. (2020). Low temperature methane conversion with perovskite-supported exo/endo-particles. *Journal of Materials Chemistry A*, *8*(25), 12406–12417. https://doi.org/10.1039/d0ta05122e

[11] Carrillo, A. J., Kim, K. J., Hood, Z. D., Bork, A. H., & Rupp, J. L. M. (2020). $La_{0.6}Sr_{0.4}Cr_{0.8}Co_{0.2}O_3$ Perovskite Decorated with Exsolved Co Nanoparticles for Stable CO_2 Splitting and Syngas Production. *ACS Applied Energy Materials*, *3*(5), 4569–4579. https://doi.org/10.1021/acsaem.0c00249

[12] Orsini, F., Ferrero, D., Cannone, S. F., Santarelli, M., Felli, A., Boaro, M., De Leitenburg, C., Trovarelli, A., Llorca, J., Dimitrakopoulos, G., & Ghoniem, A. F. (2023). Exsolution-enhanced reverse water-gas shift chemical looping activity of $Sr_2FeMo_{0.6}Ni_{0.4}O_{6-\delta}$ double perovskite. *Chemical Engineering Journal*, *475*, 146083. https://doi.org/10.1016/j.cej.2023.146083

[13] Du, Z., Zhao, H., Yi, S., Xia, Q., Gong, Y., Zhang, Y., Cheng, X., Li, Y., Gu, L., & Świerczek, K. (2016). High-Performance Anode Material $Sr_2FeMo_{0.65}Ni_{0.35}O_{6-\delta}$ with In Situ Exsolved Nanoparticle Catalyst. *ACS Nano*, *10*(9), 8660–8669. https://doi.org/10.1021/acsnano.6b03979

[14] Feng, J., Yang, G., Dai, N., Wang, Z., Sun, W., Rooney, D., Qiao, J., & Sun, K. (2014). Investigation into the effect of Fe-site substitution on the performance of $Sr_2Fe_{1.5}Mo_{0.5}O_{6-\delta}$ anodes for SOFCs. *Journal of Materials Chemistry A*, *2*(41), 17628–17634. https://doi.org/10.1039/c4ta03216k

[15] Felli, A., Duranti, L., Marelli, M., Dosa, M., Di Bartolomeo, E., Piumetti, M., & Boaro, M. (2023). $Sr_2FeNi_{0.4}Mo_{0.6}O_{6-\delta}$ Evolution for SOFC and SOEC Applications. *Journal of the Electrochemical Society*, *170*(11), 114511. https://doi.org/10.1149/1945-7111/ad06e7

[16] Lv, H., Lin, L., Zhang, X., Gao, D., Song, Y., Zhou, Y., Liu, Q., Wang, G., & Bao, X. (2019). In situ exsolved $FeNi_3$ nanoparticles on nickel doped $Sr_2Fe_{1.5}Mo_{0.5}O_{6-\delta}$ perovskite for efficient electrochemical

CO_2 reduction reaction. *Journal of Materials Chemistry A*, *7*(19), 11967–11975. https://doi.org/10.1039/c9ta03065d

[17] Lu, J., Yin, Y., Yin, J., Li, J., Zhao, J., & Ma, Z. (2015). Role of Cu and Sr in improving the electrochemical performance of Cobalt-Free $Pr_{1-x}Sr_xFe_{1-y}Cu_yO_{3-\Delta}$ Cathode for intermediate temperature solid oxide fuel cells. *Journal of the Electrochemical Society*, *163*(2), F44–F53. https://doi.org/10.1149/2.0181602jes

[18] Yang, J., Bjørgum, E., Chang, H., Zhu, K., Sui, Z., Zhou, X., Holmen, A., Zhu, Y., & Chen, D. (2021b). On the ensemble requirement of fully selective chemical looping methane partial oxidation over La-Fe-based perovskites. *Applied Catalysis B Environment and Energy*, *301*, 120788. https://doi.org/10.1016/j.apcatb.2021.120788

[19] Larring, Y., Pishahang, M., Tolchard, J., Lind, A. M., Sunding, M. F., Stensrød, R. E., Jacobs, M., Snijkers, F., Van Der Kolk, T., & Albertsen, K. (2019). Fabrication process parameters significantly affect the perovskite oxygen carrier materials (OCM) performance in chemical looping with oxygen uncoupling (CLOU). *Journal of Thermal Analysis and Calorimetry*, *140*(2), 577–589. https://doi.org/10.1007/s10973-019-08860-y

[20] Huang, X., Wang, X., Fan, M., Wang, Y., Adidharma, H., Gasem, K. A., & Radosz, M. (2017). A cost-effective approach to reducing carbon deposition and resulting deactivation of oxygen carriers for improvement of energy efficiency and CO_2 capture during methane chemical-looping combustion. *Applied Energy*, *193*, 381–392. https://doi.org/10.1016/j.apenergy.2017.02.059

[21] Han, Y., Tian, M., Wang, C., Kang, Y., Kang, L., Su, Y., Huang, C., Zong, T., Lin, J., Hou, B., Pan, X., & Wang, X. (2021d). Highly Active and Anticoke Ni/CeO_2 with Ultralow Ni Loading in Chemical Looping Dry Reforming via the Strong Metal–Support Interaction. *ACS Sustainable Chemistry & Engineering*, *9*(51), 17276–17288. https://doi.org/10.1021/acssuschemeng.1c06079

[22] Tomishige, K., Li, D., Tamura, M., & Nakagawa, Y. (2017). Nickel–iron alloy catalysts for reforming of hydrocarbons: preparation, structure, and catalytic properties. *Catalysis Science & Technology*, *7*(18), 3952–3979. https://doi.org/10.1039/c7cy01300k

[23] Liu, Q., Bugaris, D. E., Xiao, G., Chmara, M., Ma, S., Loye, H. Z., Amiridis, M. D., & Chen, F. (2011). $Sr_2Fe_{1.5}Mo_{0.5}O_{6-\delta}$ as a regenerative anode for solid oxide fuel cells. *Journal of Power Sources*, *196*(22), 9148–9153. https://doi.org/10.1016/j.jpowsour.2011.06.085

[24] Iranmanesh, M., Lingg, M., Stir, M., & Hulliger, J. (2016). Sol gel and ceramic synthesis of $Sr_2FeMo_{1-x}W_xO_6$ ($0 \leq x \leq 1$) double perovskites series. *RSC Advances*, *6*(48), 42069–42075. https://doi.org/10.1039/c6ra03923e

7. Concluding remarks and future perspectives

The research work hereby presented illustrated the development of catalyst-promoted Fe-based Oxygen Carriers (OC) for the Chemical Looping Steam Reforming (CL-SMR) process. Goal of the study was to explore novel methods for preparing oxygen carrier materials that combine the advantages of Fe-containing oxides, including environmental compatibility, relatively low cost, and the ability to be partially or fully reoxidized by steam, with the high CH_4 activation ability of Ni. The process enables the simultaneous production of pure hydrogen, along with the syngas derived from the partial oxidation of the hydrocarbons feed. The work provides guidance for the design of physically mixed OC-supported catalyst composite carrier systems, through the investigation of the CL-SMR performances, chemical compatibility, stability, and composition of such systems. Furthermore, a preliminary investigation into the use of an exsolving Ni-doped Fe-based perovskite highlights the potential of this class of materials in chemical looping processes—a potential that has remained largely unexplored until recently.

$Ca_2Fe_2O_5$ (C2F) was seen to be an ideal OC material, displaying an exceptional ability to withstand extensive reduction-oxidation cycling without performance deterioration, including at pressurized conditions. Moreover, it can be oxidized completely and relatively fast by steam, promoting hydrogen yield and productivity. The kinetic model developed in this work for the C2F reduction reaction with H_2 expands the knowledge on the effect of the total pressure on OC reactivity and may serve as a groundwork for the development of more complex investigations, such as direct reduction with CH_4 or reduction with complex gas mixtures.

As a strategy to improve the reduction kinetics of C2F with CH_4, the blending C2F with a Ni-loaded Ce-based material has been found remarkably effective, leading to the development of a stable composite OC able to compete with the best performing OC systems presented in literature. The optimized composition showed a high fuel conversion (66.6%) without significant carbon deposition, producing almost pure H_2 during the oxidation step. The high specific product yields, 13.4 and 6.6 mmol/g for syngas and H_2 respectively, reflect the good overall oxygen carrier capacity (OTC) of the composite.

The beneficial effect of introducing Ni in the system on a redox active support has been ascribed to a collaborative mechanism that takes place between the catalyst and the Fe-based carrier, mediated by the gas phase. The metallic Ni particles readily formed upon NiO reduction at the beginning of the reduction step can activate and partially oxidize methane, producing large amounts of H_2 and CO which drastically accelerates C2F reduction. As an additional benefit, Ni effectively catalyses the steam and dry reforming of CH_4, locally consuming full oxidation products and further enhancing fuel conversion. The physical barrier between Ni and C2F, provided by the Ce-based support, effectively inhibited Ni-Fe chemical interactions and the formation of mixed alloys and oxides, which are known to negatively impact CH_4 activation capability. Nevertheless, the redox stability of the reducible Ce-based support is critical for the long-term performance of the composite. The work highlighted the importance

of evaluating the chemical compatibility between components under actual reaction conditions, an essential step in the design process of such systems.

Further investigations are needed to clarify the role of the reducible support in promoting the catalytic activity of the Ni nanoparticles and the overall system, together with the characterization of the active sites for CH_4 and H_2O. An accurate mathematical description of the interplay between the catalyst and the OC phase could greatly benefit the design process of composite OC, fostering their optimization and scale up and facilitate the knowledge transfer to industrial partners.

A Ni-promoted Fe-based OC was also synthesized using an alternative approach that leverages the redox exsolution phenomenon. This investigation made use of $Sr_2FeMo_{0.6}Ni_{0.4}O_6$ (SFMN), a double perovskite previously studied for fuel cell applications. The perovskite underwent a structural evolution upon exposure to CH_4, leading to the development of a complex multiphase structure which included Ni- rich metallic nanoparticles and Ni-free perovskite-like and Ruddesleden-Popper phases. Although preliminary in its nature, the study showed that the transformation was able to promote both CH_4 activation and oxygen exchange and led to exceptionally stable CL-SMR performances.

The OC was observed to undergo reversible structural changes upon exposure to reducing and oxidizing conditions, characterized by the migration of iron inside the metallic nanoparticles upon reduction and back into the perovskite backbone upon oxidation with steam, further contributing to the oxygen transfer capacity (OTC) of the solid. The mechanism and the kinetics of this migration are not clear, and a detailed *in situ* microstructural analysis is advised to provide a complete description of the phenomenon. Moreover, the uncertainties regarding the metallic nanoparticle composition and surface features hinder the understanding of the role of Fe towards CH_4 and H_2O activation in the bimetallic particles which form upon reduction. Overall, a deeper knowledge of the dynamic processes taking place in exsolving materials upon redox cycling could enable a wider application of this class of materials in CL applications, unveiling their potential.

As the chemical looping (CL) approach gains increasing attention as an efficient and cost-effective alternative to traditional and emerging industrial processes, the significance of this study lies in its contribution to understanding the redox chemistry of the materials involved—key components in all CL processes.